

D^{*+} -meson production in
proton-proton and proton-lead
collisions in ALICE.

Annelies Marianne Veen

A catalogue record is available from the Utrecht University Library

ISBN 9789464192407 Copyright © 2021 by A.M.Veen

All right reserved. No part of this book may be reproduced, stored in a database or retrieval system, or published in any form of any way, electronically, mechanically, by print, photoprint, microfilm or any other means without prior written permission of the author. Typeset using \LaTeX Printed by Gildeprint.

D^{*+} -meson production in proton-proton and proton-lead collisions in ALICE

D^{*+} -mesonen productie in proton-proton en
proton-lood botsingen in ALICE

(met een samenvatting in het Nederlands)

Proefschrift

ter verkrijging van de graad van doctor aan de Universiteit Utrecht op
gezag van de rector magnificus, prof.dr. H.R.B.M. Kummeling,
ingevolge het besluit van het college voor promoties in het openbaar
te verdedigen op woensdag 7 juli 2021 des middags te 4.15 uur

door

Annelies Marianne Veen

geboren op 14 juli 1990 te Amsterdam

Promotor: Prof.dr. T.Peitzmann
Copromotoren: Dr. A. Mischke †
Dr. A. Grelli

Dit proefschrift werd (mede) mogelijk gemaakt met financiële steun van de Nederlandse Organisatie voor Wetenschappelijk Onderzoek (NWO).

Science is like life, you learn something new every day.

For my beautiful children, always stay curious.

Contents

	Page
1 Introduction	1
1.1 The Standard Model and Quantum Chromo-dynamics	2
1.2 The QCD phase diagram	5
1.3 Evolution of a heavy ion collision	6
1.4 Soft probes.	9
1.4.1 Anisotropic flow.	9
1.5 Hard probes	11
1.5.1 Jet measurements	11
1.5.2 Heavy flavour measurements	12
2 Charm as a probe of the QGP	15
2.1 Energy loss of heavy quarks	16
2.1.1 Collisional Energy loss.	16
2.1.2 Radiative Energy loss	17
2.1.3 Predictions and Measurements	18
2.2 Collective effects in the heavy-flavour sector	21
2.2.1 Modelling of the Quark Gluon Plasma and evolution	21
2.2.2 Hadronisation	22
2.3 Initial State effects	24
2.4 Tests of pQCD calculations with proton-proton collisions	27
3 Experimental setup	31
3.1 The Large Hadron Collider.	32
3.1.1 Accelerator updates during long shut down 1	32
3.2 The ALICE detector	33
3.2.1 Overview	33
3.2.2 V0	36
3.2.3 Inner Tracking System.	39
3.2.4 Time Projection Chamber.	41
3.2.5 Time of Flight detector	43
3.2.6 Tracks and vertex determination	45
3.2.7 Alice analysis framework	46

4	D-meson analysis strategy	47
4.1	Event selection strategy	48
4.2	Reconstruction strategy of the D^{*+} -mesons	49
4.2.1	Selection criteria	49
4.2.2	Signal extraction	55
4.3	Correction for apparatus effects: Monte Carlo studies	57
4.4	Correction for D^{*+} coming from beauty hadron decays	58
4.5	The $D^{*+} p_T$ -differential cross-section	59
4.6	Systematic uncertainty strategies	61
4.6.1	Raw yield systematic uncertainty	61
4.6.2	Tracking Uncertainty	64
4.6.3	Selection Criteria Uncertainties	66
4.6.4	Particle Identification uncertainties	66
4.6.5	Transverse momentum distribution uncertainty.	66
4.6.6	Feed-down correction uncertainty	67
5	D-mesons in proton-proton collisions	69
5.1	Results in pp collisions at $\sqrt{s}=5.02$ TeV and $\sqrt{s}=7$ TeV	70
5.2	Data sample at 13 TeV for D-meson analyses	73
5.3	Topological Cuts	76
5.4	Raw Yield Extraction	78
5.5	Efficiency Corrections	81
5.6	Systematics	82
5.6.1	Raw Yield Uncertainties	82
5.6.2	Variation of the topological selection cuts	84
5.6.3	Feed-down uncertainty	85
5.6.4	Tracking	85
5.6.5	Shape of the transverse momentum distribution in Monte Carlo simulations	86
5.7	Results	87
6	D-mesons in 5.02 TeV p–Pb collisions in run II	89
6.1	Open questions from run I.	90
6.2	p–Pb data sample	92
6.3	Topological Selection Criteria	94
6.4	Raw Yield Extraction	95
6.5	Efficiency Corrections	98
6.6	Systematic uncertainties	99
6.6.1	Raw yield uncertainty	100
6.6.2	Variation of the topological selections	103
6.6.3	Particle Identification - and Feed-down uncertainty	103
6.6.4	Tracking uncertainty	105
6.6.5	Total uncertainty on the Nuclear modification factor	106
6.7	pp-reference	106
6.8	Results	108
7	Discussion and Outlook	115
7.1	Outlook on the 13 TeV proton-proton results	116
7.2	Discussion on the p–Pb results at 5.02 TeV	117

7.3 Outlook on heavy flavour measurements	119
Appendix A: Invariant-mass-difference figures in pp collisions	123
Appendix B: Systematic uncertainties in pp collisions at 13 TeV	127
Appendix C: Topological selection criteria in p–Pb collisions	129
Appendix D: Invariant-mass-difference figures in p–Pb collisions	131
Backmatter	
Bibliography	135
Summary	143
Samenvatting	145
Acknowledgments	147
Curriculum Vitae	149

Introduction

This section gives a brief general introduction into the field of particle physics. We highlight some of the main measurements performed to investigate hot and dense Quantum Chromo Dynamical matter produced under extreme conditions of temperature and/or pressure.

1.1 The Standard Model and Quantum Chromo-dynamics

At the end of the 19th century the discovery of the electron by J.J. Thomson gave birth to the field of elementary particle physics. In the next 50 years many particles were discovered. However, the field as it is known today is governed by theories that were mainly proposed as recently as the second half of the 20th century[1]. In 1964 the quark model was proposed by Gell-Mann [2]. Originally it consisted of only 3 quarks: up, down and strange. Simultaneously, but independently, Zweig also came to the conclusion that there should be 3 smaller constituents in a baryon [3]. In that same year a fourth quark was proposed by Bjorken and Glashow[4]. They proposed this fourth quark based on the symmetry arguments as it would match the 4 leptons that were known at that time¹.

Theory predicted that new quarks should have associated particles, and starting with the ϕ -particle, such particles were found in the years after. With the discovery of the τ in 1975 the symmetry between the number of leptons and quarks was once again broken, and then assumed to be repaired when within 2 years the first particle containing a beauty quark was found. It took another 18 year to find the final (top) quark, which completes the quark and lepton model.

However, to understand nature a definition of the building blocks does not suffice, one also has to understand the forces between these building blocks. The Standard Model particle set is completed by adding the mediators of those forces, the so-called vector bosons: the photons for the electromagnetism, the W- and Z-Bosons for the weak force, the gluons for the strong force and finally the recently discovered Higgs-boson. This final particle was necessary to give the W and Z-bosons, amongst others, the appropriate mass and the Higgs-boson discovery completed the so-called Standard Model of Particle Physics [5].

¹These were the electron and muon and associated neutrino's.

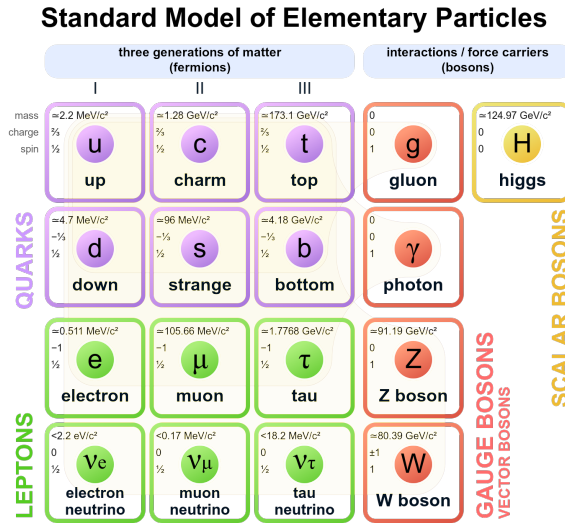


Figure 1.1: All discovered elementary particles as predicted by the Standard Model.

The focus of this dissertation will be on the strong force, this is the force that governs the interactions between quarks and gluons and makes it impossible to measure these particles on their own.

The theory governing the strong force, called Quantum Chromodynamics (QCD), is a non-abelian quantum field gauge theory based on a $SU(3)$ symmetry group. The quantum numbers associated with this force are called colour and there are three possible values for this force in a quark, namely: red, green and blue. The corresponding antiquark, on the other hand, has anti-colours. The force mediators, gluons, carry both one unit of anti-colour and one unit of colour. Interactions governed by this force consequently consists of the exchange of the colour charges.

Quantum Chromodynamics confines the quarks into hadrons and mesons, by forbidding free colour charges under normal circumstances. In order for all particles to be colour-less or white, one needs combination of either a quark-antiquark or a combination of three (anti)quarks which contain the three different (anti)colours². The confinement requirement implies that if one would try to separate a pair, the energy needed for this would be sufficient to create a new quark-antiquark pair. The second main concept of QCD, asymptotic freedom, means that there is a anti-screening effect of the quarks' color charge [7], [8]. The likely problem one may have with anti-screening is that the theory allows for runaway charges, this is actually countered successfully by the confinement criteria. Anti-screening effects also imply that if the length-scale between charges becomes very small, the force between them does so as well. An increase of the length scale would happen if one would try to separate two quarks further, or in practise when a particle is probed with lower energy scales. At small length scales, at high momentum transfer scattering, the strength

²While these are the most simple multiples possible, evidence of a pentaquark particle found in LHCb [6] proves that at high energies combinations of this configurations can also be possible.

of the coupling decreases. Mathematically this running coupling, called α_s , can be approximated as

$$\alpha_s(Q^2) \approx \frac{1}{\beta_0 \ln(Q^2/\Lambda_{QCD})}. \quad (1.1)$$

In this equation Q is the momentum transfer and Λ_{QCD} represents the scale where the perturbative description fails and the expression diverges. The potential of the strong force can be described using a Coulomb-like term and a confinement term,

$$V(r) = -\frac{4}{3} \frac{\alpha_s}{r} + kr \quad (1.2)$$

the Coulomb term of this potential can only be described in perturbation theory at small α_s .

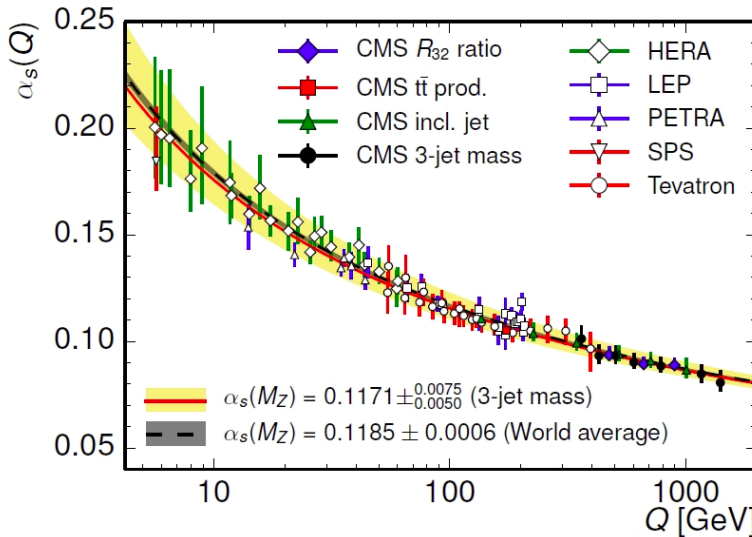


Figure 1.2: Coupling constant, α_s versus the momentum exchanged in the interaction Q . Figure from [9].

This implies that confinement itself can not be described perturbatively. However in the regime in which the coupling is large, lattice QCD [10] can be used to calculate the properties of the QCD. While QCD on a lattice allows for the confinement necessary and the perturbative region allows for the asymptotic freedom seen by the multiple experiments, the connection between the two regimes is non-trivial. The perturbative region breaks down for large values of α_s , while an infinitely fine lattice would be needed to fully connect both regimes. The agreement seen between QCD predictions and results of the large particle accelerator experiments quarks reinforces confidence that it is only a matter of time and computing power to be able to match both approaches.

1.2 The QCD phase diagram

However the anti-screening effects included lattice QCD allow not only for calculations in which the quarks are confined in particles. It also predicts that in conditions of high-energy density the confinement vanishes.

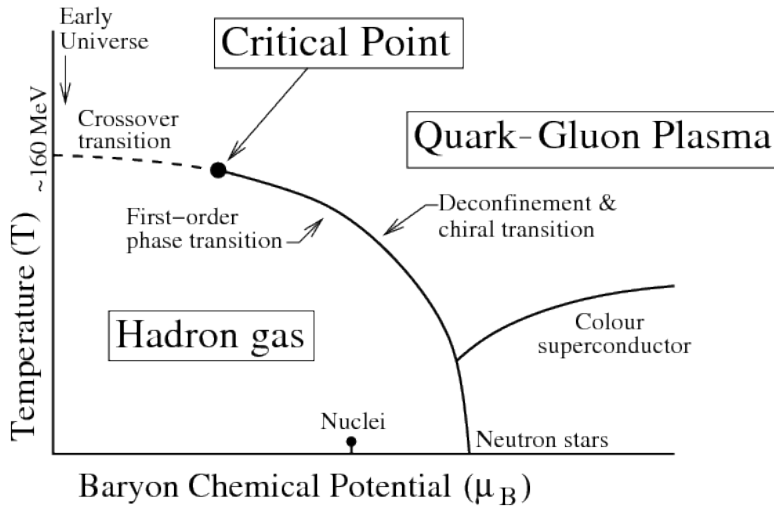


Figure 1.3: Schematic representation of QCD phase diagram in temperature via Baryon Chemical Potential. Figure from [11].

Deconfinement happens in a phase transition, which is dependent on the Baryon Chemical potential μ_B and temperature T and is schematically visualised in figure 1.3. The Baryon Chemical potential is a measure for the abundance of matter compared to antimatter, with zero indicating the same amount of matter and antimatter. At low temperature and or baryon density, quarks and gluons group into hadrons which form a hadron gas. If the temperature increases above the critical temperature, $T_C \sim 155$ MeV for low μ_B [12], quarks and gluons are deconfined. They are no longer bound into hadrons, but form a plasma. Cosmological models predict that a Quark-Gluon Plasma was formed in the early universe, which expanded and cooled down to a state of hadrons, as we find it in our current universe.

In order to be able to create this high density state of matter, this region of high temperature and low baryochemical potential is investigated with relativistic heavy ion collisions. These collisions are studied in colliders such as the Relativistic Heavy Ion Collider (RHIC) and the Large Hadron Collider (LHC).

Another new state of matter is expected at very high baryon chemical potential and low temperature. There a colour-superconductor state could be formed. This state of matter is theoritised to be found in neutron stars and is investigated in astrophysical studies [13].

1.3 Evolution of a heavy ion collision

Heavy ion collisions are studied at RHIC with gold, copper and uranium collisions. At the LHC lead and even xenon-ions have been accelerated at centre of mass energies of 2.76 and 5.02 TeV for lead-ions and 5.44 TeV for Xenon ions. In order to understand the behaviour of such a collision, one can identify various phases from the initial situation to the final measured particles. The difficulty is that measurements take place after the full evolution of the collision. Thus to understand these collisions we want to study not only the final-state effect but also identify the phase which is responsible for the effect. In chapter 2 we will discuss how different heavy flavour measurements allow us to probe different phases of the evolution.

Figure 1.4 shows a schematic of the different phases in such a heavy ion collision.

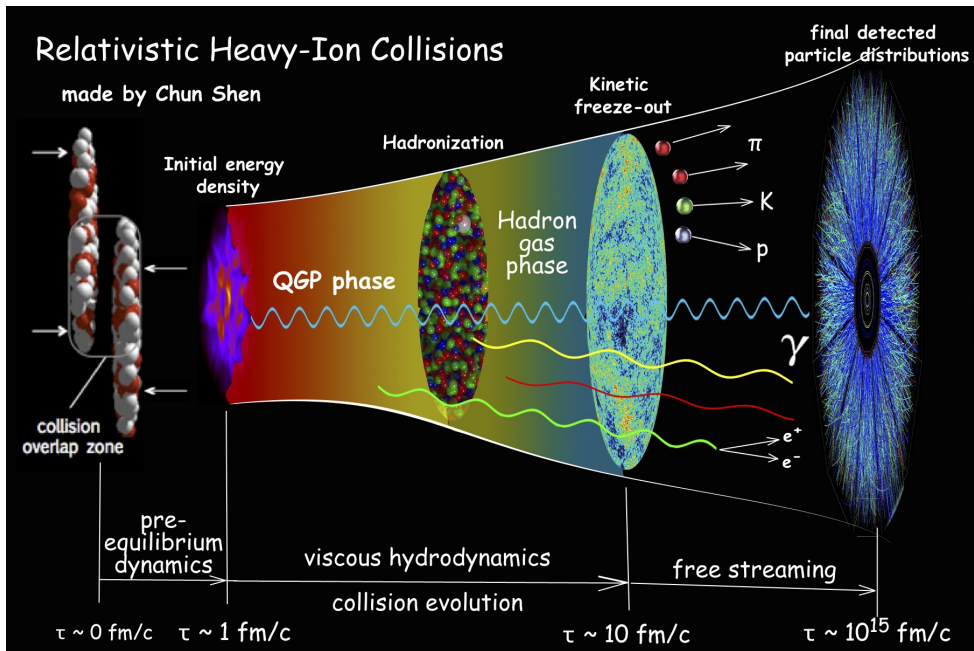


Figure 1.4: Visualisation of the dynamical evolution of a heavy-ion collision. Figure from [14]

The phases of a heavy-ion collisions will be discussed below. For a more complete review of the phases and the dynamical evolution see [15].

- ◆ **Initial collision stage**

The two Lorentz-contracted nuclei will consist mostly of gluons carrying a small longitudinal momentum fraction (low- x) and transverse momenta³. Perturbative QCD predicts that the gluon distribution would diverge for $x \rightarrow 0$, thus one of the questions is whether the gluon distribution would saturate and if so at what energy scale. The Color Glass Condensate model depicts a collision between two heavy-ion particles as colliding two sheets of gluons. These type of models use the existence of a saturation limit for gluon density in their calculations [16]. However it is also possible to do a calculation without considering a gluon-saturated initial stage and instead consider the spatial distribution of the participant from the overlap of nucleons in both nuclei which is done in a Monte Carlo-Glauber model. These initial stages are probed via proton-lead or deuteron-gold collisions and will be discussed more in depth in section 2.3.

- ◆ **Pre-equilibrium**

In this stage the particles collide and radiate softer gluons until they reach local thermal equilibrium. The duration of this phase cannot be measured directly, but is thought to last about 1 fm/ c .

- ◆ **Quark Gluon Plasma phase**

As the local thermal equilibrium is reached the quarks and gluon form a system with a small mean free path compared to the size of the system, this thermalised system with free (colour) charges is called a plasma. Such a system will influence both the directive distribution of the momentum space distribution of the partons as well as the energy of the outgoing partons. This system exists only till about 10 fm/ c , and the resulting quarks still go through the final step.

- ◆ **Hadronisation and freeze-out**

When the system cools down below $T_c \sim 155$ MeV, the phase transition into the hadron gas occurs. This proceeds via fragmentation and possibly via recombination of the available quarks⁴. After the chemical freeze-out quarks are hadronised. Therefore changes in hadronic species will mainly occur via decays. The particles do undergo elastic scatterings during the expansion of the system. Once the system is dilute enough these scatterings will also cease. This stage is called the thermal freeze-out phase after which no further changes in kinetic properties will take place.

At the moment of the initial collision, one does not know a priori what will be the size of the collision. The two nuclei or sheets of gluons do not have to hit each other head on, to be able to have a collision. The overlap between the nuclei is given by the impact parameter b , which is the smallest distance between the center of the nuclei at the time of the collision. If this distance is larger than two times the radius

³See [15] and references therein.

⁴Theoreticians are not yet in agreement with each other whether or not quarks hadronize via recombination instead of purely via fragmentation and if so what are the requirements for a quark to hadronize via recombination.

of the nuclei, there is no collision, if it is zero the collision is head on. Depending on this centrality the number of participant and spectator quarks and gluons to the collision may vary. The participants are defined as the nucleons that interact in the collision, and are thus scattered or otherwise directly influenced. The spectators, on the other hand may continue their initial path of flight and can only be influenced by a mean field present in the collision. From this description it is clear that in the case of a low impact parameter a large number of participants, i.e. a very high energy density of the collision and thus a large QGP is expected. For very peripheral collision at the same collision energy, in which the impact parameter is high, the created medium should be smaller and the particle density and thus the energy density will be a lot lower in these cases.

Measurements of an heavy ion collision are usually described in terms of so-called soft (low-momentum) and hard (high-momentum) partons. The majority of the soft partons is created mainly in the medium (i.e. the QGP). Hard partons are mainly produced in the earlier stages of the collisions and traverse the medium. For the hadronised final particles a separation between soft and hard probes is made based on the quark constituents and/or momentum of the particle of which the constituents could have traversed the quark-gluon plasma.

1.4 Soft probes

Both soft and hard probes can be studied in terms of particle yields and correlations between particles. Correlation measurements are done to study interactions inside the medium, so mainly between constituents of the medium, in order to further understand behaviour of the plasma. While particle yields are compared to pp yields in order to study the interactions of particles with the medium while traversing it. In hard probes one studies the effects of the medium on probes that interact with but are not part of that medium. In a correlation measurement for soft probes both particles are part of the medium, thus the the correlation effects related to medium features are expected to be larger compared to those of hard probes. In this section we will focus on anisotropic flow, which is mostly determined by the geometry of the collision and the collective expansion the system undergoes.

1.4.1 Anisotropic flow

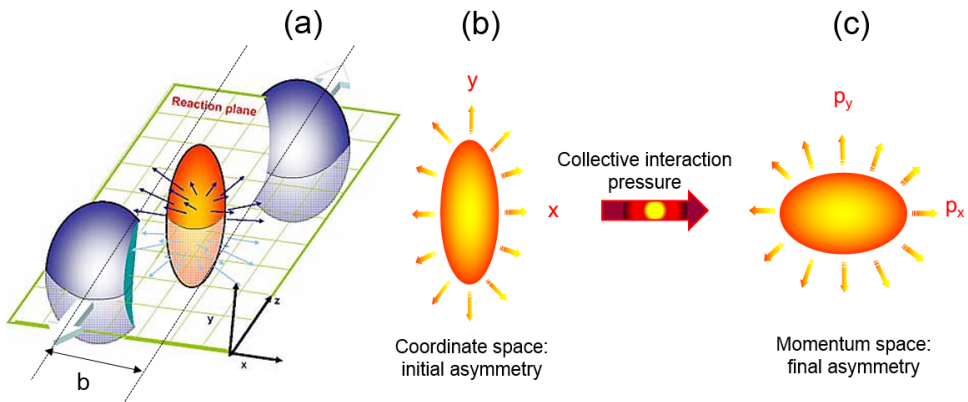


Figure 1.5: Schematic of a non-central heavy ion collision and the initial space and created momentum anisotropy. Figure from [17].

Before one can discuss the anisotropy of a collision, one has to start with a visualisation of a collision as shown in figure 1.5. The main principle of anisotropic flow is that an initial spatial anisotropy transforms into a final state momentum anisotropy in the transverse direction due to the internal pressure in the system. If a collision is fully head on, i.e. the impact parameter b is 0, there is no initial spatial anisotropy. In this case there will still be so-called radial flow, but it should not contain anisotropic flow. However if a collision is not fully head-on, and $b > 0$, the overlap region has an almond shape and thus has different pressure gradients with respect to the directions perpendicular to the reaction plane. These pressure gradients transform the system to a more symmetrical shape, and thus it results in a momentum anisotropy of the partons via the collective expansion of this almond shape liquid-state.

The reaction plane is spanned by the impact parameter and the beam axis, as schematically shown in figure 1.5. The momentum anisotropies are quantified via

the Fourier coefficients of the harmonic expansion of the particle azimuthal distribution relative to the reaction plane⁵. These coefficients v_n are called flow coefficients. The azimuthal angle corresponding to the reaction plane allows to calculate the flow coefficients as:

$$\frac{dN}{d[\phi - \Psi_n]} \propto 1 + 2 \sum_n v_n \cos(n[\phi - \Psi_n]). \quad (1.3)$$

In which Ψ_n denotes the azimuthal angle of the n -th harmonics initial state symmetry plane, and ϕ denotes the azimuthal angle for the particle, for Ψ_2 the reaction plane as defined in figure 1.5 is the average of the planes used. The first two coefficients are called the directed flow v_1 and the elliptic flow v_2 . The elliptic flow is sensitive to asymmetries of partons inside and outside the reaction plane as well as the internal viscosity of the plasma and as the largest of the harmonics, measurements of the v_2 are commonly used for research in these fields.

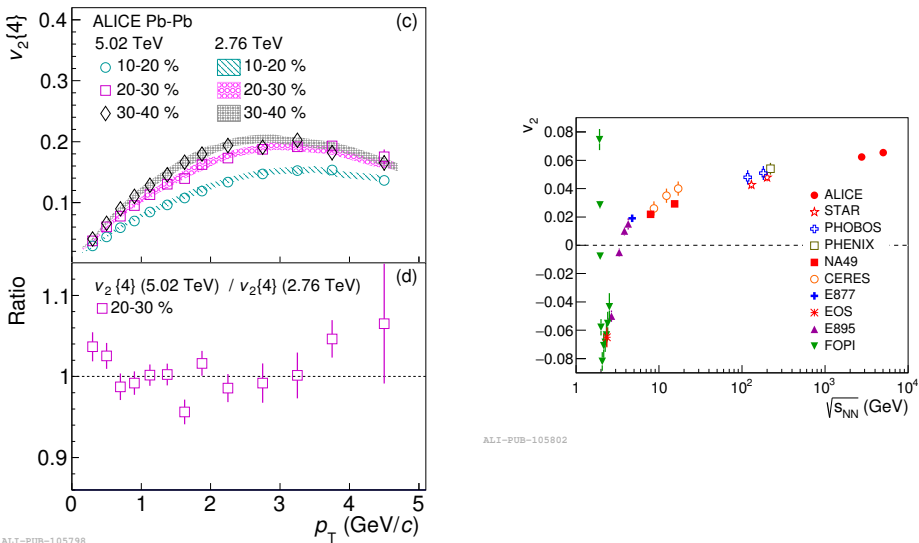


Figure 1.6: Left: $v_2(p_T)$ of charged particles in Pb–Pb collision at $\sqrt{s_{NN}} = 5.02$ TeV, with the results at $\sqrt{s_{NN}} = 2.76$ TeV shown as band. The lower panel contains the ratio between both. Right: Transverse momentum integrated v_2 measurements at various experiments and at various energies. Both figures from [18].

These elliptic flow measurements have been done for various energies at different accelerator complexes, the Super Proton Synchrotron, RHIC and the LHC, and seem to increase with higher energy. The p_T dependent measurement show compatible results for both the LHC energies⁶. This combination of results hints that the increase can be attributed to an increase in the mean transverse momenta. The elliptic flow is used for estimates of the shear viscosity of the Quark-Gluon

⁵Other symmetry planes would also suffice.

⁶And even between ALICE and RHIC, see [18].

Plasma, as the conversion efficiency from spatial to momentum anisotropy is dependent on the viscosity of the medium. Measurements at both RHIC and the LHC indicate that the Quark-Gluon Plasma behaves like a interacting fluid with very low viscosity $\frac{1}{4\pi} \leq (\eta/s)_{\text{QGP}} \leq \frac{2.5}{4\pi}$ [14].

As was shown in figure 1.5 the pre-expansion shape and thus the momentum space asymmetry depends strongly on the overlap between the two particles. Due to the size of a system one cannot force a collision with a certain overlap. Instead one can use centrality measurements to extract the level of overlap between the two colliding ions in hindsight.

1.5 Hard probes

Hard probes are defined as partons that are created due to hard scattering processes in the initial stages of the collision, measurements effects on the shape of the particle spectrum due to these processes are also called hard probe measurements. Two major examples of hard probes are jets and heavy flavour measurements. Jets are defined as collimated particles due to a shower of partons started from a very high energetic parton. The effect of the plasma on these jets is studied with respect to the jets in a near vacuum found in pp-collisions.

Heavy flavour measurements on the other hand allow to test the influence of the plasma on a heavy flavour parton.

1.5.1 Jet measurements

Jets are created both in ‘simple’ proton-proton collisions and in Pb–Pb collisions. In pp collisions these jets will be created, at first order, as two cones of particles, which are back to back to each other in the azimuthal direction. Such a 2-jet structure will mainly be created by a parton anti-parton pair and both jets will be similar in total transverse energy and momentum. However in Pb–Pb collisions partons may lose energy (a.k.a. jet quenching) and there is no a priori reason for the parton pair to be created in the centre of the collision, therefore one would expect one of the two partons to lose more energy⁷ in the plasma than the other as one will traverse a longer path through the plasma than the other. This jet quenching effect is schematically shown in figure 1.7

These measurements are complicated by the background in Pb–Pb collision which is, due to the flow effects, non-flat. In order to study jets a common strategy is to select a high-momentum particle and study the angular correlations between this and other particles. If the particles are part of this main jet there will be an enhancement around $\Delta\phi = 0$ while an away-side peak will appear at $\Delta\phi = \pi$. In order to limit background a selection is made on the transverse momentum on the associated particles as well.

⁷For methods of energy loss in the medium see section 2.1

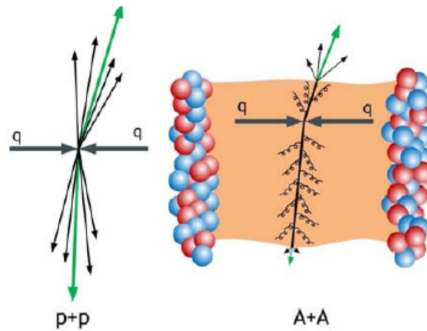


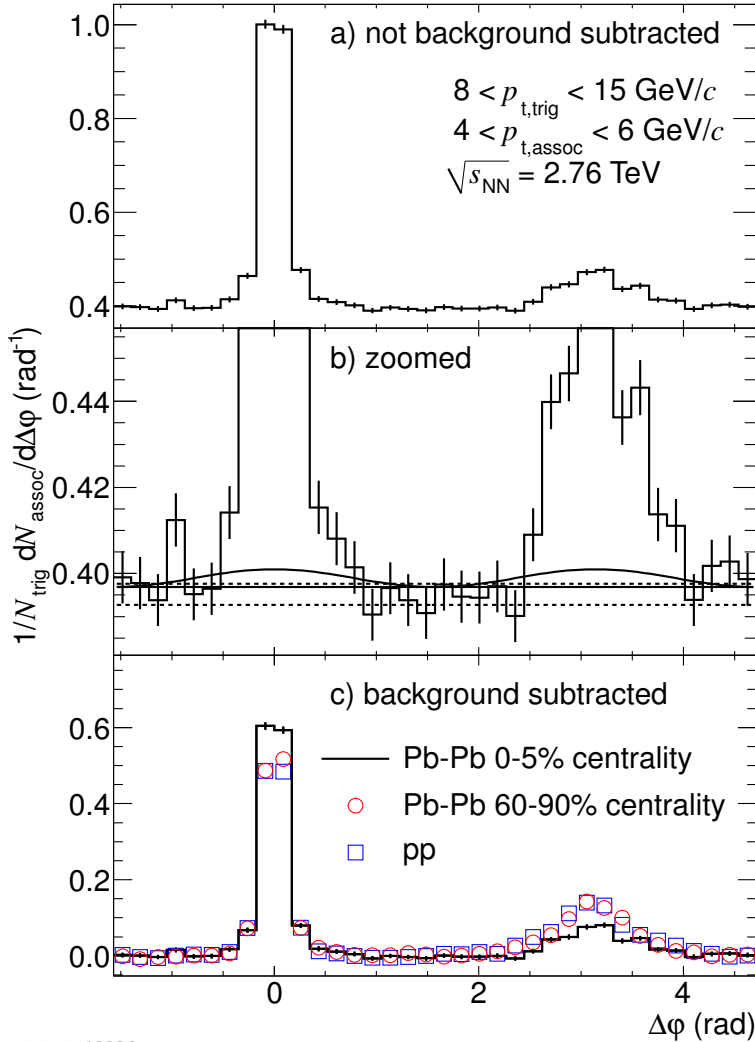
Figure 1.7: Cartoon illustrating illustrating a back-to-back set of jets in pp on the left and jet quenching on the right.

Comparisons of jets in proton-proton collisions to jets in central Pb–Pb collisions show a difference in the structure for the away side and near side peaks. The near side peak is significantly larger than the away-side peak and changes very little between pp and Pb–Pb collisions. The away-side peak is decreased due to the jet quenching in central Pb–Pb collisions, as observed in figure 1.8.

1.5.2 Heavy flavour measurements

Heavy flavour quarks, namely charm and beauty, are mainly created in hard-scattering processes at the early stages of the collision. The relatively high masses of 1.25 GeV for charm quarks and 4.2 GeV for beauty quarks are too high to be created via thermal production in the Quark-Gluon Plasma.

Therefore any heavy flavour particle consists of at least one quark that experienced the total evolution of the medium. The other(s) can either be created via gluon radiation or extracted from the medium via recombination. Because heavy flavour partons are guaranteed to experience the full evolution of the medium, the energy loss of such partons will result in a different p_T distribution for the yield for the associated heavy flavour hadrons compared to that of hadrons which do not contain partons created in the primary collision. While this is also the case for light flavour hadrons produced in the original collision, it is possible for all the partons of such a particle to be fully produced in the later stages of the collision. This makes heavy flavour a cleaner probe of the early stages of the medium. Measurements of heavy flavour particles, also have a down side, these particles have a short lifetime, therefore only the decay products of these hadrons can be measured in experiment. Any heavy flavour measurement is therefore done by reconstructing and identification based on the decay products. For heavier particles the decay can be sequential. As this dissertation will focus on these type of probes a more detailed description of the various heavy flavour measurements and the physics probed by these measurements can be found in chapter 2.



ALI-PUB-13896

Figure 1.8: Corrected dihadron yield per trigger pair for central Pb–Pb collisions in black, with results for peripheral Pb–Pb events in red circles and for pp events in blue squares. The upper figure (a) shows the results without background subtraction for central events, the middle (b) looks at the background level in more detail and shows the fitted pedestal and v_2 values used for the subtraction, while the lower panel (c) shows the background subtracted distributions. Figure from [19].

Charm as a probe of the QGP

In order to probe the Quark-Gluon Plasma, ideally a particle must exist throughout the full evolution of the medium but interact only during the QGP phase. As they at least satisfy the first criterium heavy flavour quarks are a very important probe. Due to the high mass most of the heavy quarks are created in the initial stages of the collision as the creation time for charm and beauty quarks is between $0.01 < \tau_{c,b} < 0.1 \text{ fm}/c$ [20] while the formation time of the Quark Gluon Plasma is $\tau \sim 0.3 \text{ fm}/c$ [21] at the LHC. Thermal production will not play a large role as the initial temperature of the Quark Gluon Plasma is not sufficiently high to create heavy quarks. Even at collision energies of 13 TeV in proton-proton measurements the effect of thermal production via thermalized matter is expected to still be minor [22]. The total charm or beauty cross-section is expected to be influenced very mildly by the Quark Gluon Plasma. The effect on the p_T -distribution and the overall phase-space distribution of the heavy quarks is expected to be larger. Heavy flavour hadrons can be further influenced due to the possible thermalisation of the heavy quarks and/or due to the influence of the QGP on the other quarks in the hadron. This could also influence the chemical composition of heavy flavour hadrons [23], [24].

2.1 Energy loss of heavy quarks

Heavy quarks traversing the medium can interact with its constituents and lose energy in the medium. The energy loss can occur via collisions, i.e. by hitting other partons, or via the radiation of gluons. In the following two sections energy loss is described in the formalism of a transport model. Transport models exploit the Quark-Gluon Plasma's liquid-like properties by using calculations based on (near) perfect fluid dynamics. While QCD-models describe the QGP energy loss via perturbative QCD calculations. These models assume the QGP behaves as a QCD medium without including explicitly the liquid-like properties of the medium. The main principles of the energy loss are model independent.

2.1.1 Collisional Energy loss

Partons that traverse the medium with a relatively low transverse momentum are theoretically expected to lose more energy due to elastic collisions with light particles than via radiation. As heavy quarks interact perturbatively and have a large mass, the propagation of heavy quarks can be modelled as Brownian motion. This allows one to estimate the behaviour of heavy quarks in the plasma using a Boltzmann transport equation. The collisional energy loss can be approached as a multiparton scattering. The BAMPS (Boltzmann Approach of MultiParton Scatterings) method [25] is one example of a model that uses the scatterings per parton to calculate the collisional energy loss.

If collisions of heavy quarks in the medium are described in a frame such that they are sufficiently forward peaked and/or only very little momentum is transferred in the collision, the Boltzmann equation can be simplified to Fokker-Planck dynamics [26]. This is the Fokker-Planck Langevin approach which significantly simplifies the transport equation [27]. In this formalism one has the Langevin equations, which in natural units are expressed as:

$$dx_i = \frac{p_i}{E} dt, \quad (2.1)$$

$$dp_i = -\Gamma(p)p_i dt + \sqrt{2D(p_i + dp_i)} dt \rho. \quad (2.2)$$

In these equations \mathbf{x} , \mathbf{p} are the position and momentum vector of the heavy quark, Γ is the drag coefficient, and D the diffusion coefficient. [28].

In the Langevin formalism the transport coefficients are included via the drag and diffusion coefficient, while in the Boltzmann approach they are introduced via the parton cross-sections. These coefficients can be calculated within a hard thermal loop approximation [30], as done for BAMPS (perturbatively with running α_s). Alternatively the transport coefficient can also be extracted from (thermal) lattice-QCD (lQCD), i.e. a non-perturbative calculation. It is important to note that the transport coefficients are depending on the mass of the parton, such that the drag and diffusion coefficients are proportional to $\frac{1}{m_Q}$. Therefore the transport coefficients predict a lower energy loss for heavy quarks than for lighter quarks.

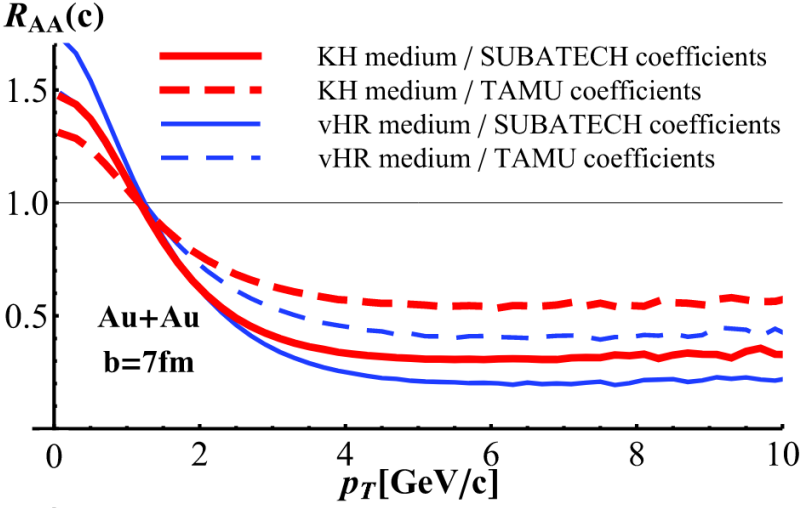


Figure 2.1: Differences between different microscopic (SUBATECH/TAMU) and bulk evolution, a hydrodynamical model by Kolb and Heinz (KH) vs elliptical fireball model by van Hees et al. (vHR) from [29].

Furthermore the evolution of the medium can also influence the collisional energy loss as the coefficients are dependent on medium properties. This implies that if the medium evolves the coefficients should change as well. Most commonly the medium evolution is modelled either as static fireballs, via hydrodynamical expansion or via different transport simulations [29]. Figure 2.1 shows an example of calculations for the nuclear modification factor with two different medium evolution models. In section 2.2 we will discuss collective effects and will elaborate further on the medium evolution, as collective effects are very sensitive to the evolution.

2.1.2 Radiative Energy loss

The second way a parton can lose energy in the medium is through gluon radiation, which is also called gluon bremsstrahlung. If a fast parton moves through a QCD medium it radiates gluons, similar to a QED charge radiating photons. From a theoretical point of view the intensity of the radiation is dependent both on the transport coefficient for the gluon, i.e. the way the medium is modelled, as well as on the nature of the parton radiating the gluon. The energy spectrum with respect to the path can be described, following [31], as:

$$\frac{dW}{d\omega dz} = \frac{\alpha_s C_R}{\pi\omega} \sqrt{\frac{\hat{q}}{\omega}}. \quad (2.3)$$

α_s denotes the QCD coupling constant, C_R the Casimir coupling factor of the parton, ω the gluon energy and \hat{q} the transport coefficient of the gluon. The transport coefficient is proportional to the density of scattering centres for the radiated gluon

and dependent on the medium model.

The colour dependence predicts a lower energy loss for quarks with respect to gluons as the energy loss spectrum is suppressed by a factor 2.25 as $C_R = 3$ for gluons and $\frac{4}{3}$ for quarks.

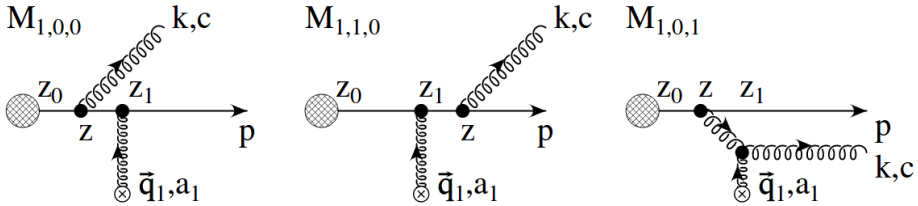


Figure 2.2: One-gluon leading order feynman diagrams, figure from [32].

Finally the mass of the radiating quark also effects the amount of gluon radiation, this effect is not taken into consideration in the previous formula. Including the quark masses in the calculations of the radiation amplitude via the appropriate one gluon Feynman diagrams, figure 2.2, leads to a distribution of soft gluons radiated by a heavy quark of:

$$dP = \frac{\alpha_s C_R}{\pi} \frac{d\omega}{\omega} \frac{k_{\perp}^2 dk_{\perp}^2}{(k_{\perp}^2 + \omega^2 \theta_c^2)^2}. \quad (2.4)$$

In which θ_c is equal to M/E if the quark mass M is much larger then the gluon mass [32] [31]. This implies that at angles less than θ_c gluon radiation is suppressed, and it seems to predict a mass-ordering amongst the quarks in terms of energy loss, such that a heavier quark should lose less energy than a lighter one.

However, while the dead-cone calculation is an elegant solution for the level of gluon radiation of a quark it does not take into account any possible medium effects. Instead it assumes that gluon radiation will behave the same in the medium as it does in vaccuum, which is not necessarily the case [33].

2.1.3 Predictions and Measurements

From the previous two section we expect different energy loss of gluons versus quarks and a mass ordering of the energy loss of quarks. These theoretical predictions are tested measurements using different particle species. It is assumed that by comparing the transverse momentum differential cross-section in proton-proton collisions to the yield in lead-lead collisions one would be sensitive to the energy loss of particles in the Quark-Gluon Plasma. This is done via the nuclear modification factor:

$$R_{AA} = \frac{1}{\langle T_{AA} \rangle} \cdot \frac{dN_{AA}/dp_T}{d\sigma_{pp}/dp_T}, \quad (2.5)$$

with N_{AA} the yield of the particle of interest per event in the lead-lead collision, $d\sigma/dp_T$ the transverse momentum differential cross-section in pp collisions and $\langle T_{AA} \rangle$ the average nuclear overlap function (Glauber model). If a nucleus-nucleus interaction would be equal to the superposition of the interactions of the separate nucleons, one would expect an R_{AA} of 1. However a deviation of this value does not have to imply an energy loss effect from a quark gluon plasma. Introducing a nucleus into the collision on its own could already influence the nuclear modification factor. Effects due to this change in the initial state are discussed in section 2.3. Returning to the effect of the energy loss on the nuclear modification factor a first question that might arise is: do we need to include both radiative and elastic collisional energy loss?

In figure 2.3 three models without radiative energy loss, namely BAMPS el.,

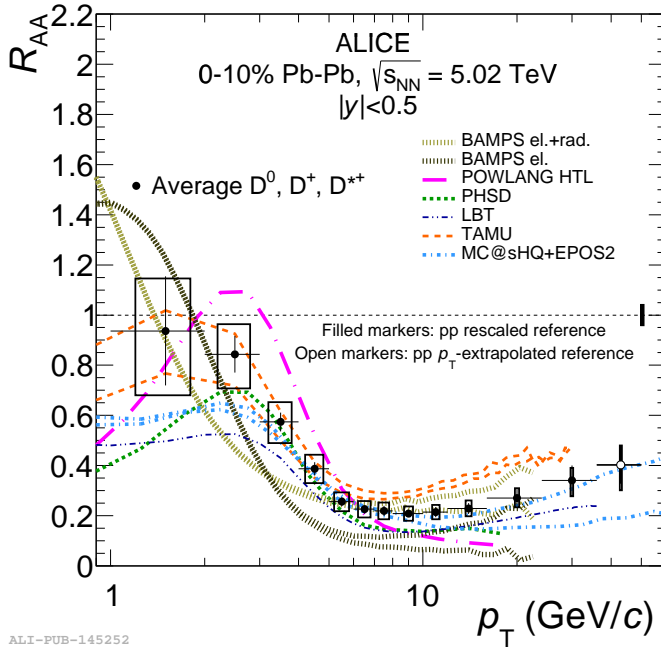


Figure 2.3: Nuclear modification factor as measured by ALICE for average of D^{*+} , D^0 and D^+ mesons, compared to several models, namely ,BAMPS (with and without radiative energyloss) [25], POWLANG [34], PHSD [35], LBT[36], TAMU[37] and MC@sHQ+EPOS2 [38]. For more on the models see section 2.2.1. Figure from [39]. For POWLANG PHSD and LBT a single central value of the theoretical prediction is included, for the others the upper and lower value of the uncertainty band of the prediction is indicated in the figure.

POWLANG and TAMU, are compared to various models in which both types of energy loss are included. For the higher momentum regions a slightly better agreement is seen for models that include both types of energy loss, while these models do not show a much larger disagreement at low momentum than those models including only one type of energy loss [39]. The nuclear modification factor on its own how-

ever is not sufficiently sensitive to some of the more subtle differences between the models. The shown (transport) models treat the medium-evolution, microscopic calculations and even the initial state in different ways, but as the models differ on various aspects it is not clear which of these differences are improving the agreement with the data.

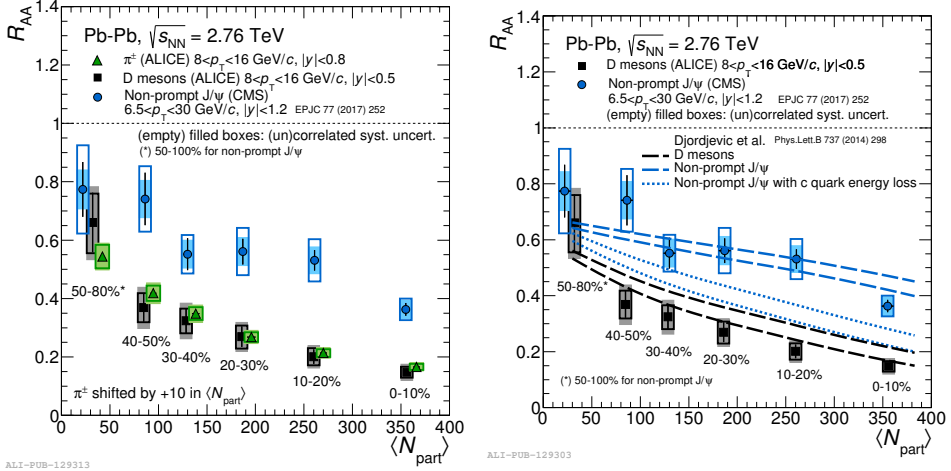


Figure 2.4: The nuclear modification factor of D mesons versus the number of particles in the collision with the corresponding centrality classes mentioned in the figures. These are compared to the values for J/ψ as measured by CMS, and on the left to the charged particles, dominated by pions, while on the right model calculations of Djordjevic [40] are included, figures from [41].

If D-meson (charm) results are compared to the pion nuclear modification factor and the non-prompt J/ψ 's one sees in figure 2.4 that the D-mesons agree quite well with the pion results. A non-transport model, which models the Quark-Gluon Plasma rather as a thermal QCD medium, namely the model by Djordjevic [40], is capable of describing both J/ψ and D-meson results. In this model the agreement between the pion and charm R_{AA} can be explained as the charm and gluon/light-quark p_T distributions and fragmentation compensate the charm-quark mass effects [42].

Both transport and non-transport models have been shown to be in agreement with the experimental R_{AA} . Transport models do have another advantage, they can simultaneously predict possible collective effects and nuclear modification factors, as this comes naturally from the description of QGP as a liquid. Non-transport models do not include flow effects and thus if that is the way of nature, a second theory will be needed to explain those results.

2.2 Collective effects in the heavy-flavour sector

A theoretical description of the effects of the quark-gluon plasma on heavy flavour hadrons contains several ingredients:

- ◆ a production mechanism, which one can test against proton-proton or proton-lead collisions to include the correct parton density functions ¹,
- ◆ a method to interact with the medium, for instance via energy loss as discussed in the previous section
- ◆ a model of the medium evolution
- ◆ a hadronization or recombination method for the heavy quarks.[20]

The proton-proton and proton-lead collisions probe the first part of the theory, and the second point is specifically probed by the nuclear modification factor R_{AA} . The effects of the third and fourth bullet points on these measurements are not easily distinguishable from each other in energy loss measurements. Other measurements of the effects of collectivity on heavy flavour hadrons are more sensitive to these effects.

Due to the early production of heavy flavour quarks, the elliptic flow of heavy flavour hadrons is sensitive to different parts of the modelling in different transverse momentum ranges. At the lowest transverse momentum the degree of thermalization of the heavy quarks in the medium is probed. Secondly at intermediate transverse momenta the sensitivity to the hadronization via fragmentation and possible recombination with other quarks is probed. Finally at high transverse momenta the path-length dependence of the energy loss is probed, as particles in the direction of the reaction plane follow, on average, a shorter path through the medium than particles perpendicular to that plane [43]. The inclusive v_2 for heavy-flavour decay electrons can be measured without identifying the corresponding heavy flavour hadron. While this allows for a smaller statistical uncertainty it is harder to relate the transverse momentum distributions to that of the heavy flavour hadron. A D-meson v_2 measurement allows for an easier correspondence between the energy loss and flow predictions for theoretical models. Collectivity predictions are more sensitive to the medium modelling and hadronization with/without recombination methods. In section 2.2.2 the hadronisation is discussed in the context of the v_2 measurements as well as a model comparison to v_2 and R_{AA} results.

2.2.1 Modelling of the Quark Gluon Plasma and evolution

One of the big differences between various models is how they incorporate the medium and/or its evolution. QCD-type energy loss models such as the model by Djordjevic [40] describe the QCD medium as a static fireball and incorporate the energy loss of partons in the medium via pQCD calculations. The Djordjevic model works well for energy loss for multiple particle species but does not give a prediction for the heavy flavour flow.

A bit more evolution is included in PHSD[35] which treat everything microscopically, but includes Quark Gluon Plasma modelling via dynamical quasi particles.

¹in which cold nuclear effects could be included

The second option uses transport coefficients and includes an embedding in so called (2+1)d viscous fluid dynamics. This approach is used by POWLANG, a powerlaw Langevin approach [34], Duke, also a langevin approach [44] and LBT [36], which stands for Linear Boltzmann Transport. (2+1)d viscous fluid dynamical models assume that the Quark Gluon Plasma is a near perfect liquid in the sense that the viscosity does not fully vanish as would be in a perfect liquid. A small amount of viscosity during the plasma evolution is assumed in these calculations, so relativistic viscous fluid dynamics are used to model the fluid in the early phase of the Quark Gluon Plasma ².

BAMPS [25] and MC@_SHQ+EPOS2 [38] start from the assumption of a non-viscous fluid and use a (3+1)d ideal-fluid-dynamical evolution, with a perfect liquid in the earliest stages of the plasma.

Next to these three types there are also attempts to modify the models to fit the evolution better. TAMU[37], for instance, has made amendments on a (2+1)d ideal-fluid dynamics model to generate a more violent transverse expansion of the medium. They have included lattice QCD equation of state predicting a smooth transition between the states instead of a first order transition into the hadron-resonance gas.

2.2.2 Hadronisation

All model calculations with results on heavy flavour hadrons that are reported in this thesis include a form of fragmentation. Most models shown here transform partons into hadrons via parametrised fragmentation functions from FONLL[45],[46]³ or PYTHIA. BAMPS [25] and the model by Djordjevic [40] assume this as the only

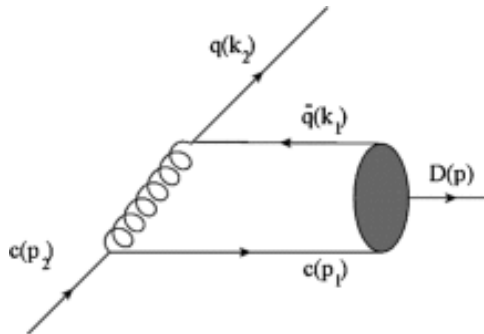


Figure 2.5: Leading order fragmentation D-meson production.

source of hadronisation for heavy quarks.

Other models have included some form of recombination as well, i.e. the heavy quark does not only hadronise via its own shower but also couples to light quarks in the medium. This allows heavy flavour hadrons to acquire some of the flow the light

²See [20] and references.

³See section 2.4

quarks have acquired via their thermal production. For the recombination the most common model is the Instant Coalescence Model [47] which recreates the appropriate light quark sample and then recombines with the heavy quarks. TAMU[37] and POWLANG[34] use different approaches; for TAMU a resonance recombination model is applied, which exploits resonant quark-anti-quark scattering amplitudes within a Boltzmann equation. POWLANG uses an in-medium fragmentation scheme extracting a light anti-quark from a thermal momentum distribution and creating a string with respect to the corresponding quark⁴ [48].

In figure 2.6 the energy loss results for central events and the elliptic flow results

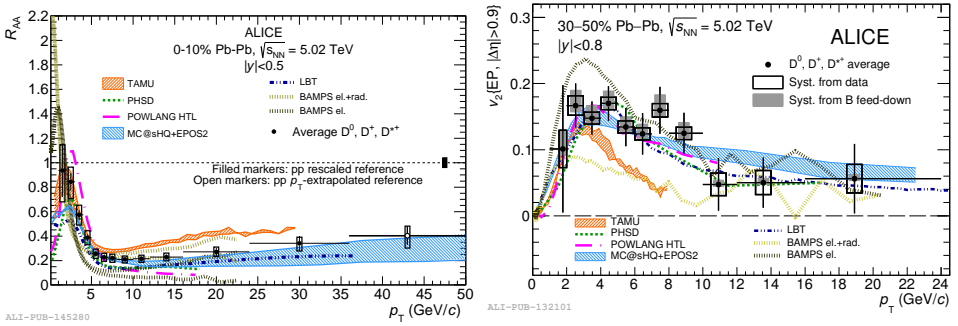


Figure 2.6: The nuclear modification factor of D mesons in most central collisions compared to the D-meson v_2 on the right with respect to transverse momentum of the D-meson compared to model calculations of BAMPS (with and without radiative energyloss) [25], POWLANG [34], PHSD [35], LBT[36], TAMU[37] and MC@sHQ+EPOS2 [38].

for mid-central events are compare to theoretical calculations that are available for both cases.

As one can see most theoretical curves are in agreement with data and each other, however the combination of both measurements does allow for some constraints. For instance TAMU underestimates the v_2 and overestimates the R_{AA} probably due to the fact that it includes only collisional energy loss. For BAMPS one can see that including the radiative energy loss improves the R_{AA} description, but underestimates the elliptic flow. For those models that nicely fit the estimation of the flow coefficient, there is some tension in the description of the R_{AA} . In order to further distinguish between models and to make sure these effects are due to a Quark Gluon Plasma, the initial stage effects can be better controlled by testing for possible cold nuclear effects. In the next section possible cold-nuclear effects will be discussed.

⁴This last method requires the created string to be heavy enough to create a pair of hadrons, and assumes a fragmentation of the light quark string.

2.3 Initial State effects

The previous two sections focussed on possible effects of the Quark Gluon Plasma, and the heavy flavour measurements used to further understand this medium. However in addition to the Quark-Gluon Plasma created in Pb–Pb collisions, there could also be effects due to the fact that nucleons inside a nucleus have different properties than free nucleons. The effects of colliding nuclear matter with respect to that of colliding separate particles are called Cold Nuclear Matter (CNM) effects. Distinguishing between Cold Nuclear Matter and Quark-Gluon Plasma effects is only possible by measuring the effect of a nucleus on a collision in a situation in which one does not expect a Quark-Gluon Plasma to be formed. This is the main motivation for the measurements in proton-lead collisions at ALICE.

The effects of a nuclear initial state are attributed to different sources depending on the initial state model. Partons possibly behave differently in a proton than in a nucleon due to the density of partons in a nucleon. The behaviour of a parton can be modelled depending on its longitudinal momentum fraction x and the scale of the parton parton interaction, Q^2 . Such modifications are included in so called nuclear-modified Parton Density Functions (nPDF). While the sizes of the effects are theory dependent one can usually identify:

- ◆ a shadowing region, lowering of the nPDF at small $x \lesssim 10^{-2}$,
- ◆ A possible anti-shadowing regime at $10^{-2} \lesssim x \lesssim 10^{-1}$ which is related to phase-space saturation,
- ◆ After which some models include a depletion in the so called EMC regime $x \gtrsim 10^{-1}$,

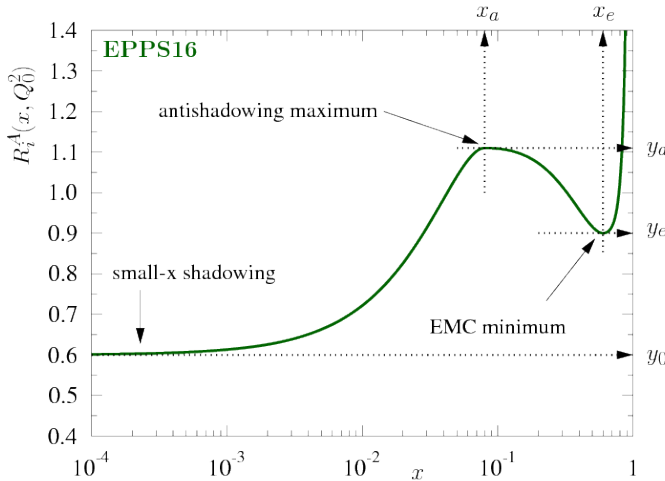


Figure 2.7: Illustration of the EPPS16 scale dependent nuclear modification fit function $R_i^A(x, Q^2)$ from [49], a model which uses a fit to DIS data combined with a DGLAP evolution.

Models which include nPDF's normally extract the strength and range of each region via fits to DIS or LHC proton-lead data. The densities are parametrized at large enough Q^2 and evolved with DGLAP evolution, as for instance EPPS16 [49] in figure 2.7.

Instead of modifying all parton distribution function of partons to one in a nucleus one can also describe the physics at small x within a Colour Glass Condensate (CGC) framework. Colour Glass Condensate frameworks assume that in these extreme situations the nucleus is dominated by the gluonic distribution to such an extent that it can be described as a thin sheet of gluons. Depending on the formalism, the same approach is sometimes used for something as small as a proton, assuming a much smaller sheet of gluons. These sheets are expected to have a finite density, considering that while the gluon density should grow when one reaches lower x the gluon occupation number will saturate due to gluon-gluon interactions at high densities⁵.

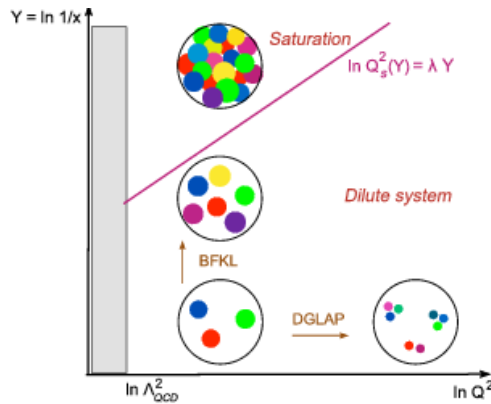


Figure 2.8: Schematic of a phase diagram for the parton evolution in QCD with the saturation line indicated in which Q^2 is the saturation moment, Y the rapidity and λ the saturation exponent. Figure from [16].

Such Colour Glass Condensate models calculate the gluon saturated situation by evolving it from a low rapidity low energy situation via a Balitsky-Kovchegov or JIMWLK non-linear evolution equation approach to the high rapidity situation.

Finally one can also assume that for the collision itself there are effects of multiple scattering of the colliding partons in the nucleus. These scatterings can occur both before and after the hard scattering, which should lead to radiative or collisional parton energy loss and a transverse momentum broadening of the resulting partons. The transverse momentum broadening due to multiple scatterings of the colliding partons is also called the Cronin effect. The modification it causes is illustrated in

⁵For more on this see [16] and references there in.

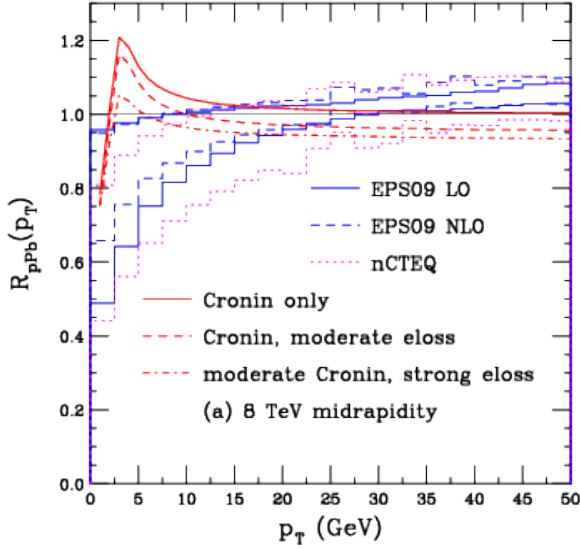


Figure 2.9: Predictions for 8 TeV p-Pb collisions for the R_{pPb} for D-mesons, showing in red different combinations of the strength of the Cronin effect and parton energy loss due to the multiple scattering of Vitev [50] compared with in blue the earlier discussed shadowing. For the shadowing EPS09, [51] is used as well as nCTEQ [52] with the results calculated with the data-driven framework of Lansberg and Shao [53], figure from [54].

figure 2.9 via the predicted R_{pPb} which is defined similarly to the R_{AA} as,

$$R_{pPb} = \frac{1}{A} \cdot \frac{d\sigma_{pPb}/dp_T}{d\sigma_{pp}/dp_T}, \quad (2.6)$$

in which σ_{pPb} represents the proton-lead cross-section and nuclear number A is used to scale the cross-section from p-Pb to pp collisions.

While a Quark-Gluon Plasma is not expected in proton-lead or high multiplicity proton-proton collisions there have been results hinting to some form of collectivity in those collisions. Therefore some Pb-Pb energy loss models also give predictions for proton-lead collisions assuming a small QCD medium in proton-lead collisions. For instance the POWLANG theoretical approach⁶ provides predictions in proton-lead.

An overview of the different Cold Nuclear Matter effects for heavy flavour particles can be found in [20].

⁶see sections 2.1 and 2.2

2.4 Tests of pQCD calculations with proton-proton collisions

In order to fully understand complicated systems such as p–Pb and Pb–Pb collisions a good understanding of proton-proton collisions is paramount. Precision probing of the Quark-Gluon Plasma effects, do not only require a precise measurement in Pb–Pb collisions but also a stable and precise measurement in proton-proton collisions to serve as a baseline. Measurements of heavy flavour hadrons in proton-proton collisions allow probing of the high-energy regime in which pQCD calculations give predictions. This is due to the fact that the mass of the charm quark, is significantly higher than $\Lambda_{QCD} \approx 0.2$ GeV, while for light quarks pQCD is only applicable above a high momentum scale.

The nuclear modification factor is calculated from measurements of the transverse momentum differential cross-section in proton-proton and p–Pb collisions as defined in 2.3 and with respect to the Pb–Pb yield as defined in section 2.1.3 . To be able to understand this cross-section and the theoretical prediction it helps to separate the production of open heavy flavour in perturbative and non-perturbative aspects;

- ◆ Non-perturbative: initial conditions described by Parton Density Functions (PDF's) which are parametrizations of the parton distributions as a function of the parton momentum fraction x and the squared momentum transfer of the process Q^2 . These PDF's have been studied extensively in Deep Inelastic Scattering processes.
- ◆ Perturbative: partonic scattering cross-section. Theoretical calculations are performed using perturbation theory at a given order, for heavy flavour this is currently available at leading order (LO) or next-to-leading order (NLO). In leading order only gluon fusion and quark-antiquark annihilation contribute to the heavy flavour production. At next order gluon splitting and flavour excitations are also included in the calculations.
- ◆ Non-perturbative: fragmentation of the quarks into open heavy flavour hadrons, in which both the quark and antiquark fragment into hadrons. The probability that a certain parton of momentum P fragments into a specific hadron h with momentum fraction $z = p/P$ is described by fragmentation functions, which are measured in electron-positron experiments [24].

Two theoretical calculations that can be used to describe the production cross-section are FONLL [45],[46], Fixed Order Next to Leading Log, and POWHEG [55], POSitive Weight Hard Event Generator. POWHEG only includes the first two steps and one has to combine it with an event generator to include the possibility for parton showers and the hadronization process, such as HERWIG[56] or Pythia[57]. A further difference between these two methods is that FONLL combines a fixed next-to-leading order (NLO) QCD calculations with an all-order resummation to next-to-leading log (NLL) accuracy in the limit where the transverse momentum of the heavy quark is much larger than its mass. POWHEG, on the other hand, uses a NLO+PS (Next-to-leading order plus parton shower) model including gluon split-

ting only to lowest order while the use of a resummation scheme allows FONLL to include higher order for high momenta partons.

In addition to POWHEG, one could alternatively consider MC@NLO. However MC@NLO calculations are done with an HERWIG-event generator background, while for the current measurements at ALICE a Pythia event generator is used.

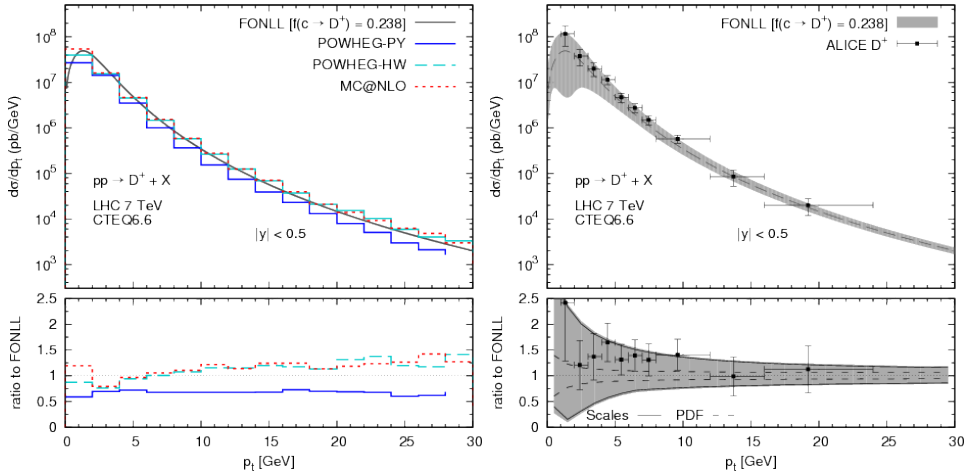


Figure 2.10: Left: Predictions for 7 TeV pp collisions from, POWHEG with HERWIG and Pythia MC@NLO+HERWIG and FONLL. Right FONLL predictions versus ALICE measurements with uncertainty, the shaded is full uncertainty, the dashed the uncertainty due to PDF's and the solid the uncertainty due to renormalisation and factorisations scales from [45].

In figure 2.10 the ratio between the central values of the models is shown in the lower panel⁷.

For the FONLL calculations the uncertainties can be split into uncertainties on the parton density function, the renormalisation and factorisation scales and heavy quark mass variation. The fragmentation fractions per hadron as well as fragmentation functions and decay branching ratios influence the total uncertainties of the prediction as well, but are not considered as internal model uncertainties.

The uncertainty of the PDF's is dependent on the PDF model that is used for the predictions. On the other hand, the renormalisation and factorisation scales uncertainty is acquired by variations around a central hypotheses of $\mu_R = \mu_F = \mu_0 = \sqrt{p_T^2 + m^2}$ where the mass and momentum are that of the heavy quark. The uncertainty-band corresponding to the uncertainty on the energy scales is extracted by independently varying the values of μ_r and μ_f between half and double of the central value and the envelope of the results is used as the uncertainty. The central value of the charm quark is $1.5 \text{ GeV}/c$ and it is varied to $1.3 \text{ GeV}/c$ and $1.7 \text{ GeV}/c$. The corresponding uncertainty is included as independent uncertainty with respect to the previously

⁷These results and have been achieved in 2012 and while more precise results are available today, these results show nicely how the comparison between data and theory can be made.

mentioned uncertainties. Here, the uncertainty is estimated while the renormalisation and factorisation scale as well as the PDFs are kept at their central hypothesis. All three uncertainties are considered independently and are quadratically summed to give the final uncertainty on the theoretical calculation. In order to further test these cross-section predictions in terms of energy universality proton-proton collision results are also compared to each other, which allows for a cancellation of correlated uncertainties such as the uncertainties on the heavy quark mass, fragmentation fractions per hadron as well as fragmentation functions and decay branching ratios.

Therefore a ratio-measurement will have smaller uncertainties on the theoretical predictions, while it still depends on the PDFs. This cancellation of other sources of uncertainty makes measurements at very low D-meson momentum at different collisions energies a relevant source to further constrain the PDFs in a range where DIS measurements cannot reach in this range the PDFs will mostly be gluonic of nature [46].

Experimental setup

Fundamental particle physics can be studied either by measurement from astroparticle physics, via measurements of particles that reach earth from various sources in the universe, or via particle collisions created in a laboratory setup. Both measurements probe different parts of the field of particle physics, one of the advantages of measurements in a laboratory set-up is the ability to control and change such a setup. With high-energy particle accelerators QCD measurements are done at various energies and in various colliding systems. To be able to probe a Quark-Gluon Plasma an accelerator is needed that is capable of accelerating heavy ions, such as gold or lead and colliding them at very high energies to reach the necessary temperature at a given baryon density. For the measurements it is crucial to use a detector that provides precision measurements under the extreme conditions of a heavy ion collision.

3.1 The Large Hadron Collider

Located at the French-Swiss border close to Geneva, the Large Hadron Collider (LHC) is the largest and most powerful particle accelerator currently available. The Large Hadron Collider is part of the “Conseil Européen pour la Recherche Nucléaire”, or European Council for Nuclear Research and has been approved in design as early as 1994. The LHC was built using earlier colliders in the tunnels of LEP, which was the largest electron positron collider of that time. It is part of a larger accelerator complex, in which protons, lead ions, and even xenon ions, are accelerated in various accelerators with the LHC-ring being the final step. Protons are injected into the Proton Synchrotron Booster (PSB) after having received a first acceleration in the Linear Accelerator (Linac2 in this case). After this booster they enter the Proton Synchrotron, and consequently the Super Proton Synchrotron, which after reaching 450 GeV allows them to enter the Large Hadron Colliderring, where the protons, separated in two beams going in opposite directions, are accelerated to their final collision energies. For ions the preacceleration is done in the Low Energy Ion Ring (LEIR) instead of the Linac2, after which they follow the same path, with the addition of an ion selection after the Proton Synchrotron [58].

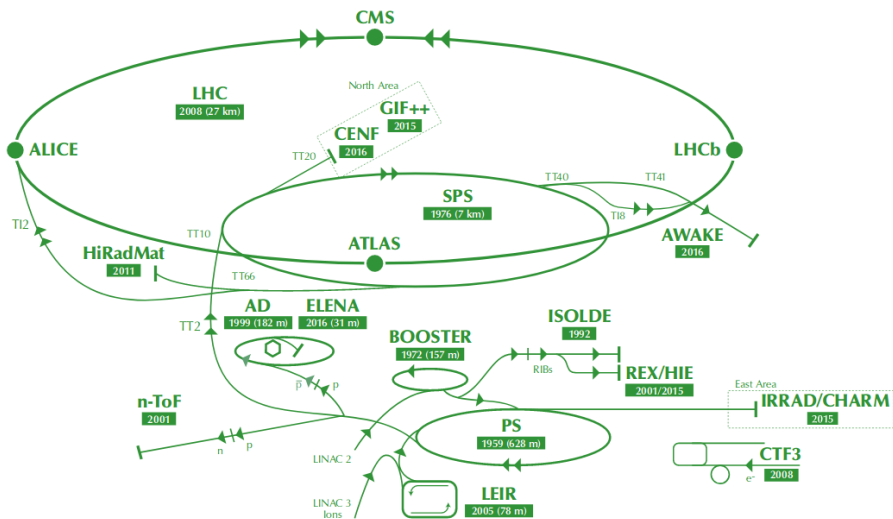


Figure 3.1: Schematic of the different parts of the CERN accelerator complex, including various experiments. Figure from [58].

There are four main experiments located around interaction points, at these points the oppositely travelling bunches of particles are steered to collide with each other.

3.1.1 Accelerator updates during long shut down 1

The first run of the LHC lasted from 2009 till 2013. This run was extended by a few weeks with respect to what was originally planned as a result of the Higgs-boson

measurements. However, early 2013 the LHC was turned off, to be updated and improved for both the machinery and detectors till the second run that started on the 5th of april 2015. While the LHC was originally designed for a centre-of-mass energy of 14 TeV in proton-proton collisions, during run 1 it was not possible to increase the energy above 8 TeV.

This was mainly due to the major magnet quenching experienced at the start of LHC, which made it necessary to introduce new consolidation and safety methods before the magnets could be ramped up to the energy necessary for 13 TeV.

In particular the splices that interconnected the LHC cryo-magnets, which are used to accelerate and focus the beams in the main ring, needed to be prepared.

New measurements and realignments of the magnets in the PS, PSB, SPS took place and faulty magnets were replaced if necessary during the shutdown. Even the beam-pipes leading to the experiments were checked and either reinstalled or replaced if necessary and finally beam position monitors were installed. The combination of all these replacements and actions resulted in a very tight schedule for the first long shutdown [59]. However in run 2 the LHC has been able to deliver a much larger luminosity of collisions, for Atlas and CMS 160 fb^{-1} was delivered¹, in comparison a little under 30 fb^{-1} was received by these experiments in run 1 of the LHC. Most collisions used protons at $\sqrt{s} = 13 \text{ TeV}$, but there was also an increased luminosity for Pb–Pb and p–Pb collisions at 5.02 TeV. On top of that there were p–Pb collisions at 8.16 TeV and the first Xenon-Xenon collisions.

3.2 The ALICE detector

The detector setup used in this thesis is the ALICE detector. ALICE stands for A Large Ion Collider Experiment and it studies mainly the strong interaction (QCD) with the focus on heavy-ion collisions. The QGP is studied via measurements in Pb–Pb, Xe–Xe and p–Pb collisions. Measurements in p–p collisions are also taken with the ALICE detector. These measurements serve as a baseline and also provide relevant physic data in those area's where ALICE measurements can compete with other LHC experiments. The ALICE detector has excellent tracking and particle identification capabilities allowing precision measurements in the high multiplicity experienced in Pb–Pb collisions, being sensitive enough to differentiate between the various low momentum particles. This is the reason that the detector is build for, in LHC standards, relatively low interaction rate as was expected in Pb–Pb collisions. As it includes relatively slow detectors such as the Time Projection Chamber and a Silicon Drift Detector [60].

3.2.1 Overview

The ALICE detector contains many different subdetectors, of which those crucial to the D^{*+} -meson measurements will be highlighted. The detectors of ALICE can be

¹A lower luminosity was delivered to ALICE and LHCb as these high precision detectors did not have the capabilities to do their specific jobs at such high luminosity. These detectors instead need a high stable beam time to collect as many separate collisions as possible, and also got a significant increase in data in run 2.

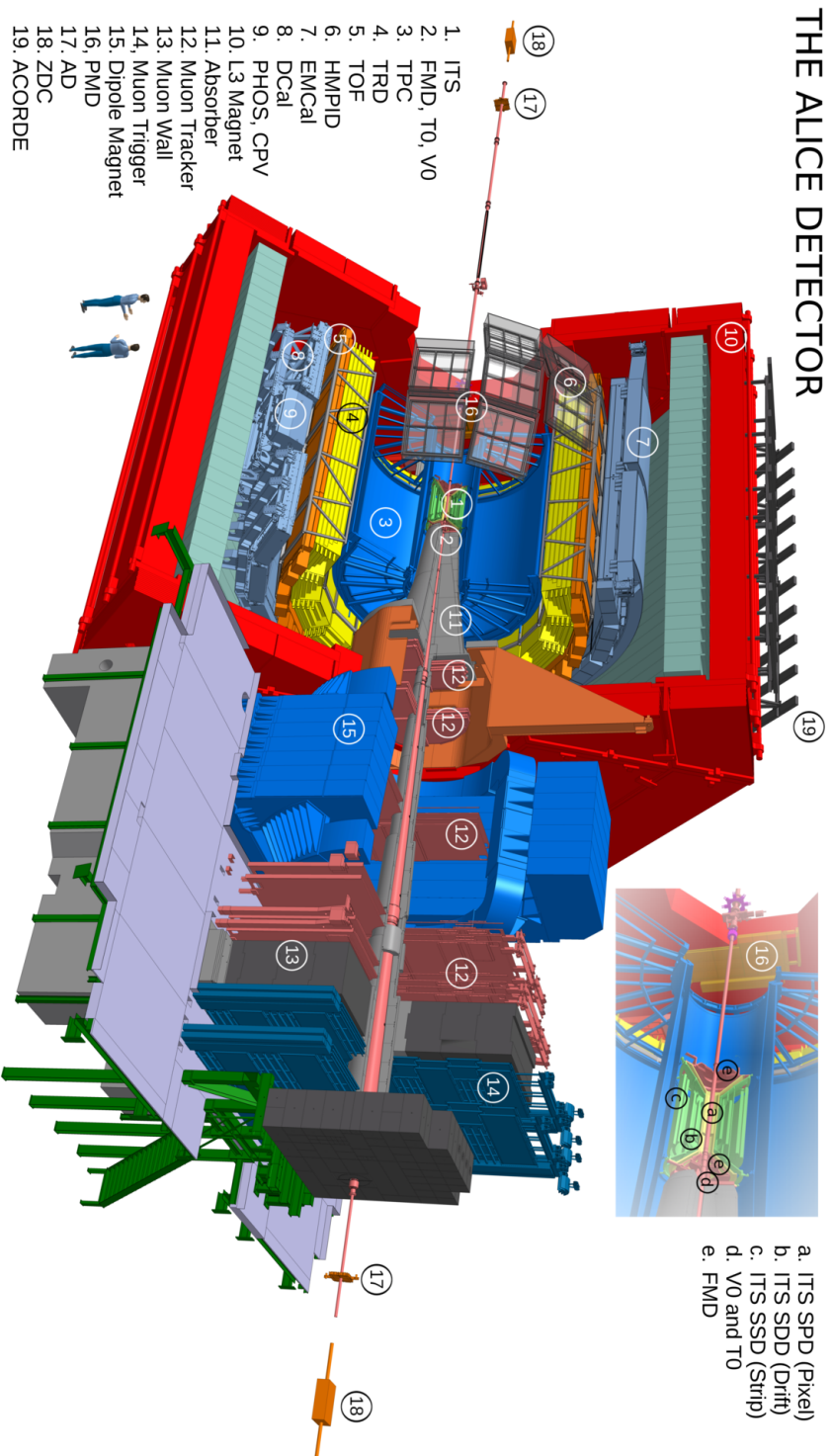


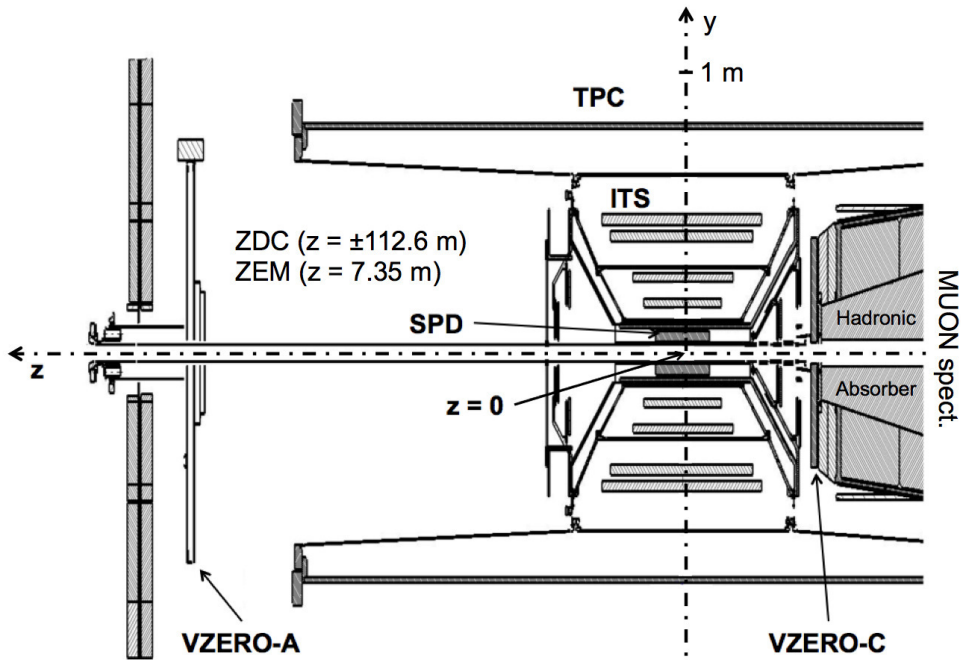
Figure 3.2: Schematic overview of the ALICE detector as available in run 2 of the LHC.

divided based on their rapidity coverage between those contained in the central barrel $|\eta| < 0.9$ and those outside of it. On the outside it contains the T0 trigger detector and the Muon arm. Moving inwards one finds the V0 detector located on the edge of the central barrel. This provides trigger and centrality measurements and a more detailed explanation can be found in section 3.2.2. The central barrel is contained in a large red magnet, this magnet was already placed here in the time of LEP. From outside moving inwards one can then find: the electromagnetic calorimeter (EMCal), PHOS, the TRD and inside of that the three detectors used in the D^{*+} -meson reconstruction, namely: a Time-Of Flight detector (TOF), and closer to the beampipe the Time-Projection Chamber (TPC) and in the most inner section the Inner Tracking System (ITS) of ALICE. The EMCal is mainly used to detect photons, π^0 and electron with very high transverse momenta [61]. The PHoton Spectrometer PHOS is a higher granularity detector and offers a more precise measurement of photons and π^0 's but has a lot smaller acceptance than EMCAL. PHOS is optimised for measurement of photons, π^0 and η 's with energies from as low as $0.5/1/2 \text{ GeV}/c$, depending on the species, while the EMCal focusses on particles with more than $10 \text{ GeV}/c$ [62]. The TRD or Transition Radiation Detector can perform charged particle tracking and contributes to the electron measurements [63].

3.2.2 V0

The main goals of the VZERO or V0 detector are to act as trigger, to measure the luminosity of the beams and the centrality of a collision.

As shown in figure 3.3, the VZERO is located on the edges of the central barrel. It consists of two arrays of scintillator counters with the V0C on the side of the muon arm, the right side of the figure at a pseudorapidity of $3.7 < \eta < 1.7$ and the V0A on the left side of the figure at a pseudorapidity of $2.8 < \eta < 5.1$. Both the V0A and the



ALICE-PUB-89913

Figure 3.3: Schematic of the location of V0A and V0C, figure from [64].

V0C consist of a disc and each disc is segmented into 4 rings, these rings are each divided into 8 azimuthal sectors. Each of these segments is connected to a PMT of which the timing and charge information is converted via TDC and ADC converters. On the lowest level two types of trigger algorithms are implemented. The primary algorithm is used to select minimum bias events based on timing information of the beams in coincidence with the time signals of the counters. Depending on the timing difference events are categorised in beam-beam and beam-gas interaction from both sides of the interaction point. The second algorithm is used for Pb–Pb (or p–Pb) collisions and is based on the total charge and/or total number of fired sections. As central collisions produce many more particles, this allows a selection of central (0–10%) or Central-Semi Central (0–50%) events. Minimum bias events are recorded if at least one PMT fires in each disc, which selects 84% of the proton-proton collisions.

Luminosity measurements are done via the van der Meer scan method, this meas-

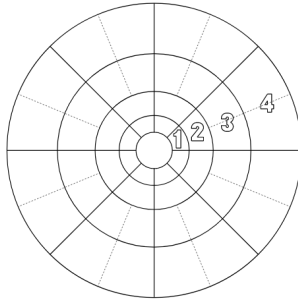
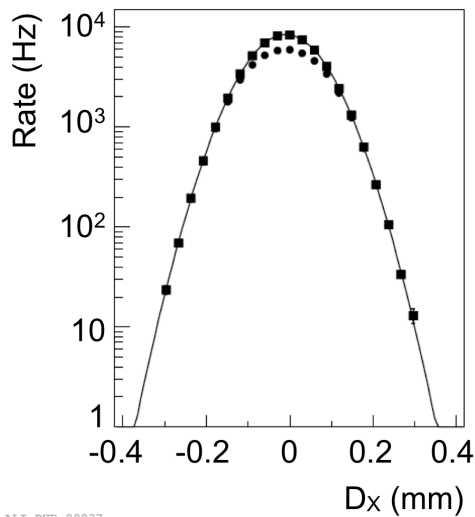


Figure 3.4: Schematic of the segmentation of the V0A and V0C, figure from [65].

measures the size and the shape of the beams by observing the counting rate, giving both the luminosity and the counting rate as functions of the transverse displacements of the beams [[64]-[66]].

The luminosity is extracted based upon the beam specifications, such as intensity



ALI-PUB-89937

Figure 3.5: Example of MB_{AND} counting rate as function of beam displacement in horizontal direction, van der Meer scan data from may 2010, at $\sqrt{s} = 7$ TeV pp collisions. Circles represent the raw trigger data, squares the interaction rate. Figure from [64].

and number of collisions in combination with the counting rate of the V0. The minimum bias cross-section is calculated by correcting the measured collisions with a hit in either V0A or V0C for acceptance and efficiency of the detector.

Depending on the number of produced particles in the collision a higher charge in the V0 is expected. A detailed simulation allows one to extract a centrality or multiplicity distribution based upon the charge distribution found from the V0, via a Glauber model [67] prediction matching the V0 amplitude to the centrality of a

collision.

Centrality determination

The impact parameter b cannot be directly measured. Therefore results of Pb–Pb events are reported with respect to the centrality of the collision. For the most central events the 0-5% percent centrality class is defined, these are mostly head-on collisions with a very small impact parameter. This definition denotes percentages of the total inelastic cross-section that are included up to this percent, meaning that 100% includes all collisions even those in which the particles barely hit each other, so in which b is nearly equal to the radius of the nucleus.

The edge values of centrality classes are identified [68] in the measurement by comparing the charged particle multiplicity distribution to the corrected total number of observed events. These results are corrected for trigger efficiency and defined as

$$c \approx \frac{1}{N_{tot-events}} \int_{N_{ch}^{th}}^{\infty} \frac{dN_{tot-events}}{dN_{ch}} dN_{ch}. \quad (3.1)$$

The impact parameter, and number of participants and spectators can be extracted from this using a MC- Glauber model [69],[67] fit. This model assumes N_{ch} , the number of charged particles in a collision, to be linearly dependent on the number of participant nucleons and the number of binary collisions. This is then convoluted with a negative binomial distribution.

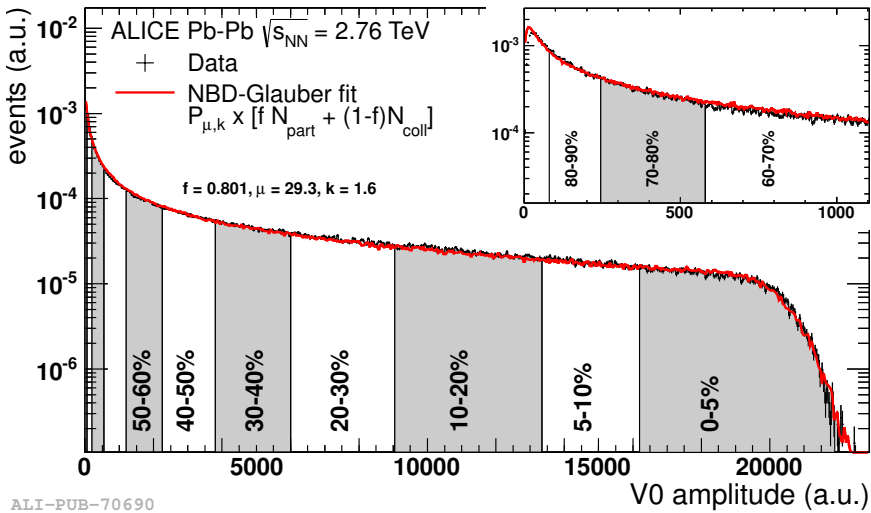


Figure 3.6: Distribution of the V0 amplitude (sum of V0A and V0C) in arbitrary units with respect to the number of events. The centrality bins are defined with respect to the full integral, i.e. with respect to the total cross-section. The absolute scale is determined via a fit to the MC-Glauber model. The inset shows a magnified version of the most peripheral region.

Figure 3.6 shows an example of how the centrality classes are defined based upon a Glauber fit of the distribution of the signal amplitude in the V0. This am-

plitude is a measurement on the relative number of charged particles in the event which can be linked to centrality.

3.2.3 Inner Tracking System

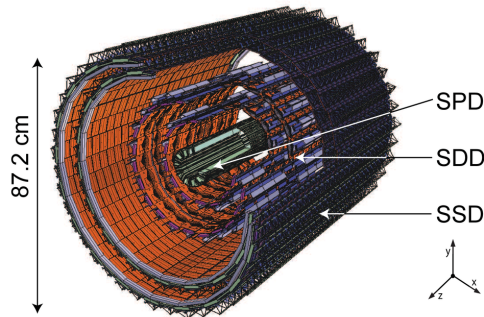


Figure 3.7: Layout of the ITS with directions and layers indicated. Figure from [70]

The Inner Tracking System, or ITS, currently consists of three sets of two layers, from the inside out, the Silicon Pixel Detector (SPD), the Silicon Drift Detector (SDD) and the Silicon Strip Detector (SSD) as shown in figure 3.7. The combination of different layers was chosen to be both cost effective and allow a low material budget. The effective granularity is highest for the innermost layers. Table 3.1 gives the main characteristics and range listed per layer.

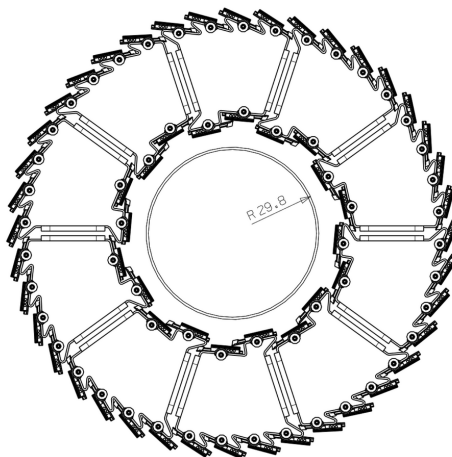


Figure 3.8: Schematic of the SPD and the beampipe. Figure from [70]

The SPD is the most central detector of ALICE and consists of hybrid silicon pixel detectors, which are combined in modules of 256×160 cells. Each cell is $50 \mu\text{m}$ by $425 \mu\text{m}$ in $r\phi$ and z direction. The modules are paired into half-staves in the z direction and combined head-to-head with a mirrored half stave onto a carbon-fibre support which includes the cooling. There is 2% overlap in the $r\phi$ direction between the modules of different half-staves, as shown in figure 3.8, and a small gap in the z direction between two half-staves.

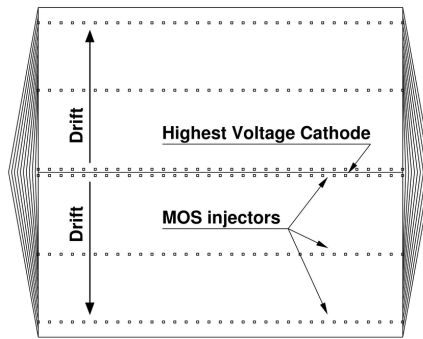


Figure 3.9: Schematic an SDD module. Figure from [70]

The SDD drift detectors around it consist of a silicon wafer on which an electric field is applied to make any free electrons drift. For each module the position of the channel gives the direction perpendicular to the module while the spatial direction inside the module can be extracted from the drift-time of the electron by applying a field in both directions 3.9. Each module is mounted on a linear support structure. Instead of the angled, roof-tile like overlap of the SPD, these straight structures overlap considerably, more than $580 \mu\text{m}$ with each other in $r\phi$ and z direction. Finally the SSD consists of double sided silicon strip detectors, which are almost parallel to the beam axis to provide the best resolution in the $r\phi$ direction. Each module has 786 strips included and the modules are assembled on the same type of horizontal ladders as the SDD, with an overlap of about 2% in both directions [70].

The SDD and SSD detectors offer a measurement of both the spatial position and the deposited energy of charged tracks in the detector while the SPD mainly measures space points. The measurements of the deposited energy can be used for particle identification.

For the ITS the internal alignment is started on cosmic muon data, and is later refined using collision events as well as dedicated runs without a magnetic field [71].

Layer	r[cm]	$ \eta $	$\sigma_{r\phi}$ [μm]	σ_z [μm]	$\%X/X_0$
SPD in	4.0	1.98	12	100	1.14
SPD out	7.2	1.4	12	100	1.14
SDD in	15.0	0.9	38	28	1.13
SDD out	23.9	0.9	38	28	1.26
SSD in	38.5	0.9	29	830	0.83
SSD out	43.6	0.9	20	830	0.86

Table 3.1: Main characteristics of the Inner Tracking System per layer from [70]

3.2.4 Time Projection Chamber

Around the Inner Tracking System, the Time Projection Chamber (TPC) is located. This gas chamber is the main tracking system of ALICE, allowing also a precise particle identification with up to 160 space-time points over the full range.

The TPC consists of a cylinder of 90m^3 with a central electrode in the middle separating it into two drift regions. The electric field is opposite in direction in each drift regions and is kept uniform along the z-axis by a field cage. This cylinder is filled with a gas mixture of Neon and CO_2 (90:10), which will be ionised if charged particles pass through it. The electrons freed in the ionisation will drift towards the end plates where a Multi Wire Proportional Chamber collects their signal. The analogue signal from the Multi Wire Proportional Chamber is proportional to the deposited energy of the particle inside the TPC in that region, which can be used to identify the particles. The drift time of the detector, which is limiting ALICE's data taking speed, is maximally $90\ \mu\text{s}$, which allows an acquisition rate of 11 kHz. At low to intermediate transverse momenta, there is a clear separation in specific energy loss dE/dx compared to the momentum of the particle between different particle species, see fig 3.10. This specific energy loss can be described with respect to the particles momentum via a Bethe-Bloch parametrisation [72].

A spectrum of energy loss for fixed particle momentum can be fitted using a combi-

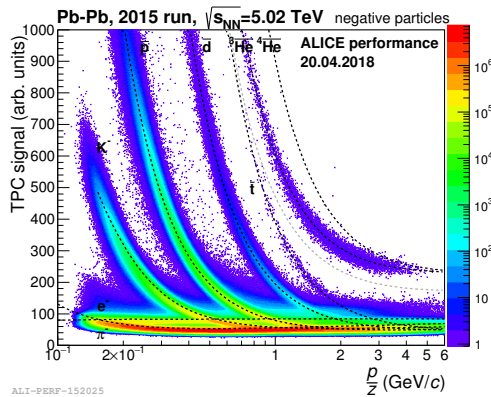


Figure 3.10: Energy loss distribution of negatively charged particles in the TPC in Pb-Pb collisions at 5.02 TeV.

nation of multiple Gaussians for the different available particle species and a background function. The expected mean for each Gaussian can be used as a starting value for the fits. Fig. 3.11 shows the energy loss relative to the fitted mean value, normalised to the width of the distribution, as expected for pions, as a function of the particle momentum. This normalised, relative energy loss is called number of sigma. The distribution of the number of sigma is again fitted with a gaussian. If there would only be pions present within 5 sigma of the gaussian peak the mean of this distribution would be exactly 0 and the width would be equal to 1. If other particles are contaminating this region, the refit will differ in both width and mean. As figure 3.11 shows on average the measured identification for pions is precise enough to have a low percentage of misidentification of pions via the TPC.

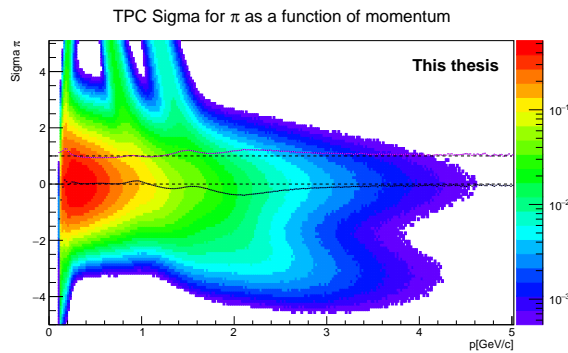


Figure 3.11: Number of Sigma distribution with respect to expectations for charged pions in the TPC in p-p collisions at 13 TeV. The black line denotes the mean from the secondary fit to the distribution, the pink line denotes the width of the secondary fit.

3.2.5 Time of Flight detector

The Time of Flight Detector (TOF) is the final particle identification detector for the intermediate transverse momentum particles. It has a cylindrical shape and is consisting of Multigap Resistive Plate Chamber Strips which are positioned at 370-399 cm from the beam axis. Each strip consists of stacks of resistive glass plates with a high voltage on the external surfaces of the stack (see figure 3.12). The detector covers the pseudorapidity range $|\eta| < 0.9$.

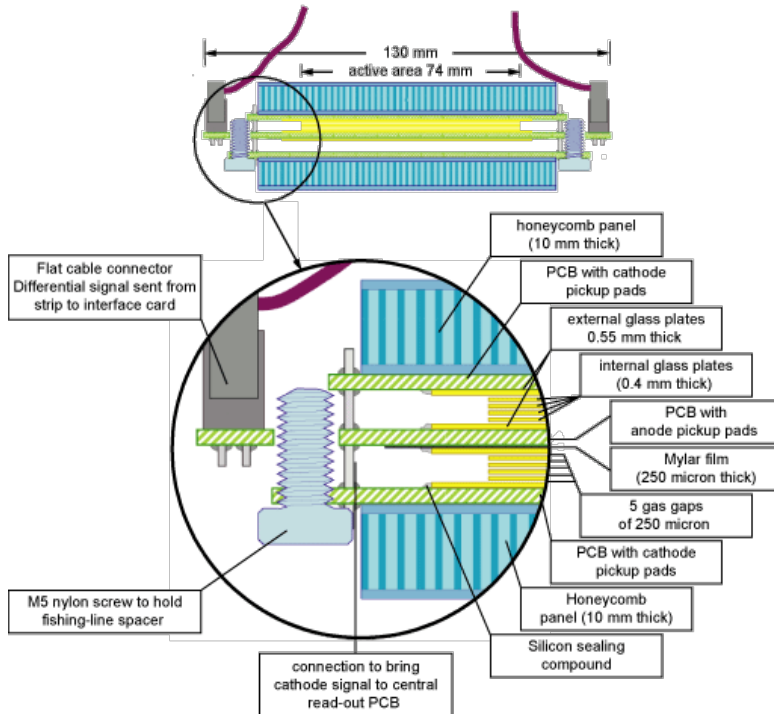


Figure 3.12: Module description of the Time of Flight detector, showing the different material in each module. Figure from http://aliceinfo.cern.ch/Public/en/Chapter2/Chap2_TOF.html

The gas in between the glass plates is ionised by traversing charged particles and the glass plates allows for the ionisation per gap to be measured on pick up electrodes on the ends of each module. Between the internal plates there is a small distance which allows for a good time resolution of the detector of 80 ps for pions with a momentum around 1 GeV/c.

The particle identification uses the time of flight of a particle together with its momentum, which allows the mass to be estimated. The TOF gives a precise time measurement of the moment when a particle reaches the detector, and the time-of-flight is calculated with respect to the interaction time provided by the T0 detector. A 3 sigma separation between kaons and pions can be obtained up to approximately 2.5 GeV/c, and it extends up to approximately 4 GeV/c for kaons and protons [73].

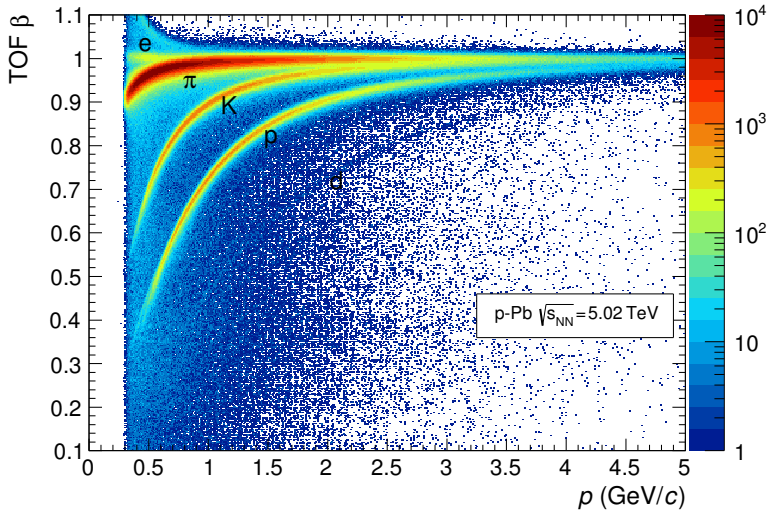


Figure 3.13: Velocity of particle species as measured by TOF as a function of the momentum of a particle measured with the TPC. Measured in p–Pb collisions at 5.02 TeV in run 1, figure from [71]

In figure 3.13 we show the measurement of velocity of different particle species as a function of the charged particle momentum with the TOF in p–Pb collision [71].

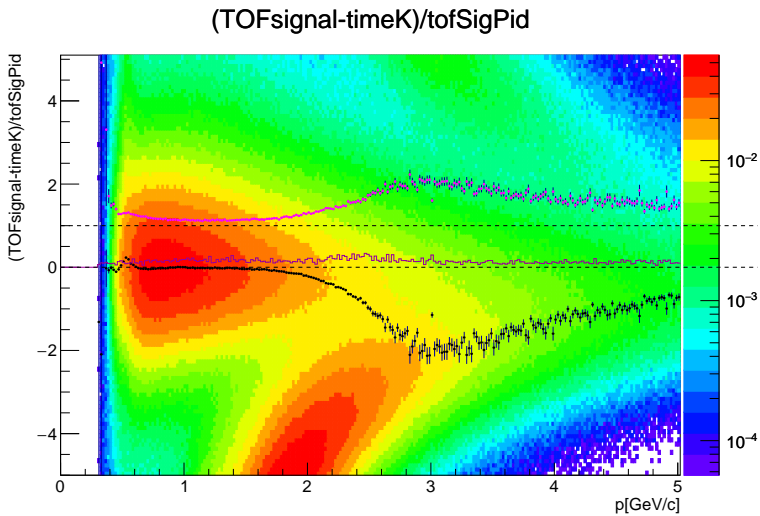


Figure 3.14: nSigma distribution of the measured TOF-times, with included in black the mean, in pink the sigma and in magenta the reduced χ^2 of a fit of the slices with a gaussian. Figure obtained via measurements of p–p collisions at 13 TeV.

In Figure 3.14 a similar figure for the TOF is shown as was shown for the TPC in

figure 3.11. This shows the difference between the expectation and the measured time normalised to the sigma of the original fit.

In the final analysis a background and multiple Gaussians are included for higher momenta particles in the original fit to account for different particle species.

The higher occupancy at nearly 5 sigma consists of pions which come relatively close to the true Kaon distribution. By combining both particle identification methods from TOF and TPC the chances of misidentifications are lowered further.

3.2.6 Tracks and vertex determination

The ALICE tracking information is a combination of the information of multiple detectors, mainly the TPC and the ITS. If there is tracking information available from the TOF or Emcal for instance this information is included, but this will not be the case for those particle we are most interested in for the D-meson analyses.

The reconstruction of a track, the trajectory of a charged particle, is done by matching a combination of clusters into the most likely path of a particle.

The TPC clusters on the outer edge are used as a starting point, and the first possible path is calculated by extending the hit towards the main vertex position, via a Kalman filter algorithm [74]. At each step it searches for a matching cluster on a layer closer to the center. The uncertainties of the previous step are used as weights to choose a region to identify the most likely matching cluster. Once the most inner layer is reached the procedure is repeated in the opposite direction. All matches that are no longer a good fit are replaced moving outwards from the central point, however this process does not stop at the edge of the TPC but checks if information of the TOF/ EMCal or HMPID is available and if so continues. Before repeating the process in the inward direction one last time, the PID information is included in the track. This last inward procedure is called the refit and is done to correct the information in the inner layers, allowing for possible secondary vertex reconstruction.

For the primary vertex determination only the SPD is used, the z-distribution of the hits in the inner layer are checked. If this distribution is symmetric the primary vertex is very close to $z = 0$, if it is not both layers are used and the correlation between their centres can be used to determine the location of the primary vertex. In the transverse direction of the detector most particles will be at sufficiently high momenta to be considered linear inside the SPD. This allows the extraction of the x and y location of the primary vertex via a minimalisation procedure. Different primary vertex x and y positions are a tried and in each case the measured hits in the two layers are connected to make tracks in such a way that as many tracks as possible point towards the proposed location. Extending the tracks creates a distribution of starting points for those tracks, and the distribution of the starting points of all hits is studied. The case in which these starting points have the lowest width for both the x and y direction points towards the correct x and y location of the primary vertex

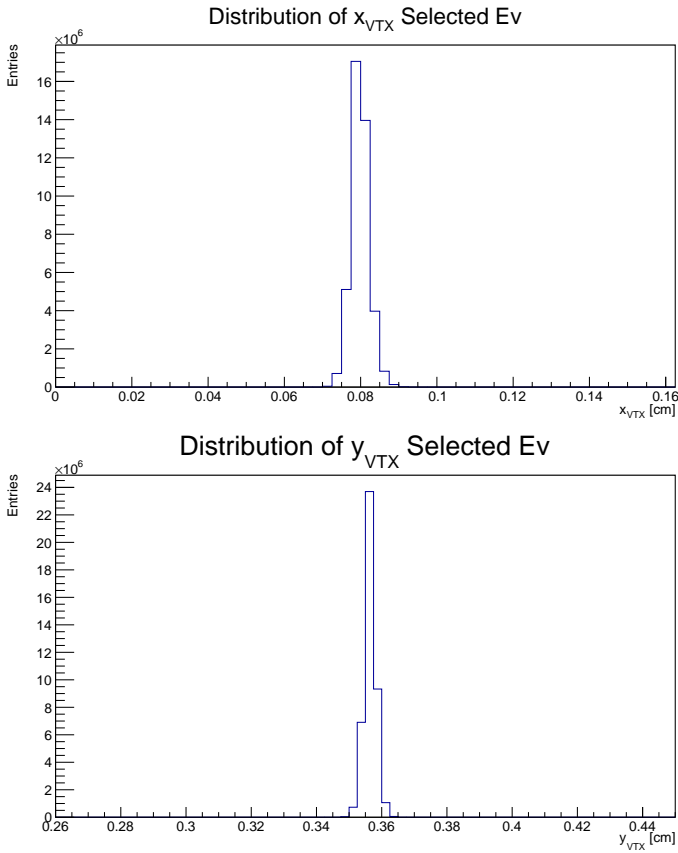


Figure 3.15: Example of x (upper) and y (lower) vertex position of selected events in p–Pb collisions at 5.02 TeV centre of mass energies.

3.2.7 Alice analysis framework

The Alice analysis framework consists of an Object Oriented ROOT-based framework, which is mainly written in C++. This framework, that is maintained by the collaboration via the use of a github system, can be split into two main structures: AliROOT, which contains the data reconstruction and simulation tools as well as an ALICE specific library, and AliPhysics which is more analysis oriented, and of which the packages are maintained per working group of analysers.

The analysis framework uses the CERN computing GRID facilities via the ALIEN handler (ALICE ENviroment handler), allowing acces to a vast international computer network and allowing to handle the large datasamples used in the analyses.

D-meson analysis strategy

The reconstruction of the D^{*+} -meson follows multiple selection steps, both at the event level and at the reconstruction level. The event selection optimizes the balance between statistics and detector performance (4.1). The reconstruction algorithm, on the other hand, is selected to optimize the signal to background ratio (4.2). After the reconstruction a raw yield of D^{*+} -mesons is calculated, this yield has to be corrected with respect to the detector acceptance and the efficiency of the reconstruction. These corrections are based on a good understanding and extensive simulations (4.3) of our detector. A further correction is applied to correct for D^{*+} -mesons that are produced in B-meson decays instead of in the hadronisation of charm quarks, that are directly produced in the hard-scattering (4.4). Finally the calculation of the systematic uncertainties on the $D^{*+} p_T$ -differential cross-section are discussed in section 4.6.

4.1 Event selection strategy

A basic event selection is applied to select reconstructed events in which no vital detector information is missing. The final cross-section is normalised with respect to the number of events after selection, and corrected with respect to the inelastic cross-section measured in the van der Meer scan [75].

The primary selection is done during data taking via a trigger. For both reported analyses this was done using a minimum biased trigger which required coincident signal in both scintillator arrays of the V0 detector (see section 3.2.2).

This trigger was sensitive to approximately 96.4% of the p–Pb inelastic cross-section and an integrated luminosity L_{int} of $292 \pm 11 \mu\text{b}^{-1}$ was collected. For the pp collisions at 13 TeV, see chapter 5, a L_{int} of $3.3 \pm 0.3 \text{ nb}^{-1}$ was reported.

Furthermore, events are selected based upon the available detectors, for this analysis the TPC as well as ITS (SPD, and either SDD or SSD) are required to be included. The particle identification can be done based upon TOF and TPC information, but it is also possible to do the identification purely on TPC information. Thus the TOF detector is not required in order to include a run in the sample used for the analyses. A further selection is required to exclude events for which the D^{*+} decay products are less likely to be reconstructed within the central barrel detectors. For this reason the reconstructed primary vertex is required to be within 10 centimetres of the centre of ALICE in the z direction.

Finally in those cases in which multiple primary collisions are included in one event, i.e. for pileup, the event is rejected. Pileup occurs both via multiple collisions from the same bunch crossing (in-bunch pileup) or via interactions from different bunch crossings (out-of-bunch pileup) which are measured simultaneously. Pile-up has to be rejected as it leads to an increased background due to combinations of tracks from different collisions. The probability of pileup is below 0.5% and it was rejected via a multivertexer approach. In this approach the true primary vertex is identified as the one where the majority of tracks is coming from, taking into account information from both the ITS and TPC if available. If, in addition, there is Time-of-Flight information available, the same bunch crossing id is required, i.e. the difference between a particle's time of arrival and the one expected for such a particle coming from the primary vertex has to be below 25 nano seconds.

Other vertices are removed if they fulfil the following requirements:

- ◆ ≥ 5 particles contributing to the vertex,
- ◆ for all contributors the fit of the track towards the vertex has a $\chi_{\text{red}}^2 < 5$
- ◆ the weighted distance between the primary vertex and this vertex in the z direction, $\frac{Z_{v_{\text{prim}}} - Z_{v_2}}{\sqrt{\sigma_{Z_{v_{\text{prim}}}^2} + \sigma_{Z_{v_2}}^2}} \geq 15$.

The first requirement is used to protect against misidentifying possible secondary vertices (such as a D^0 decay) as pileup vertex. The second is used to not accidentally identify debris from primary or secondary vertices or even random combinatorial as pileup vertex. Finally the distance in z is required to be large enough to exclude the possibility of accidentally identifying part of the main primary vertex as a different vertex. These requirements are used in both analysis reported in this thesis.

4.2 Reconstruction strategy of the D^{*+} -mesons

For the measurement of the p_T -differential cross-section of D^{*+} -mesons hadronised from c-quarks created in the initial scattering, i.e. primary D^{*+} -mesons the selection criteria are optimized with respect to the significance and signal/background ratio of the signal 4.2.1, for the chosen decay channel. Subsequently the D^{*+} yield is extracted via an invariant mass analysis 4.2.2. D^{*+} -mesons and their charge conjugates are reconstructed in the hadronic decay channel of $D^{*+} \rightarrow D^0 \pi^+ \rightarrow K^- \pi^+ \pi^+$ (BRs of $(67.7 \pm 0.5)\%$ and $(3.89 \pm 0.04)\%$ respectively) [76] In the first decay, the

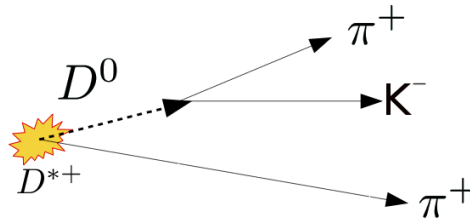


Figure 4.1: Visualisation of D^{*+} decay

decay pion is a so-called soft pion, referring to the fact that it has the lowest momentum compared to the other final state particles.

4.2.1 Selection criteria

Based on the decay topology of the D^{*+} and the detector resolution, a set of variables is identified for which the decay products of true D^{*+} mesons are expected to respond differently than random combinatorial background particles. These variables exploit the topology of the D^{*+} - and D^0 -meson decays and in particular the displaced vertex of the D^0 decay. Before these topological selections are applied tracks are pre-selected based upon the expected quality for tracks created by the decay products of D^{*+} -mesons.

In the analysis frame-work a pre-selection is applied at time of the reconstruction to reduce the computing time for the analysis, this pre-selection is done based on very loose requirements on the same variables as the analysis selection.

In addition to the track selection and the selection based up on the topology criteria, the particle identification information is also used for the reconstruction, leading to four groups of selection criteria:

- ◆ track based criteria for those tracks coming from the D^0 ,
- ◆ track based criteria on the soft pion,
- ◆ decay topology criteria and

- ◆ particle identification criteria.

Track based criteria: $D^0 \rightarrow K^- \pi^+$

For each of the two tracks used to reconstruct the D^0 decaying from the D^{*+} , we require at least:

- ◆ a correct refit in the ITS,
- ◆ at least 2 hits in the ITS of which one in either of the SPD layers,
- ◆ at least 70 out of 159 associated space points in the TPC,
- ◆ $\chi_{red}^2 < 2$ for the reconstructed track inside the TPC¹,
- ◆ $|\eta| < 0.8$,
- ◆ and $p_T > 0.3 \text{ GeV}/c$.

Track based criteria soft pion

Due to the lower momentum of the pion coming directly from the decay from $D^{*+} \rightarrow D^0 \pi^+$, no requirements are made on the TPC information for the soft pion, as it might not reach the TPC.

Thus only ITS requirements are made, being:

- ◆ a correct refit in the ITS,
- ◆ at least 2 hits in the ITS of which one of these two has to be in one of the SPD layers.

Any further selection of D^{*+} soft pion candidates is done based upon the decay topology and discussed in the next section.

Decay topology criteria

The D^{*+} is a very short-lived particle with a decay length $c\tau$ in the order of $0.1 \mu\text{m}$, as it is a strong decay, thus topological cuts are mostly focused on the decay products of the D^0 , which has a mean proper decay length of $\sim 123 \mu\text{m}$.

The main variables used to select D^{*+} mesons from both pp and p–Pb collisions are:

- ◆ The product of impact parameter $d_0^\pi \times d_0^K$ of the D^0 decay products, see figure 4.2
- ◆ the cosine of the pointing angle, which is the angle between the D^0 flight line it would have if it would have been a primarily produced D^0 and the direction of the reconstructed D^0 momentum
- ◆ the distance of closest approach between the D^0 decay products (DCA),
- ◆ for low p_T D^{*+} mesons the normalised decay length.

¹ χ_{red}^2 stands for the χ^2 divided by the number of degrees of freedom for the fit

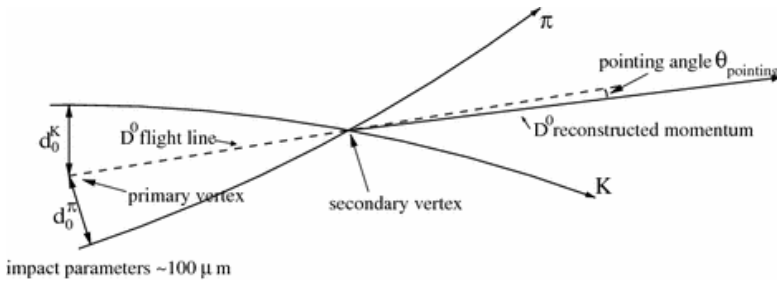


Figure 4.2: Visualisation of D^0 decay with topological criteria.

The normalised decay length is the full decay length including the D^0 decay, i.e. the distance between the primary vertex and the D^0 decay vertex in the transverse plane, divided by the uncertainty on this measurement.

In addition the less stringent selection criteria consist of:

- ◆ a lower bound on the transverse momentum for the kaon and pion originating from the D^0 ($p_{T,K}$, $p_{T,\pi}$),
- ◆ a lower bound on the impact parameter with respect to the primary vertex for the D^0 decay products, $|d_0^K|$, $|d_0^\pi|$,
- ◆ an upper and lower bound on the transverse momentum of the soft pion $p_{T,sp}$,
- ◆ an upper bound on the invariant mass-window of the D^0 (maximal difference with respect to the true D^0 mass) ,
- ◆ an upper bound on the difference of the mass with respect to the true D^{*+} mass,
- ◆ an upper bound on the mass difference between the reconstructed D^{*+} and the reconstructed D^0 .

An absolute lower limit on the transverse momenta of the decay products comes from the difference in rest mass between the D^{*+} respectively D^0 and their decay products.

Due to the displaced topology of the D^0 decay, its daughters are expected to have a larger impact parameter than most of the combinatorial background particles.

The product of impact parameters in our detector has an asymmetric distribution favouring those solutions in which the D^0 decay product appear on opposite sides of the primary vertex, resulting in a negative product of impact parameters.

The final two selection criteria are mainly used to lower computing time, they remove candidates that are extremely far away from our peak. These particles have to consist of combinatorial background and are even outside the range of our invariant mass-analysis.

Optimisation of selection criteria

In both analyses highlighted in chapter 5 and 6 the following optimisation of criterias was used. Starting values for the topological selection criteria were derived from previous optimisations that were applied for proton-proton collisions at 7 TeV. For p-Pb the stricter topological cuts from the run 1 analysis were compared to 7 TeV

pp cuts and a starting value was selected based on a first comparison between both criteria.

The product of impact parameters, DCA and cosine of the pointing angle were varied via a multidimensional optimisation code, which allows the user to vary multiple criteria at the same time. This code performs a signal extraction with a chosen range and calculates the Significance defined as:

$$S_{ign} = \frac{S}{\sqrt{N}} \quad (4.1)$$

$$= \frac{S}{\sqrt{S+B}} \quad (4.2)$$

, where S stands for signal, and B for Background. For more details on the invariant mass fits see section 4.2.2.

The optimisation code was run on a part of the data sample, and the values of the variables were only allowed to vary within those ranges where they gave stable results. The ranges were checked for the stability of the cross-section under variation of the criteria up to 20 %. This percentages was applied directly for the product of impact parameters and the DCA, while for the cosine of the pointing angle it was applied on the difference between the used value and the maximum value of 1. At low transverse momentum of the D^{*+} -meson, i.e. $p_T < 4 \text{ GeV}/c$, the combinatorial background increases strongly and very strict cuts are needed to be able to get a good signal/background ratio. For those momenta the balance between a highly significant raw-yield fit and thus a low statistical and systematical uncertainty from the yield-extraction has to be balanced with a slightly larger systematic uncertainty on the detector efficiency that is associated with the very stringent criteria. In addition to the multidimensional code the normalised decay length was varied individually. This criteria was not used in proton-proton collisions at 7 TeV and to verify the stability of this variable the cross-sections extracted with and without these requirements were compare and found to be compatible.

As an example figure 4.3 shows info from the optimisation done for two p_T intervals from a subsample of the 13 TeV proton-proton collisions. The optimisation code uses the following procedure: for each of the three variables a minimal and maximal value are required as input. This range is divided into 6 values between the start and ending point, creating $8^3 = 512$ different selection criteria combinations. The invariant mass distributions resulting from these criteria are fitted with a function for the background and gaussian for the signal². The fit of the invariant mass distribution is considered succesful if the width³ is between 300 and 1000 MeV/c^2 and the $\chi_{red}^2 < 2.5$. If there is a succesful fit the significance of the fit is saved, otherwise it is set to 0. Finally, figures such as figure 4.3 are acquired in the following way: for each square the code checks all 8 options for the variable that is on neither the x or y axes and assigns highest significance available matching that square. As an example: for the top figure the significance of all values of the cosine of the pointing angle are checked per bin. In addition to the figure the code also gives a numerical

²Similarly to the central values, see section 4.2.2.

³As can be seen in section 5.4, the the average width for the D^{*+} peak from MC is between 400 and 900 MeV/c^2 .

output indication the combination which has the highest significance in the chosen ranges.

Special attention should be given to the the minimal and maximal value, as computing time limits the amount of bins per range so wide values risk missing the optima. Likewise small ranges might not include the optimum as well as might require changes smaller than the detector resolution, which implies that the variation is not really testing the systematic uncertainties. After the multi-dimensional optimisation code was done on part of the sample the selection criteria were tested on the full sample, and an extra test was done to see if the significance and signal over background were influenced strongly if one released the optimised criteria slightly. The loosest criteria set for which signal over background and significance were not significantly lower then the optimal were selected to obtain optimal stability. For the p–Pb case the new proton-proton criteria were compared to the requirements used for p–Pb in run 1 and the variables were tested with respect to the difference between these two cutsets. The best performing combination of the the two sets was used as a starting point and the criteria were further optimised in order to acquire the lowest uncertainties.

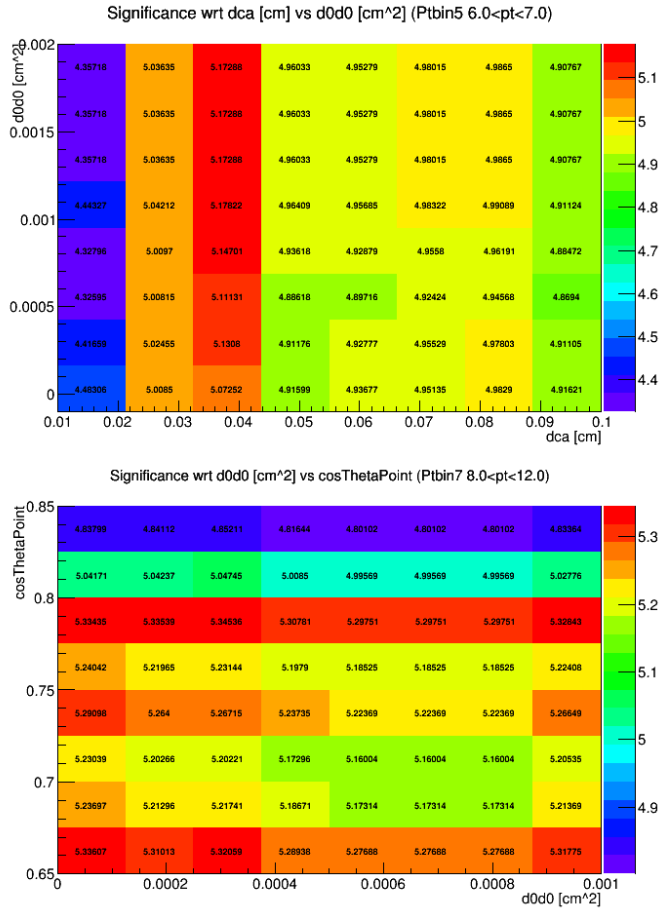


Figure 4.3: Significance of fits with different selection criteria, here the DCA, product of impact parameter and cosine of the pointing angle are varied simultaneously. In the upper figure the found peak significance for D^{*+} -mesons with $6 < p_T < 7 \text{ GeV}/c$ is shown with the product of impact parameters on the y-axis and the DCA on the x-axis. In the lower figure the found peak significance for D^{*+} -mesons with $8 < p_T < 12 \text{ GeV}/c$ is shown with the cosine of the pointing angle on the y-axis and the product of impact parameters on the x-axis. The variation is done on a subsample of the proton-proton measurement at $\sqrt{s} = 13 \text{ TeV}$.

Particle identification criteria

The direct identification of the soft pion does not significantly improve the results and therefore these tracks are selected via the tracking and topological criteria discussed in the previous two sections. Identifying the decay products of the D^0 candidates does give a significant improvement, as they have a higher transverse momentum and both the TPC and TOF information can be used. The method of particle identification for the detectors is explained in subsection 3.2.4 (TPC) and 3.2.5 (TOF). In the analyses reported in this thesis either “normal” or “strict” particle identification requirements were used. There “normal” is defined as agreement with the

requested particle type within 3σ in the TOF and the TPC identification. A “strict” particle identification is defined similarly as agreement with the requested particle type within 3σ in the TOF, but within 2σ for the TPC information.

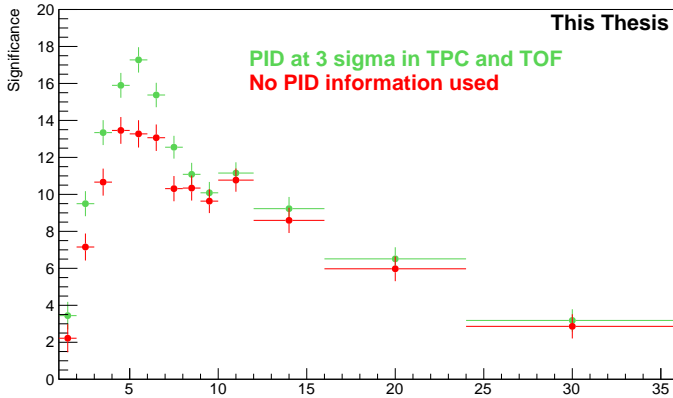


Figure 4.4: Significance of the invariant mass-analysis for D^{*+} in pp collisions at 13 TeV with and without particle identification for the decay products of the D^0 .

4.2.2 Signal extraction

Candidates satisfying all selection criteria are combined in an invariant mass fit. An invariant mass analysis is done on the mass-difference of the reconstructed D^{*+} candidate with respect to that of its reconstructed D^0 candidate to reduce the uncertainty on the measurement and thus the width of the signal.

By taking the difference the widening of the peak due to the resolution effects on the D^0 reconstruction cancel and the width of the peak is mainly due to the resolution of the measurement of the soft pion.

Another effect of this choice is that the absolute lower limit of this mass-difference is equal to the mass of the soft pion. For the upper limit on the mass-difference one has to consider a point reasonably far from the expected D^{*+} meson mass, to allow for determination of the background level.

The transverse momentum intervals of the reconstructed D^{*+} are chosen such that the maximum number of bins is used for which the available statistics leads to a significant measurement.

The left panel of figure 4.5 shows the invariant mass distribution in the transverse momentum interval of 3-3.5 GeV/c of the p-Pb data at $\sqrt{s_{NN}} = 5.02$ TeV as measured by ALICE in run 2, while the right panel shows the same for the transverse momentum interval of 16-24 GeV/c.

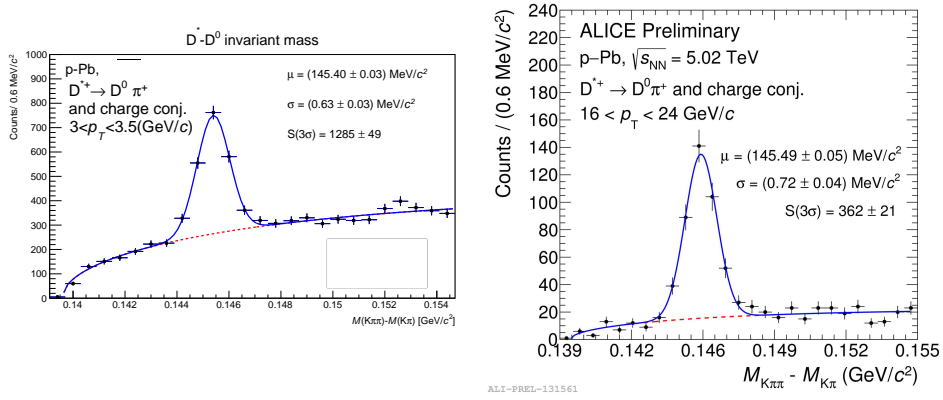


Figure 4.5: Invariant-mass-difference distributions of D^{*+} candidates and charge conjugates in the $3 < p_T < 3.5$ GeV/c interval (left) and the $16 < p_T < 24$ GeV/c interval (right) for a sample of p-Pb collisions at $\sqrt{s_{NN}} = 5.02$ TeV in 2016. The blue curve shows the fit function of a combined signal and background function, while the red dashed line represents the background fit function.

The ΔM distribution of the D^{*+} candidates was fitted with a Gaussian function for the signal, blue lines in figure 4.5, and for the background a square root multiplied by an exponential was used: $a \sqrt{\Delta M - m_{\pi}} \cdot e^{b(\Delta M - m_{\pi})}$, where a and b are free parameters, red dashed line in the figure.

The maximum range is chosen such that the fit is stable and the function fits the background in the range of more than 5σ outside the peak. The signal is extracted by taking the integral of the blue curve within 3σ of the mean of the Gaussian peak and then subtracting the integral of the background function in that range. To understand the systematic uncertainty, alternative fitting ranges, background functions and bin-counting for the signal instead of the integral of the fit are studied in section 4.6.

The reconstruction criteria mentioned in this section are optimized for a combination of the signal/background and significance.

The significance of the signal gives a measure for the size of the signal compared to one standard deviation of the mass-fit. As was defined earlier: $S_{ign} = \frac{S}{\sqrt{N}}$, and as in a counting experiment measuring N particles the natural distribution is expected to be a poissonian distribution thus the standard deviation of such a measurement will be equal to \sqrt{N} .

For discoveries of new particles a significance of 5 is required. As these are measurements of a well-known particle we use all bins where the significance is at least 3, implying that the chance of the measured data point being due to a statistical fluctuation is 1% or less.

4.3 Correction for apparatus effects: Monte Carlo studies

High-energy collisions and also the corresponding measurement processes undergo statistical fluctuations, so a model description is in general studied in Monte Carlo simulations. In these studies random number generators are used to give possible results of such an experiment. These simulations are performed with so-called Monte Carlo generators, whose settings are tuned to describe the collisions under study. For p–Pb the simulated events were produced with Pythia v6.4.21 with the Perugia-2011[77] tune. These simulated physics events then have to be run through a computer simulation of the apparatus, which is performed within the GEANT framework. In these simulations one takes care to implement settings of the experimental setup that match those of the real experiment for each data run.

The heavy flavour working group utilizes a simulated sample in which one $c\bar{c}$ or $b\bar{b}$ is requested in each event and the decays are set to those studied in ALICE.

This forcing of heavy-flavour quarks is done to obtain sufficient statistics for the signal with reasonable computational effort. The downside of this approach is that it will not simultaneously describe the background distributions. A separate simulation sample, without any such bias as introduced by the above requirements, is available to study the background distribution in detail.

As mentioned above the simulated events are matched to a run, share settings with a run, i.e. a contiguous data file. Usually during several such runs in a so-called period the conditions do not change significantly. For each run period, usually including multiple runs, a simulation sample is produced in which the distribution of the simulated sample over the runs is equal to that in data. In each run the detector parameters are set equal to those extracted from data for that run, allowing for run by run comparison of the Monte Carlo and data sample.

This allows to check the matching between data and simulations via quality assurance checks. If the simulation reproduces the data well the testing distributions, such as the number of hits in the ITS, should match between data and Monte Carlo. While these checks are relatively straightforward in the simulation sample that can be used to study the background, it is more complicated in the signal sample. As an example the p_T -distribution of the tracks in data is dominated by the non-heavy flavour background which have a softer p_T distribution than is found in heavy-flavour decay products. Testing the differences at heavy-flavour candidate level do improve these results, however some deviations between the samples are still expected due to a larger non heavy-flavour background in data than in simulations.

The heavy-flavour forced sample is used to determine how efficient our selection criteria are both on D^{*+} -mesons created from prompt charm quarks and on those created in B-meson decays. In addition to the efficiencies of the cuts, the effects of the acceptance of the ALICE detector is also extracted from Monte Carlo simulations. Included in the acceptance correction is the rapidity acceptance of our detector as our measurements are done in a rapidity range of $\Delta y = 2 y_{\text{fid}}$ with the fiducial rapidity range y_{fid} varying from 0.5 at low p_T to 0.8 at high p_T . The final measurements

are reported in $|y_{lab}| < 0.5$. This y_{fid} is defined based on the requirements on the tracks. At low p_T the possibility to measure tracks drops steeply to zero for $|y| > 0.5$. However for $p_T > 5 \text{ GeV}/c$ the track efficiency does not vanish till $|y| > 0.8$. In order to mimic the shape of the distribution y_{fid} it increases from 0.5 to 0.8 in a second order polynomial-shape for $0 < p_T < 5 \text{ GeV}/c$, and then is kept at 0.8 for all higher values. The correction factor for the rapidity acceptance will be denoted as $c_{\Delta y}$.

4.4 Correction for D^{*+} coming from beauty hadron decays

The two dominant production processes for the D^{*+} are production from charm fragmentation (prompt) and decay modes of beauty-hadrons (feed-down). For D^{*+} from charm fragmentation the production can be directly or via decays of other excited open charm and charmonium states.

As we are interested in the effect of possible cold-nuclear matter on the charm quark and the total charm cross-section, it is necessary to correct for D^{*+} -mesons produced in beauty-hadron decays. This is partially done by optimizing the selection criteria to acquire a higher efficiency for prompt D^{*+} -mesons instead of feed-down D^{*+} -mesons. However it is not possible to exclude enough of the feed-down for it to be negligible without excluding too much prompt D^{*+} -meson signal.

Thus the correction factor f_{prompt} is calculated per p_T interval with a FONLL-based method in p-Pb collisions as,

$$f_{\text{prompt}} = 1 - \frac{N_{\text{raw}}^{\text{D feed-down}}}{N^{\text{D+}\bar{\text{D}},\text{raw}}/2} = 1 - A \cdot \left(\frac{d^2\sigma}{dp_T dy} \right)_{\text{feed-down}}^{\text{FONLL}} \cdot R_{\text{pPb}}^{\text{feed-down}} \cdot \frac{(\text{Acc} \times \epsilon)_{\text{feed-down}} \cdot c_{\Delta y} \Delta p_T \cdot \text{BR} \cdot L_{\text{int}}}{N^{\text{D+}\bar{\text{D}},\text{raw}}/2}, \quad (4.3)$$

where A is the mass number of the Pb nucleus.

The B-meson production cross section in pp collisions is estimated with FONLL calculations $\left(\left(\frac{d^2\sigma}{dp_T dy} \right)_{\text{feed-down}}^{\text{FONLL}} \right)$. The efficiency ϵ for D mesons from beauty-hadron decays is extracted from Monte-Carlo studies and combined with the acceptance of the detector (Acc) and the product of these is denoted by $(\text{Acc} \times \epsilon)_{\text{feed-down}}$. Furthermore a hypothesis on the nuclear modification factor $R_{\text{pPb}}^{\text{feed-down}}$ of D mesons from B decays is included, the $R_{\text{pPb}}^{\text{feed-down}}/R_{\text{pPb}}^{\text{prompt}}$ uses a central value of 1 but is varied depending on the centrality class between 1 and 2, this hypothesis introduces an additional uncertainty [78]. Finally, the branching ratio for this decay and the uncorrected yield for the D-mesons are used to calculate the correction factor. The correction factor for proton-proton collisions can be reproduced by setting A and $R_{\text{pPb}}^{\text{feed-down}}$ both to 1 in equation 4.1. While this method offers a precise correction for the cross-section produced in proton-proton and p-Pb collisions it utilizes FONLL predictions on the feed-down to do so. One could argue that the downside of this is that one is using the theoretical predictions for the beauty to correct the measurements on a different

parton where one is trying to falsify the theory based on the same approach. However as the beauty correction is fairly small (less than 10%), this does not influence the results significantly. The cross-section obtained from these collisions is used primarily to test FONLL predictions on the prompt D^{*+} -mesons production cross-section. To eliminate this inconvenient method the ALICE experiment is currently improving methods to measure the prompt-fraction experimentally. The data-driven method exploits the differences in the shape of impact parameter distribution which is more sharply peaked for prompt D -mesons than for feed-down D -mesons. The data-driven method currently acts as check on the reliability of theory method. Due to the limited range and precision the data-driven method introduces a larger uncertainty in the measurement than the use of the theory at this time. As can be seen in figure 4.6 the data-driven method is in agreement with the theoretical approach within uncertainty.

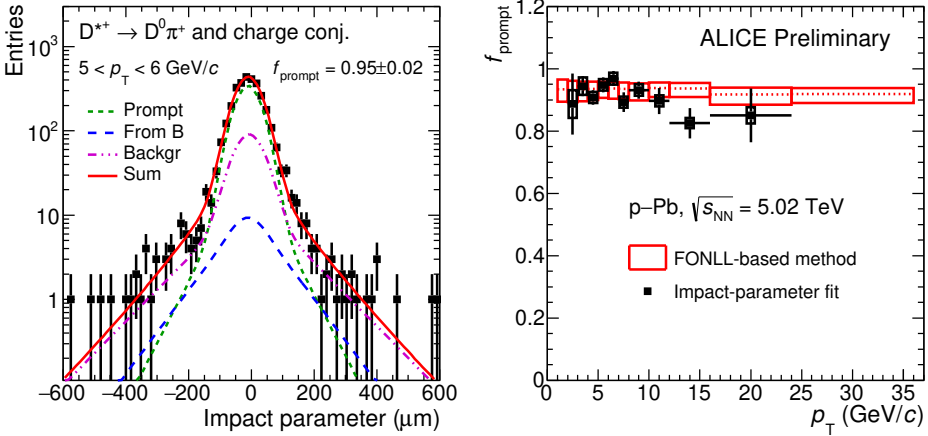


Figure 4.6: Left: Impact parameter distribution for the D^{*+} , with fits for the prompt, feed-down and background contributions. Right: fraction of prompt D^{*+} raw yield as a function of p_T compared to the values obtained with FONLL-based approach. The uncertainty mentioned on the FONLL method is due to the internal uncertainties on the theory mentioned in the previous chapter.

4.5 The $D^{*+} p_T$ -differential cross-section

The final cross section is calculated according to the following equation:

$$\frac{d^2\sigma^{\text{prompt}D^{*+}}}{dp_T dy} = \frac{1}{\Delta p_T} \cdot \frac{f_{\text{prompt}}(p_T) \cdot \frac{1}{2} \cdot N^{\text{D}^{*+} + \overline{\text{D}^{*+}}, \text{raw}}(p_T)}{c_{\Delta y}(p_T)} \cdot \frac{1}{(\text{Acc} \times \epsilon)_{\text{prompt}}(p_T)} \cdot \frac{1}{\text{BR} \cdot L_{\text{int}}} \quad (4.4)$$

Here, $N^{D^{*+}\overline{D}^{*+},\text{raw}}$ represents the raw yield (sum of particles and antiparticles) in the rapidity interval Δy and p_T interval of width Δp_T , measured as discussed in section 4.2.2. This raw yield includes contributions from both prompt D^{*+} -mesons and D^{*+} -mesons created in Beauty decays.

The rapidity acceptance correction factor $c_{\Delta y}$ and the product of the acceptance and the efficiency of prompt D^{*+} mesons $(\text{Acc} \times \epsilon)_{\text{prompt}}$ are extracted via Monte-Carlo simulations as discussed in section 4.3.

The factor 1/2 accounts for the fact that the measured yields include particles and antiparticles while the cross sections are given for particles only.

f_{prompt} is the fraction of prompt D mesons effectively reconstructed in the raw yield, BR the branching ratio of the considered decay channel and L_{int} is the integrated luminosity.

4.6 Systematic uncertainty strategies

In the previous sections of this chapter the reconstruction and invariant mass analysis is broken down into several steps and in many of these steps there are uncertainties involved.

For instance there is no physical reasoning to choose an exact range on which the fit for the background level is performed. One should only require that the background under the signal peak can be well described in this range, see section 4.2.2. By varying parameters that can influence the measurement but are not bound by physics the systematic uncertainties due to the chosen method can be evaluated. The range of the fit influences the uncertainty due to the fitting method, but the possibility that the description of the detector in the simulation is not identical to the actual detector effects introduces an uncertainty on the measurement as well. In this section the uncertainties introduced in the method of calculating the cross-section are discussed, starting from the formula used for the cross-section.

4.6.1 Raw yield systematic uncertainty

For the raw yield the systematic uncertainty is considered the uncertainty due to the fit, i.e. the uncertainty due to the chosen fitting method.

In these analyses, this can be split up into the uncertainty due to the fit function for the background, fit function for the peak, that due to the binning for the mass histogram and that due to the choice of fitting range for the invariant mass. The method to estimate these uncertainties is explained below. For each transverse momentum bin the central value is selected on a minimal value of the reduced χ^2 and it is checked if the result is stable i.e. it is not an outlier of the distribution of values. These central values are compared to other possible values in terms of yield, width and mean peak position. These values are obtained via a large sample of variations. These variations contain:

- ◆ multiple different rebinnings,
 - for instance if in the original measurement the mass-histogram's minimal bins are combined in groups of 6, other possibility varying from combining them in groups of 4 to groups of 8 are allowed,
- ◆ variations of the fit range on both sides of the spectrum,
 - the absolute lower limit of the fit-range is the pion-mass, variations of the lower limit are taken to be starting and this mass or one to 6 measurement points further in the data taking binning, for the upper limit of the fit-range a variation between 5σ and $< 20\sigma$ from the center of the averagely fitted peak is used,
- ◆ A different fit-function for the background is used, a powerlaw of the form $a(\Delta M - m_\pi)^b$, where a and b are free parameters, for this background the rebinning and fit range variations are also
- ◆ the fit function for the peak is checked by performing a bin-counting after using a so called Poissonian smearing of the peak.

The Poissonian smearing is a process in which each data point is understood as being a mean value in which the uncertainty of the measurement is the width of the corresponding poissonian distribution for that point. Via a monte-carlo method this can then be used to create many theoretically possible measurements assuming the original measurement as the mean and true measurement. This was added to check for effects of possible fluctuations on the data points that could influence the bincounting more strongly than the integral. For each of these measurements the background fit is used and the peak is calculated via bin-counting instead of using the integral under the corresponding data peak.

The effect of the types of variations is tested as follows: for each combination of binning variation and lower and upper range of the invariant mass distribution a new fit is done. This process is subsequently repeated with the alternative background hypothesis.

The variations in binning and lower and upper range are done via a multi-fitter code which was developed during this PhD ⁴. For each succesful fit the mean, width and raw yield are saved and result in distributions such as figure 4.7.

A fit is deemed succesful if:

- ◆ the fit has a reasonable reduced $\chi^2 < 3$,
- ◆ the fit has a width that is, within uncertainties, compatible to that expected from Monte Carlo simulations, and
- ◆ a mean peak position that is compatible with the expected mean positions extracted from simulations in which similar selection criteria were applied.

If a fit matches these requirements and has a significance above 3^5 , is taken into account in the extraction of the uncertainties as such a fit would be accepted for a central hypothesis result.

The extracted raw-yield differences are combined with the distributions obtained for the alternative background and the ones from bin-counting variations. These distributions are weighted such that the combination of binning and range variations has a weight of 2 compared to 1 for the alternative background and the bin-counting variations. This specific weighting was chosen to give equal weight to all 4 possible sources and matches old measurement methods⁶. A combined distribution containing all types of trials is extracted and from this distribution the RMS is calculated, which gives a size of the uncertainty on the Raw Yield extraction.

⁴With help of bachelor student Joris Ketelaars.

⁵For cases where the central value is very close to 3 a seperate test is also checked and the requirement can be set to lower values if needed

⁶Multiple tests have showed that the exact weight between the various sources does not influence the results very strongly, similar results were obtained with weights varying from 1 to 4 for the available sources.

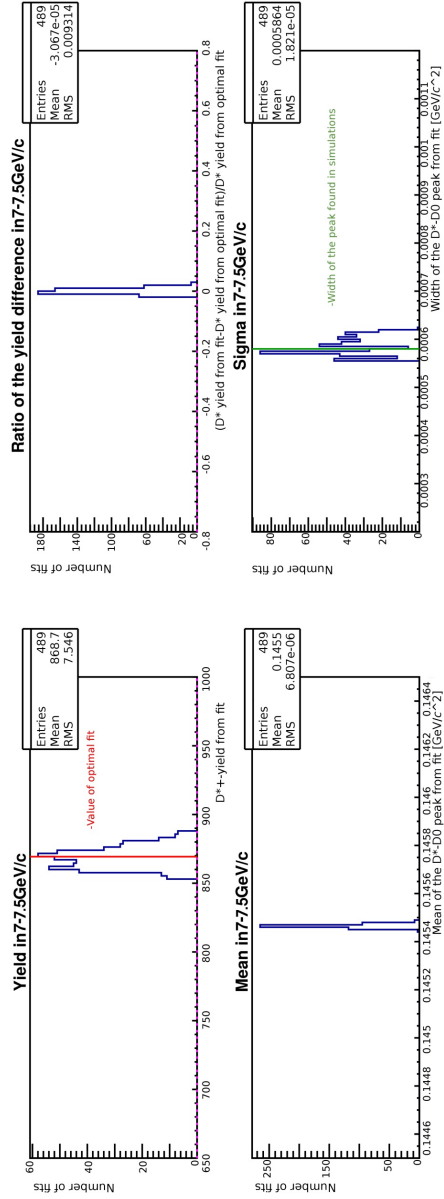


Figure 4-7: Exemplary results of the multifitter: upper two figures show the Raw yield and ratio of Raw-yield difference w.r.t. Raw yield central value. Lower two figures show the mean and width distribution of the fits. The red line shows the central value raw-yield, the green line shows the predicted width of the gaussian in simulations.

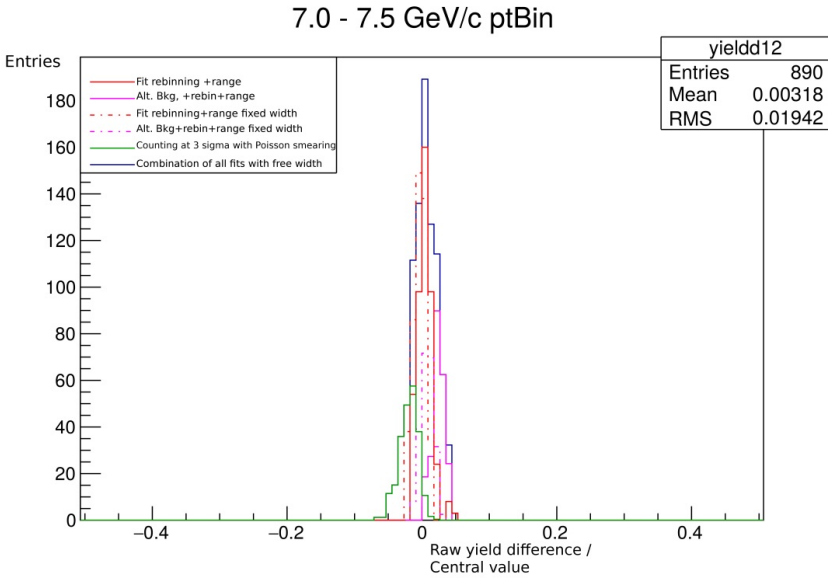


Figure 4.8: Example of the combination of the various sources of uncertainties on the raw yield

For the efficiency and acceptance factor the uncertainties are assumed to consist of multiple independent sources and are therefore calculated and added independently. The uncertainties on the acceptance and efficiencies considered in a typical cross-section analyses are:

1. The uncertainty on the track reconstruction
2. The uncertainties on the selection criteria,
3. The uncertainty on the particle identification,
4. The uncertainty with respect to the weighing of the transverse momentum distribution with respect to either a FONLL shape or the one with which the Monte Carlo is produced.
5. The uncertainty on the feed-down correction.

All of these uncertainties are considered fully independent. They all enter in the total uncertainty via a sum of squared uncertainties $\sigma = \sqrt{\sum_i \sigma_i^2}$.

4.6.2 Tracking Uncertainty

The uncertainty on the reconstruction of tracks has to be split in two types of tracks for the D^{*+} , namely the tracks for the D^0 candidate and the track of the soft pion. This distinction is made due to the different requirements placed on both type of track. For the soft pion tracks the uncertainty is extracted via the following variations

of the requirements:

- ◆ at least 3 instead of at least 2 hits in the ITS,
- ◆ requiring a hit in the first layer of the SPD instead of in any layer,
- ◆ or requiring a hit in both layers of the SPD instead of in one of them.

These requirements are changed separately and the uncertainty is extracted from the distribution of the variations. The low momentum of the soft pion increases the possibility for a incorrect track reconstruction inside the ITS, leading on average to a slightly larger uncertainty.

For the tracks of the D^0 associated with the D^{*+} , the uncertainty on the ITS is insignificant when compared to the requirements on the TPC and the matching uncertainties between both detectors. To extract a systematic with respect to the TPC requirements the following settings are varied:

- ◆ the number of clusters required in the TPC
- ◆ the lower bound on the ratio of the total number of clusters with respect to crossed rows
- ◆ required ratio of crossed rows over findable clusters.

For the matching efficiency the fraction of tracks with clusters in both ITS and TPC with respect to all with clusters in the TPC is studied. However the matching efficiency for secondary tracks is expected to be lower than for primary tracks and tracks arising from interaction with material should have an even lower efficiency.

Thus if the fractions of primary and secondary tracks differ between data and the simulation, the estimation of the systematic uncertainty in the matching would be incorrect. Such a difference could either be due to true differences between the efficiencies in simulations and data, or due to a incorrect weighting of the fractions. Hence, the Monte Carlo efficiencies are reweighted with the fractions obtained from data to obtain a corrected inclusive efficiency. This efficiency is compared to the efficiency without reweighting of the primary and secondary fractions to extract a source of systematic uncertainty. The uncertainty on the matching efficiency as a function of p_T is calculated as:

$$\sigma_{matching} = f_{primaries} \times Eff_{primaries}^{MC} + (1 - f_{primaries}) Eff_{secondaries}^{MC},$$

where the Monte Carlo efficiency is corrected with the fraction of primaries and secondaries extracted from data. This per track uncertainty is then summed in quadrature with the uncertainty coming from systematic on the TPC selection for the D^0 tracks.

Finally, as the ITS-TPC matching efficiencies are measured in final particle p_T intervals the full uncertainties are propagated to D^{*+} -meson p_T intervals. This propagation takes place via Monte Carlo simulation applying the same topological and PID cuts that were used in data, to include the influence of our topological selection on daughters kinematics.

For the D^{*+} the soft pion systematic uncertainties are summed with the D^0 decay products tracking uncertainty. For the tracks corresponding to the D^0 daughter tracks both matching efficiency and the tracks variations uncertainties are included. As there is no matching applied for the soft pion, for these tracks only the track variation uncertainty is included.

4.6.3 Selection Criteria Uncertainties

As mentioned in section 4.2.1 there are 4 main selection criteria which most strongly influence our invariant mass-spectra, the product of impact parameters, the DCA, the cosine of the pointing angle and the normalised decay length. These selection criteria are simultaneously varied, both stricter and looser in order to extract reasonable invariant mass-spectra. The variations must be selected in such a way that one has both differences large enough to possibly yield different results, as well as still be able to extract a stable yield from the spectra. The effect of the variations can be seen by checking the difference in efficiency as this give the size of the expected difference.

However if the criteria used for the central values are very loose, one should not force a large difference in the efficiency. As with loose central cuts a very large difference in values might be needed to create a reasonable difference in efficiency. Imposing such stringent criteria does not test how our simulation behaves in the situation in which we extract our yield. Instead it is testing if our simulation is still valid in those extreme regimes, which should not influence the uncertainty on our measurement. In addition to that, very tight cuts might result in very low yields, which are then very sensitive to statistical uncertainties, which should be avoided if at all possible.

In this dissertation variation up to 20 % of the value of the criterium or even larger for loose criteria have been used. The resulting mass spectra are tested with respect to the fit quality. For the cosine of the pointing angle the difference was expressed in terms of the difference to the maximum possible pointing angle value , so with respect to 1. A further description of the variations with respect to the central value and the selection criterium can be found in the respective chapters.

4.6.4 Particle Identification uncertainties

The uncertainties on the particle identification are acquired by comparing the situation with and without particle identification. However if a more stringent particle identification was applied this was compared to results with the standard 3σ requirement in TPC and TOF as well. The requirement of matching within 3σ in both the TPC and TOF combined have a 95% acceptance ratio in which the associated uncertainties of the ALICE detector are negligible. To check the size of a possible uncertainty the ratio between results with and without particle identification information is studied. If the mean value over the full p_T -interval is significantly different from 1, this is quantified as the uncertainty due to Particle Identification.

4.6.5 Transverse momentum distribution uncertainty

The true transverse momentum distribution of D^{*+} in the data is not precisely known. One can only measure the final decay products distribution and any measurement is influenced by the detector resolution of the detector used in the measurement. Therefore the transverse momentum of the particles in the simulation is weighted with a FONLL-predicted distribution or alternatively the decay products are weighted with a distribution that matches the data set as closely as possible. The difference between the $D^{*+} p_T$ -differential cross section with these different weights

is compared. If the difference between both settings is significant this is added as a systematic uncertainty to the p_T -differential cross-section.

4.6.6 Feed-down correction uncertainty

The systematic uncertainty on the theoretical part of the subtraction of feed-down from B decays was estimated via a variation of the FONLL parameters (b-quark mass, factorisation and renormalisation scales and uncertainty associated with Parton Density functions) [45]. For the central hypothesis the factorisation and renormalisation scales are set equal to the transverse mass of the b-quark.

The uncertainty is estimated by varying the renormalisation and factorisation scales separately, and taking the envelop of these variations. For the mass values, three mass-values are used for the b-quark mass, namely $m = 4.75, 4.5$ and 5 GeV.

The Parton Density Function's internal uncertainty is calculated inside the associated theoretical framework, in this case CTEQ6.6 [79] and included as an independent source of uncertainty. These three uncertainties are added in quadrature and used to calculate the feed-down uncertainty due to correction in proton-proton collisions. The experimental uncertainties due to selection criteria and so on are included in the estimations discussed above, thus do not need to enter here again. Therefore it suffices to include only the theoretical uncertainty for pp collisions. For the p-Pb additionally the uncertainty of the hypothesis on the nuclear modification factor of feed-down D mesons has to be included and is extracted by varying this hypothesis in the range $0.9 < R_{pPb}^{\text{feed-down}}/R_{pPb}^{\text{prompt}} < 1.3$.

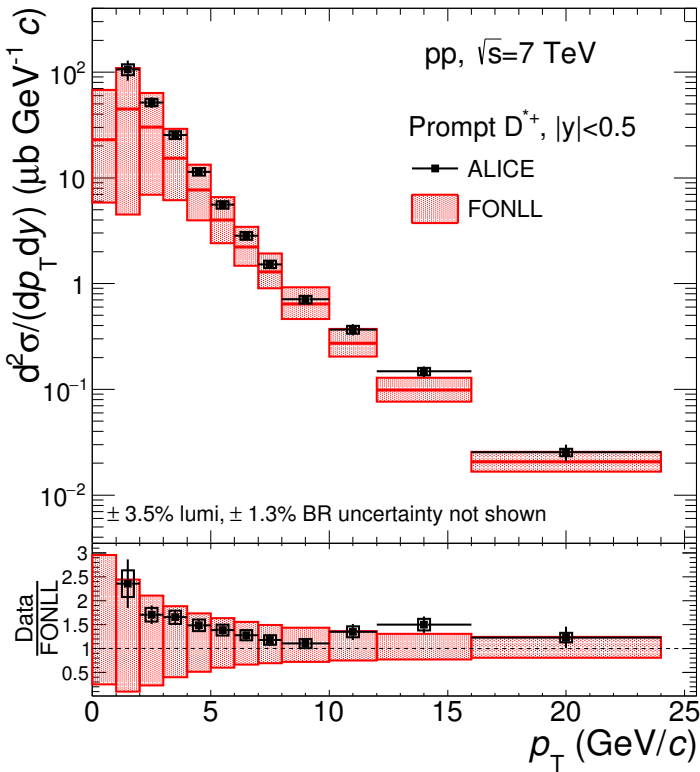
D-mesons in proton-proton collisions

In run 1 of the Large Hadron Collider the ALICE collaboration has measured D-meson invariant cross sections via hadronic decay channels. These measurements were done at all collision energies provided at the LHC, starting from $\sqrt{s} = 2.76$ up to $\sqrt{s} = 7$ TeV . In this chapter we will present our new measurements at $\sqrt{s} = 13$ TeV and as an introduction revisit a few important results at lower energies to motivate our measurement.

5.1 Results in pp collisions at $\sqrt{s}=5.02$ TeV and $\sqrt{s}=7$ TeV

In run 1 of the LHC ALICE has been able to measure proton-proton collisions at 2.76, 7 and 8 TeV centre of mass energies. Proton-proton results are studied for two main goals: to serve as a baseline for lead-lead and proton-lead runs and to test pQCD calculations, as was discussed in section 2.4.

For the 7 TeV results of run 1, the D^{*+} meson measurements are available in a trans-



ALI-PUB-125431

Figure 5.1: p_T -differential production cross sections for prompt D^{*+} mesons compared to FONLL [46] pQCD calculations. The ratios of the data to the theoretical predictions are shown in the lower panel. Figure from [80].

verse momentum range of 1-24 GeV/c, see figure 5.1 from [80].

These results were found to be in agreement within the uncertainties with FONLL[46] calculations, but there was some tension with the theory in the highest transverse momentum bins. In addition the measurements are consistently at the upper 1σ limit of the theoretical predictions. These results, with an integrated luminosity of

$L_{\text{int}} = (6.0 \pm 0.2)nb^{-1}$, i.e. 370 million events, was the largest sample in which D-meson measurements have been done in proton-proton collisions that ALICE has collected in run 1.

In run 2 of the LHC results at $\sqrt{s} = 5.02$ TeV were collected to serve as a more stable and solid baseline for the proton-lead and lead-lead measurements at this same energy. Previously, energy-scaled results derived from the 7 TeV results were used as a baseline. The new pp results were collected at an integrated luminosity of $L_{\text{int}} = (19.3 \pm 0.4)nb^{-1}$, i.e. 990 million events in 2017. This sample has almost triple the statistics of the entire 7 TeV sample. The new sample permits an increase of the transverse momentum range of the measurement and the use of a finer binning in the previously precisely measured transverse momentum range. In figure

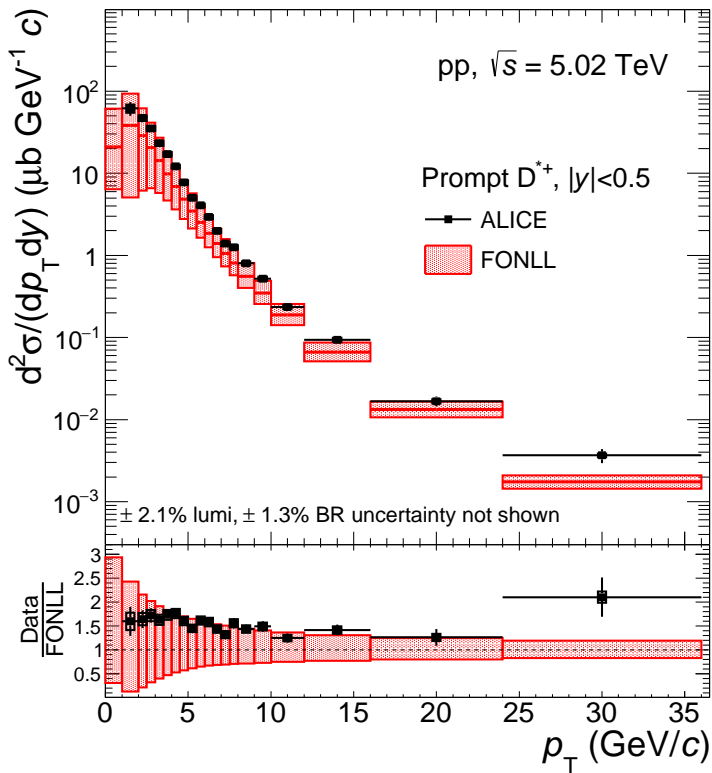


Figure 5.2: p_T -differential production cross sections for prompt D^{*+} mesons are compared to FONLL [46] pQCD calculations. The ratios of the data to the theoretical predictions are shown in the lower part the panel. Figure from [81].

5.2 the $D^{*+} p_T$ -differential cross-section in pp collisions at 5.02 TeV is compared to theoretical prediction of FONLL[46]. These results are at the upper limit of the uncertainty band on the theory, which is consistent with the earlier measurement. Our

new measurements strongly constrain the theoretical predictions as the precision of our measurement is a lot higher than the theoretical uncertainties. The study of the energy dependence of charmed particle spectra in proton-proton collisions can be performed via ratio's between cross-sections. This has the advantage that a number of uncertainties in the corresponding theoretical calculations cancel. Therefore precise measurements of D-mesons cross-sections could allow to test the energy dependence which at low p_T has PDF's which are mainly gluonic of nature, see section 2.4. However, the predicted differences between 5 and 7 TeV is relatively small as the energy difference is not so large. Comparing, instead, the 5 and the 13 TeV results at high precision would therefore be a very interesting measurement[46].

5.2 Data sample at 13 TeV for D-meson analyses

The ALICE experiment has taken data in proton-proton collisions at 13 TeV from 2015 till November 2018. In this thesis the cross-section of the D^{*+} -meson measured in part of the sample collected in 2016 will be discussed. This data set consists of 1.9×10^8 events i.e. a luminosity of $L_{int} = (3.3 \pm 0.2) \text{ nb}^{-1}$. A global quality assurance, used to reject runs in which a detector was misbehaving strongly or remove unstable runs, of this sample was provided by the data processing group. As a further assurance extra checks were performed, in the scope of this thesis, to check for possible issues in the sample. As was mentioned in chapter 4 the D^{*+} reconstruction strategy relies strongly on the ITS, TPC and TOF results. Thus the performances of these detectors are specifically checked.

There are some known area's in which a detector might have imperfections. Some of these imperfections are known, and thus corrected via the simulations, others however might not yet be well known and one will have to include these effects in the systematic uncertainty on the measurement. Possible reasons to not (fully) correct for detector problems can be due to either computing power or the time it would require to implement the solution which are not always worth the size of the possible improvement. For instance small instabilities in the ϕ direction in the ITS due to missing sectors, would have to be corrected precisely for correlation measurements, but can be included inside the acceptance for a cross-section. As long as the measurement does not strongly depend on an imperfection, a corresponding correction would not be worth the associated effort. If any imperfections are not fully described, in places where they do influence the measurement these should be probed in the procedure to address the uncertainties. As small changes in the detector topology have strong influences on the results, the uncertainties due to the topological selection criteria and those due to the track selection criteria are very sensitive to possible missed imperfections in the detector. In order to understand possible sources of disagreement between data and simulation a precise quality assurance which takes into account as many detector or alignments effects as possible is a necessity.

In this dissertation a few examples of the applied quality assurance tests is shown. These tests focus on those area's in which the simulation disagree with the data, which can point to a missed detector imperfection, but some can also be explained by choices made to limit computing time in the simulation process. It is highlighted how this disagreement is understood and if necessary corrected or taken into account in the uncertainties.

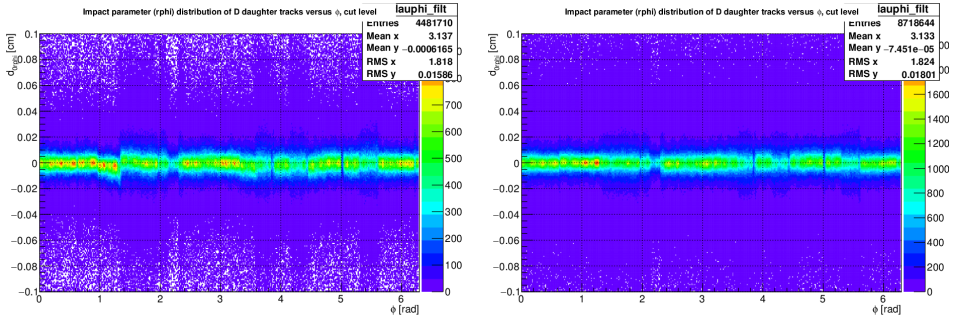


Figure 5.3: Transverse impact parameter of D^0 -daughter tracks as a function of their azimuthal angle, for data (left) and heavy-flavour Monte Carlo (right), after event selection.

As mentioned the ITS is a very important element for the D^{*+} -meson analysis as, amongst others, the measurements of the impact parameters rely heavily on the ITS information. The transverse impact parameter distribution for the daughter particles of D^0 -meson candidates are compared between data and Monte Carlo in figure 5.3. These distributions are used to locate possible areas of misalignment in modules of the ITS as well as a check for the correct implementation of known ITS deficiencies. In figure 5.3 the transverse impact parameter distribution for the daughter particles of D^0 -meson candidates are shown as a function of their azimuthal angle ϕ . This comparison reveals shifts in the data distribution around $\phi = 1.2, 3.5$ and 4.5 radians, which are not reproduced by Monte Carlo simulations. This effect was seen in all of the 2015/2016 data, and is due to residual SPD misalignment not taken into account in the Monte Carlo productions. Part of the parameter resolution and the observed shifts in data have been corrected by a so called ImproverTask. This is a script which shifts the data back to the correct alignment. If any residual effects are not corrected these are included in the systematic uncertainties via the variations of the product of impact parameters. In the simulations a slightly broader distribution of the impact parameter distribution with respect to data is expected, as the simulations studied for the analyses are enriched in terms of charm and beauty quarks, this can be seen in the values of the y-RMS in the above figures. Beauty hadron- and feed-down D-meson decay products have a wider impact parameter distribution than the decay-product originating from prompt c particles or background.

For the soft pion one of the track requirements is that it includes at least one hit in any SPD layer of the detector. This is used to be able to correctly identify such a track and figure 5.4 shows the necessity of such a criterium. On the left we see that without this requirement the agreement between the data (blue) and the simulations (red and green) is rather poor for ITS-standalone tracks. On the right this requirement is added and one can see the strong improvement in the agreement between both. The reason to show two simulations is to identify if this is only necessary for charm/beauty dependent particles (red) or also for non-heavy flavour particles (blue).

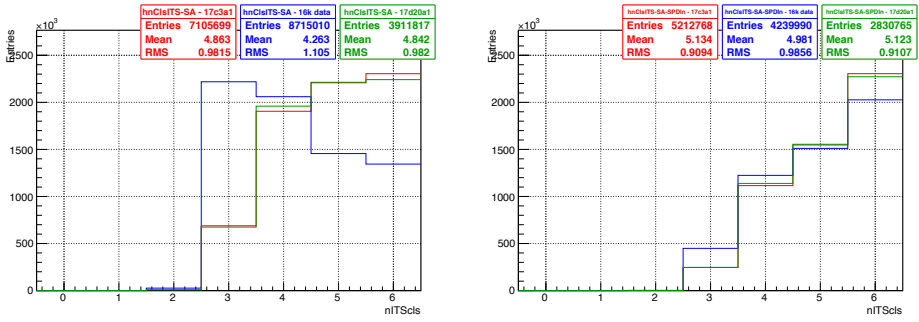


Figure 5.4: Number of ITS clusters involved in the reconstruction of ITS-standalone tracks (without quality criteria), without SPD request (left) and with SPD request (right), for selected events. Distributions obtained in data (blue), general-purpose Monte Carlo (green) and heavy-flavour Monte Carlo with updated dispersion of the luminous region (red).

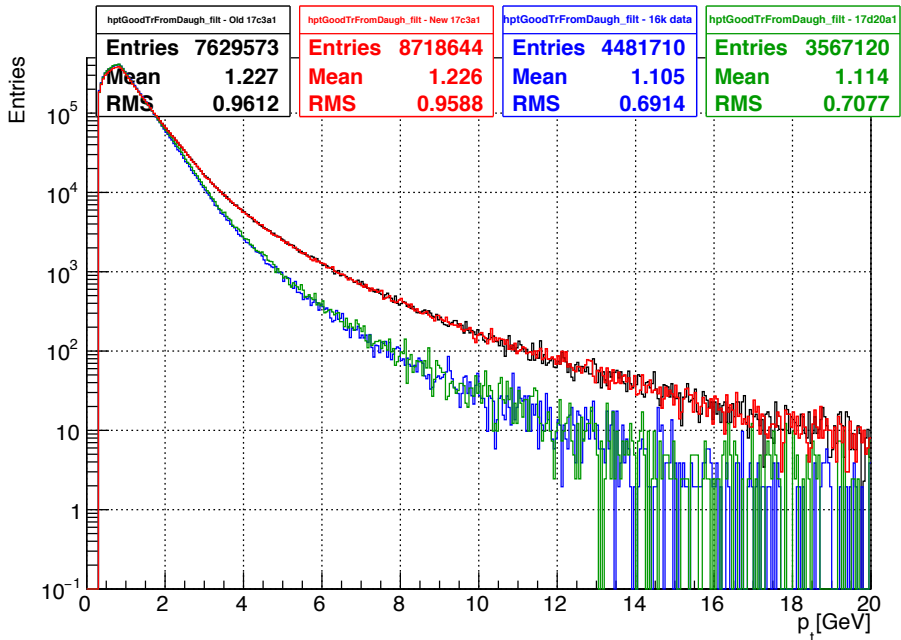


Figure 5.5: Transverse momentum distribution of tracks selected by filtering criteria to be possible D^0 decay product candidates for selected events. Distributions obtained in data (blue), general-purpose Monte Carlo (green) and heavy-flavour Monte Carlo with updated dispersion of the luminous region (red).

Figure 5.5 shows that the p_T -distribution of all tracks selected with non stringent D^0 selection criteria from D^0 decay-product in the heavy-flavour forced Monte Carlo and the data, respectively, is also very different. Using these non-stringent criteria does not select primarily real D^0 candidates in the data, which means that the data sample is primarily filled with pions and kaons that do not come from a D^0 . This becomes clear as the comparison with the general simulation, in which there is no forcing of parton species in the simulation, shows a much better match with the data than the charm-forced simulation. If one would place very stringent criteria on the data such that one would nearly only include D^0 decay particles the data would match the monte-carlo distribution for heavy flavour particles quite nicely.

5.3 Topological Cuts

Table 5.1: Topological selection criteria for D^{*+} used for analysis in p-p collisions, where hw stands for Half-width.

p_T (GeV/c)	1-2	2-3	3-4	4-5	5-6
Inv Mass D^0 (GeV/c ²)	0.03	0.032	0.032	0.032	0.036
DCA (cm)	0.0315	0.027	0.03375	0.042	0.05
$\cos \theta^*$	0.8	0.8	0.8	0.9	1.0
$p_T K$ (GeV/c)	0.5	1.0	1.0	1.	1.0
$p_T \pi$ (GeV/c)	0.5	1.0	1.0	1.	1.0
Imp. par. $d0_K$ (cm)	0.1	0.1	0.1	0.1	0.09
Imp. par. $d0_\pi$ (cm)	0.1	0.1	0.1	0.1	0.09
$d0_K \times d0_\pi$ (10 ⁻³ cm ²)	-0.33	-0.1	-0.1	-0.028	0.055
$\cos \theta_{point}$	0.865	0.9	0.83	0.81	0.79
Inv. M. hw D^{*+} (GeV/c ²)	0.3	0.3	0.3	0.3	0.3
Hw $M_{K\pi\pi} - M_{D^0}$ (GeV/c ²)	0.15	0.15	0.15	0.1	0.1
p_T min soft π (GeV/c)	0.05	0.05	0.05	0.05	0.05
p_T max soft π (GeV/c)	.5	0.5	0.5	100	100
Norm Decay Length_XY	4.	4.	0	0	0

In tables 5.1 and 5.2 the selection criteria for the D^{*+} used to obtain the central values of the analyses are mentioned, these values are obtained via an optimisation scheme.

The transverse momentum range mentioned is the full range in which one could get a reasonable signal with a significance of at least 3. For lower transverse momenta it was not possible to distinguish signal from background. For the highest transverse momentum bins, on the other hand, there was not enough statistics available to extract a raw yield. The criteria were acquired starting from the optimisation method explained in section 4.2.1. Then a few criteria were varied individually in the final sample to select the loosest high significance criteria. The normalised decay length specifically was only varied individually for low p_T intervals, because an extra criterion was necessary to acquire the best significance in these high background

Table 5.2: Topological selection criteria for D^{*+} used for analysis in p-p collisions at higher p_T , where hw stands for Half-width.

p_T (GeV/c)	6-7	7-8	8-12	12-16	16-24	24-36
Inv Mass D^0 (GeV/c ²)	0.036	0.036	0.05	0.094	.7	.7
DCA (cm)	0.1	0.1	0.105	0.1	.15	.125
$\cos \theta^*$	1.0	1.0	1.0	1.0	1.0	1.0
$p_T K$ (GeV/c)	1.0	1.0	1.0	0.3	0.3	0.3
$p_T \pi$ (GeV/c)	1.0	1.0	1.0	0.3	0.3	0.3
Imp. par. $d0_K$ (cm)	0.1	0.1	0.1	0.2	0.5	.5
Imp. par. $d0_\pi$ (cm)	0.1	0.1	0.1	0.2	0.5	.5
$d0_K \times d0_\pi$ (10 ⁻³ cm ²)	1	0.25	10	10	10	10
$\cos \theta_{point}$	0.7	0.8	0.68	0.6	0.6	0.6
Inv. M. hw D^{*+} (GeV/c ²)	0.3	0.3	0.3	0.3	0.3	0.3
Hw $M_{K\pi\pi} - M_{D^0}$ (GeV/c ²)	0.1	0.1	0.1	.15	0.3	0.1
p_T min soft π (GeV/c)	0.05	0.05	0.05	.045	0.05	0.05
p_T max soft π (GeV/c)	100	100	100	100	100	10000
Norm Decay Length_XY	0	0	0	0	0	0

intervals.

5.4 Raw Yield Extraction

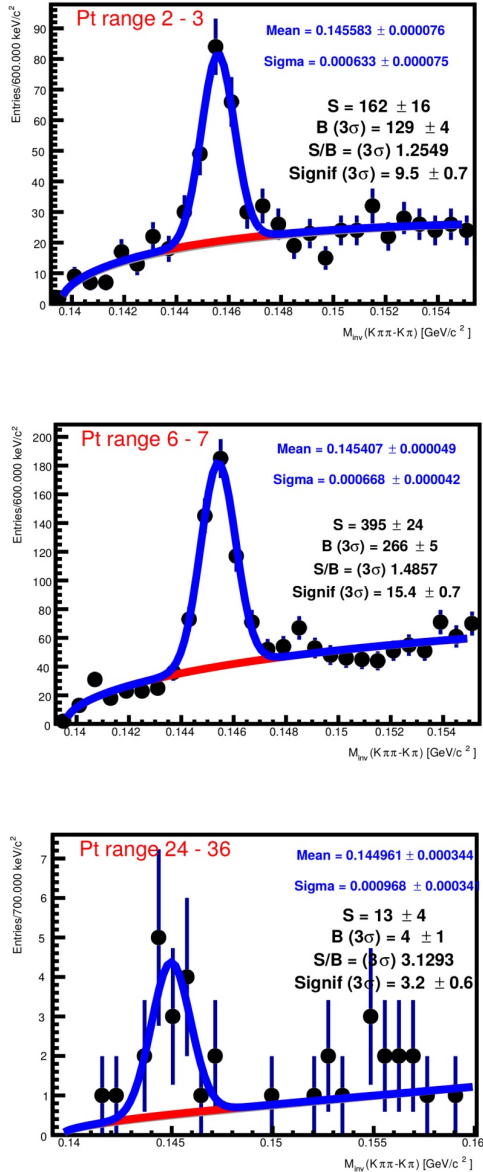


Figure 5.6: Invariant-mass-difference distributions of D^{*+} candidates and charge conjugates in a low, mid and high p_T interval as examples for pp collisions at $\sqrt{s} = 13$ TeV. The blue curve shows the fit function of a combined signal and background function, while the red line represents the background fit function.

Figure 5.6 shows the invariant mass distributions of selected intervals extracted with the selection criteria from section 5.3. For mass distribution for all p_T bins see Appendix A. Included in the figures are the mean and width of the Gaussian that was fitted for the mass-peak, the signal and background levels estimated at 3σ under the peak, as well as the signal/background level and the significance of each peak.

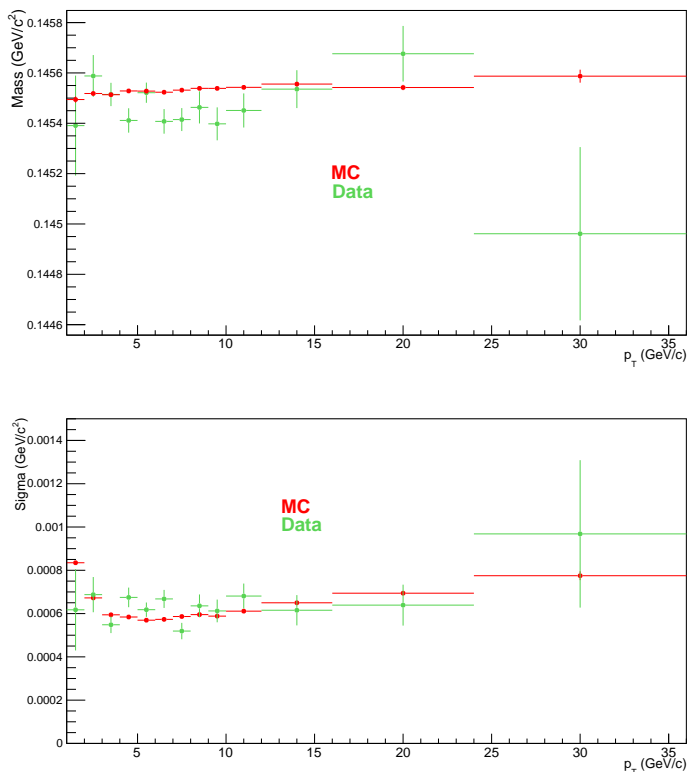


Figure 5.7: Top: the mean position of the mass-peak compared to that from simulations, bottom: the width of the Gaussian mass-peak, in both the results from data are shown in green and those of the simulations are shown in red.

To test the description of our signal distribution in the Monte-Carlo simulations, the width and the mean position of the peak are compared between data and simulation in figure 5.7. Note that the fluctuations seen for the mean position are fluctuations of less than 1 MeV, while the total invariant mass-difference is of the order of 145 MeV. On average we conclude that the results obtained in data are compatible with those obtained from simulations.

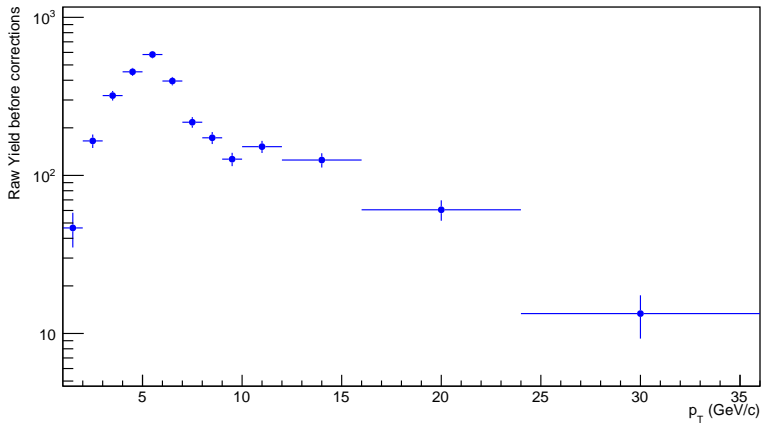


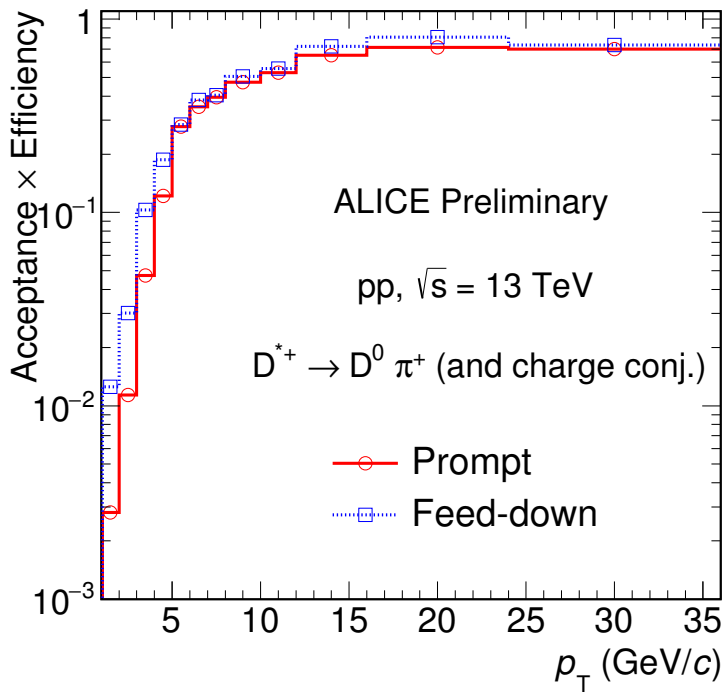
Figure 5.8: Raw yield in logarithmic scale with respect to transverse momentum interval before corrections.

In figure 5.8 the final values of the raw yields extracted are shown with the associated statistical uncertainties. The associated systematic uncertainties will be discussed in section 5.6.

5.5 Efficiency Corrections

The raw yield extracted in the previous section is uncorrected for both the influence of feed-down D^{*+} -mesons and the acceptance and efficiency criteria introduced by our detector or analysis. The acceptance and efficiency corrections for data are based on Monte Carlo simulations as described in chapter 4.

Proton-proton collisions at $\sqrt{s} = 13$ TeV were simulated with the requirement that each event contains a $c\bar{c}$ or $b\bar{b}$ pair produced at central rapidity $|y_q| < 1.5$. In this simulation the D-mesons are forced to decay via a hadronic decay channel of interest for the analysis. The events were generated using PYTHIA v6 with Perugia-2011 tuning. The responses and a detailed geometry of the detectors was combined with the GEANT3 particle transport package to simulate the effects of the appropriate detectors. The luminous region distribution and the conditions (active channels, gain, noise level, and alignment) of all the ALICE detectors and their evolution with time during 2016 were matched in the simulations. On these simulations the product



ALI-PREL-131132

Figure 5.9: Acceptance times efficiency of prompt and feeddown D^{*+} mesons with respect to the transverse momentum distribution.

of the detector acceptance and the efficiency were extracted and the distributions are shown in figure 5.9. The corresponding correction factors are combined with the FONLL predictions for the prompt fraction to correct the data for feed-down D-

mesons. Finally the $D^{*+} p_T$ -differential cross-section is calculated as shown in figure 5.15.

5.6 Systematics

For the analysis results extracted as highlighted in the previous section the following uncertainties were extracted:

- ◆ a feed-down uncertainty that varies between 2 and 9 percent,
- ◆ a topological selection criteria uncertainty that varies between 3 and 11 percent,
- ◆ a raw yield uncertainty of 21 percent at the highest transverse momentum range and varying between 2 and 9 percent for the other bins,
- ◆ the uncertainty on the p_T distribution of the tracks that is 4% below 2 GeV and 0 elsewhere,
- ◆ and finally a tracking uncertainty of 5.5 -7%.

This combines to a total uncertainty varying between 8 and 22%. The exact values can be found in appendix B. As the particle identification criteria were set to a 3σ correspondence in both TOF and TPC the uncertainty due to these criteria were negligible. Any non negligible uncertainties are discussed in the following subsections.

5.6.1 Raw Yield Uncertainties

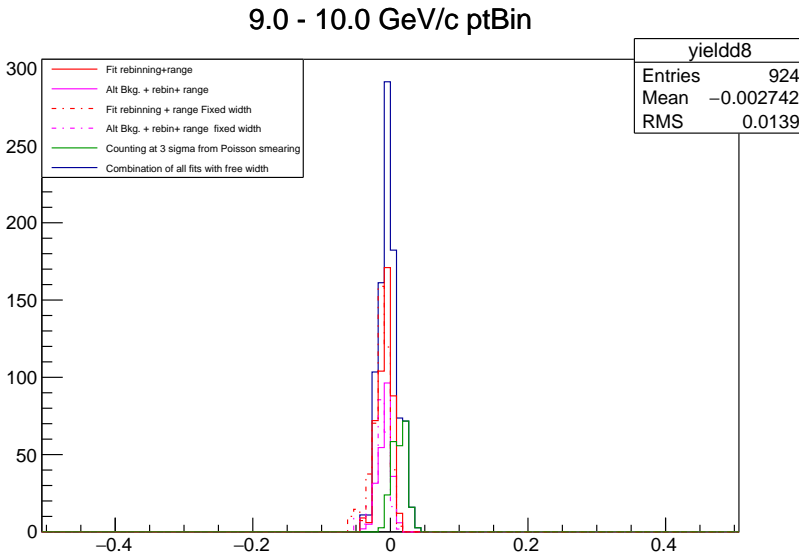


Figure 5.10: Distribution of the ratio of the difference between the various trials of the multi-fitter and the central hypothesis described in chapter 4 for the 9-10 p_T interval.

In figure 5.10 the distribution of the difference of the raw yield with respect to the central value from the various fits in the transverse momentum range from $9 \leq p_T \leq 10 \text{ GeV}/c$ is shown as an example. These distributions allows us to check if the extracted the central peak value is within the uncertainty fully compatible with the mean of the peak-value distribution. Furthermore any differences between the bincounting and alternative background distributions, pointing towards a wrong description of signal or background shape are easily spotted. These variations are done with free width for the main background, but as the alternative background does not reproduce the background as well, it increases the chance of including extra fluctuations into a wide peak, which is likely to contain extra background. Therefore we fix the peak width in the alternative background¹. For the alternative background the width of the Gaussian is fixed to the value found in the Monte Carlo simulations. If we do not fix the width in the alternative background one found extremely wide peaks these are very unstable fits, with corresponding large uncertainties on the fit. However as the criteria to allow a dit only require the width to fit the mean value within the fit uncertainty these results are not automatically rejected. Which makes it necessary to exclude such fits via a different method, in this case fixing the width to the Monte Carlo width. In tables 5.3 and 5.4 the RMS and mean of each distribution

p_T (GeV/c)	1-2	2-3	3-4	4-5	5-6	6-7	7-8
Mean ($\cdot 10^{-2}$),	-0.012	-0.62	0.46	-0.81	-0.47	0.79	0.60
RMS	0.077	0.058	0.023	0.034	0.0109	0.013	0.013
Prop. unc. (%)	7.7.	6.4	2.7	4.2	1.5	2.1	1.9
Final unc. (%)	8.	6.5	4.5	4.5	2.5	2.5	2.5

Table 5.3: Proposed uncertainties from raw-yield extraction for the D^{*+} for p_T up to 8 GeV

p_T (GeV/c)	8- 9	9-10	10-12	12-16	16-24	24-36
Mean ($\cdot 10^{-2}$),	-0.38	-0.27	0.30	0.1	0.72	-
RMS	0.0149	0.013	0.017	0.023	0.018	0.21
Prop. unc (%)	1.8	1.5	2	2.4	2.5	21
Final unc.(%)	2	2	2	2.5	2.5	21

Table 5.4: Proposed uncertainties from raw-yield extraction for the D^{*+} for p_T 8 - 36 GeV

are mentioned for all but the highest momentum bin. In the $24 < p_T < 36 \text{ GeV}/c$ interval the statistics were so low that few fits succeeded and the variation of those fits was very large. Therefore instead of the RMS the spread of the succesfull fits, i.e. the envelop of the highest and lowest, was used to determine the uncertainty in this p_T interval. These values are smoothened, from proposed uncertainty to final using the assumption that, due to the increase of the significance of the peak, the stability of the fit should increase up to $p_T \sim 10 \text{ GeV}/c$ and decrease after. The second decrease happens as at higher D^{*+} transverse momentum the stability of the

¹This was only necessary due to the available statistics, this is not required in for instance the p-Pb results later on

background function drops due to low statistics and thus the uncertainty of the fit will increase once more.

5.6.2 Variation of the topological selection cuts

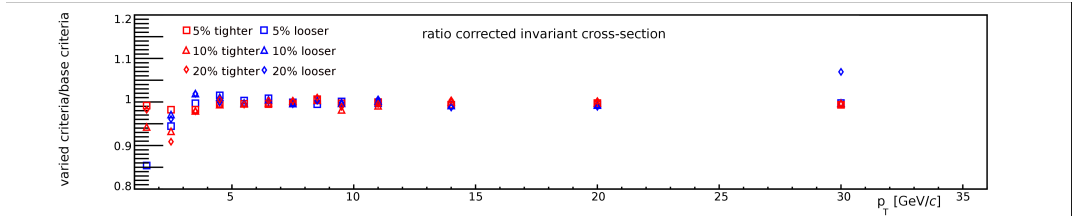


Figure 5.11: Difference in corrected yield collected from variations in selection criteria to stricter and looser variables as mentioned in chapter 4. Blue point denote topological selection cuts which are less stringent than the optimised value, while red denote more stringent criteria. The criteria are varied by 5, 10 and 20 % with respect to the value used in the central measurement.

The selection criteria were tested in 6 variations and the RMS of the distribution of results with a given p_T bin was used as a measure of the uncertainty. In the highest p_T interval the selection criteria were set to pre-selection level and the statistics were very low. In this case the statistical uncertainties are much larger than any systematic effect. We assigned a systematic error of 1% for this bin. For the first bin there is a strong fluctuation in the loosest criteria, which is not stable due to the high background level. One could not perform a stable fit for this bin, and with the very stringent requirements a 20% looser fit is quite an extreme difference to consider. As the other variations of the criteria were stable this result was excluded from the uncertainty. As one can see in figure 5.11 the for the lowest two p_T intervals, the other fits tend towards a slightly lower data value. This effect was only seen if the width was fixed to the that found in the central fits. In order to properly include the possibility of there being a bias in the uncertainty, this uncertainty was increased such that the centre of the distribution is included. Thus if this effect is due to a difference between data and Monte-Carlo simulations it is included within the systematic uncertainty on the selection criteria. The correction for the shape of the primary vertex distribution in the Monte Carlo simulation was estimated to have a 3% effect at all transverse momenta. In order to give a conservative estimate of the uncertainties the maximum of the measured selection criteria uncertainties and the correction effect was taken into account for the total uncertainty. For $D^{*+} p_T > 4 \text{ GeV}/c$ the uncertainty due to the correction was higher than the effect of the measured selection criteria uncertainties.

5.6.3 Feed-down uncertainty

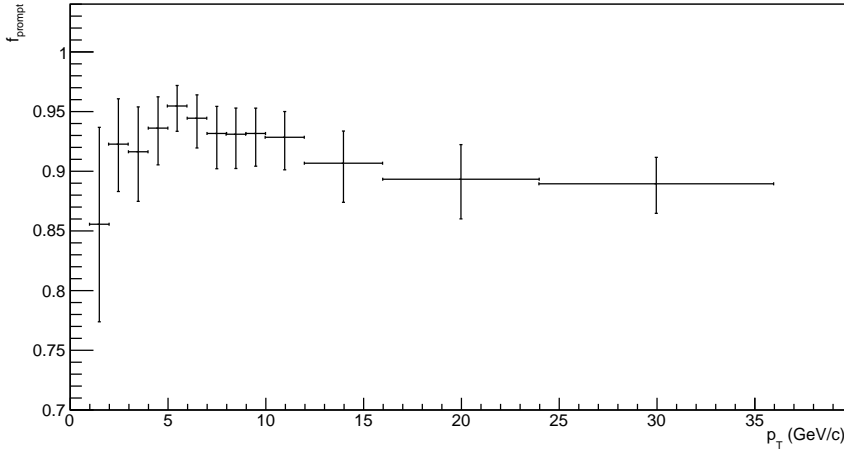


Figure 5.12: Theoretical charm fraction with uncertainties extracted from FONLL calculations.

The feed-down uncertainty is extracted as mentioned in section 4.6.6, and shown as uncertainty on the theoretical charm fraction for this measurement in figure 5.12.

5.6.4 Tracking

In this measurement the same method to estimate the uncertainty from track reconstruction was used as in run 1. This method assumes the same variations for the soft pion as done of the D^0 daughter particles. This should on average lead to slightly larger systematics than the method described in chapter 4. The method used here is consistent with the 7 TeV analysis, and, if anything, it should rather be conservative.

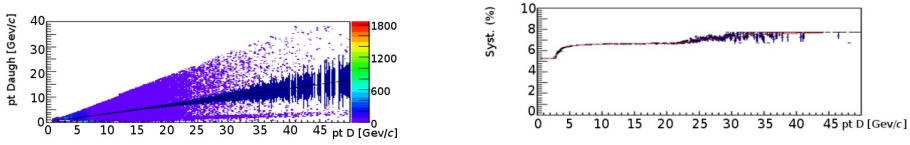


Figure 5.13: Left: The transverse momentum distribution of the pion and kaon coming from the D^0 on the y -axis with respect to the corresponding D^{*+} transverse momentum distribution on the x -axis, showing the width of possible combinations. Right: The distribution of propagated tracking uncertainty of the D^{*+} with respect to the D^{*+} transverse momentum, i.e. the combination of the uncertainty extracted from the left figure and that of the soft pion, the red line denotes the average value that is used for the final uncertainty per p_T -bin.

In figure 5.13 the distribution of the propagated uncertainty is shown on the right, while the left shows the p_T of the daughters corresponding to that of the D^{*+} , from this the uncertainty on the tracking is extracted.

5.6.5 Shape of the transverse momentum distribution in Monte Carlo simulations

The systematic effect of the generated p_T -shape of the D^{*+} on the efficiency coming from the simulations is extracted by computing the efficiency with and without using p_T -dependent weights. As the true p_T -shape is not known exactly it is assumed to be predicted reasonably well by FONLL, thus the difference between the generated spectrum used in the Monte Carlo and the prediction from FONLL is taken as the uncertainty. To illustrate the sensitivity of the results to the shape we also show results enforcing a flat p_T -distribution. As this is an unrealistic assumption, it will not be used in the uncertainty estimates. In figure 5.14 the distribution of the product of the efficiency times acceptance are shown in the upper panel for all three options. The lower panel shows the ratio of the weighted distributions to the standard value. An uncertainty of 4 percent is assigned in the first bin and it is considered negligible for transverse momenta higher than $2 \text{ GeV}/c$.

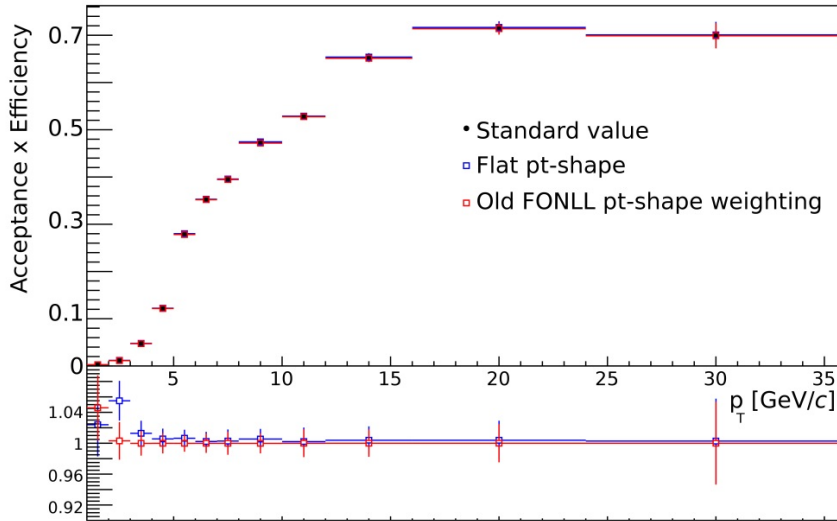
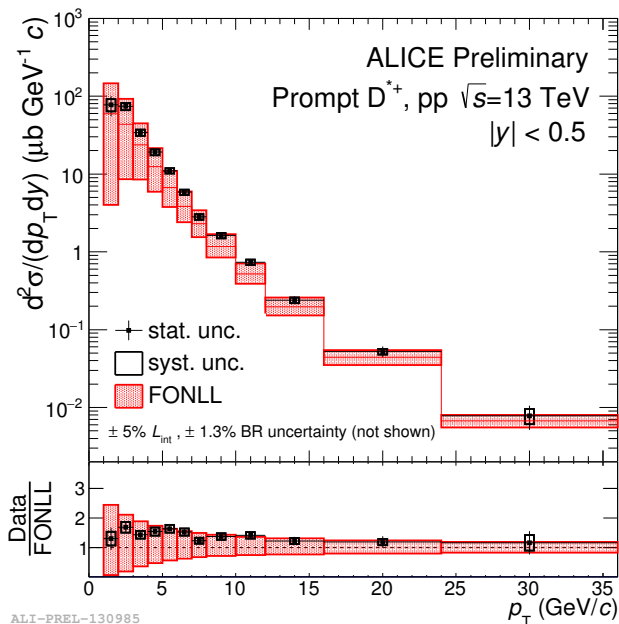


Figure 5.14: Product of efficiency times acceptance for prompt D-mesons with various p_T -distribution weights in the upper panel and the ratio of the acceptance times efficiency with different p_T weights

5.7 Results



In figure 5.15 the final D^{*+} production cross-section is shown compared to FONLL calculations. The D^{*+} production cross-section matches the FONLL predictions within uncertainties, while being consistently close to the upper one σ limit of the theoretical prediction. This is consistent with D^{*+} -meson results collected by ALICE at other collision energies. Note the 8-9 and 9-10 GeV/ c p_T intervals were merged for the final cross-section. These bins were merged to allow for interval by interval comparison to earlier measurements at centre of mass energies of 7 and 8 TeV.

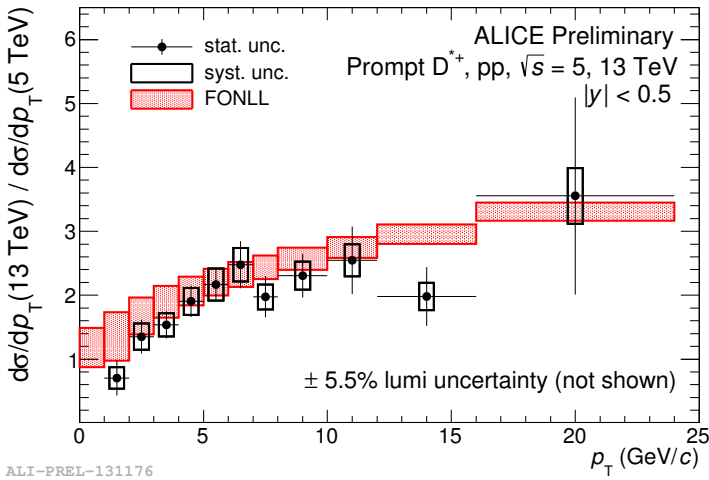


Figure 5.16: Ratio of the p_T -differential production cross section of prompt D^{*+} -mesons in the interval $1 < p_T < 36$ GeV/ c , in pp collisions at $\sqrt{s} = 13$ TeV divided by the preliminary results at 5 TeV compared to the ratio of FONLL pQCD calculations.

We compare the results between the 5 and the 13 TeV sample both from run 2. The ratio between the two run 2 measurements is shown in figure 5.16. The new measurement for the D^{*+} in run 2 allows us to compare the two energies over a much wider p_T -range.

From figure 5.16 we conclude that the energy ratio is compatible with the predictions of FONLL within uncertainty. The central value is not always fully included in the uncertainty band but the difference is compatible within statistical uncertainty. This first results is in agreement with the behaviour we have seen consistently at various energies of collisions for the D^{*+} . However a full statistics measurement of the 13 TeV sample might be able to show whether there is a significant difference between theory and measurement.

D-mesons in 5.02 TeV p–Pb collisions in run II

In 2016 the LHC collided protons with lead ions at $\sqrt{s_{NN}} = 5.02$ TeV, these collisions allow us to probe cold matter effects, such as discussed in section 2.3. The D-meson R_{pPb} , reported in this thesis, gives a precise measurement of initial state effects on the p_T -distribution of heavy flavour particles.

A comparison of these new results with respect to Pb–Pb and proton-proton collisions at the same energies can help to disentangle the cold nuclear matter effects that are present in heavy ion collisions from the final state effects. We will also report multiplicity dependent measurements. These are becoming more interesting as a positive v_2 is measured in high-multiplicity p–Pb collisions, which is seen as a sign of collectivity in heavy ion collisions.

In this chapter the data sample and reconstruction of the D^{*+} -meson will be described in more detail, highlighting our D-meson R_{pPb} results.

The results mentioned in this chapter are published in [78], a publication to which the author of this thesis contributed.

6.1 Open questions from run I

From the first proton-lead run in 2013, amongst many other measurements, an invariant mass analysis leading to the first D-meson R_{pPb} was performed. A comparison between the results from the 2016 data to the 2013 data, in the 2013 transverse momentum bin highlights mostly the increase of statistics by a factor 6. In figure 6.1 one can see the significant reduction in statistical uncertainty of the order $\sqrt{6} \approx 2 \sim 2.5$.

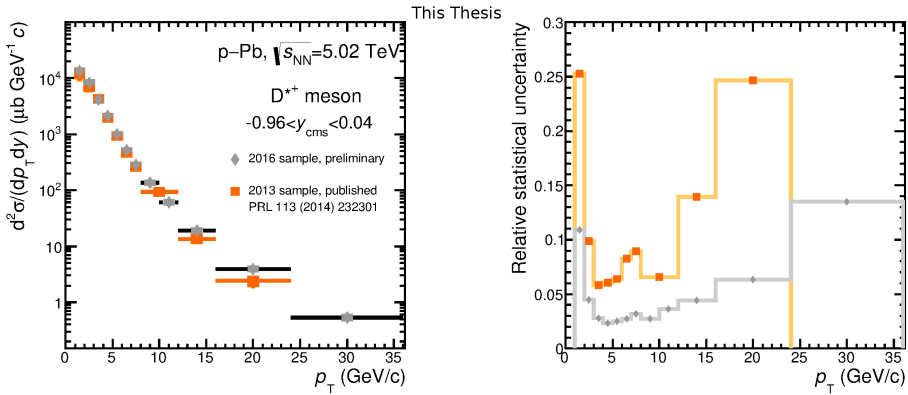


Figure 6.1: Statistical uncertainty difference between the preliminary values of 2016 for the invariant cross-section compared to that of 2013.

The 2013 result allowed for the R_{pPb} measurement seen in figure 6.2. It is important to take into account that only part of the uncertainties are due to the smaller data sample. The uncertainties of the 2013 R_{pPb} also include a contribution due to the energy scaling of the proton-proton reference. A sample of proton-proton collisions at $\sqrt{s} = 5.02$ TeV was not yet available in 2013. Thus energy-scaled results from pp collision at $\sqrt{s} = 7$ TeV were used as a baseline for the comparison between proton-proton and proton-lead results. This method was tested and well documented to provide a baseline for the early recorded Pb–Pb collisions at $\sqrt{s_{NN}} = 2.76$ TeV. Furthermore the energy scaled 7 TeV sample was available up to a p_T of 24 GeV/c , this measurement had the largest range in terms of D- p_T that was available at that time.

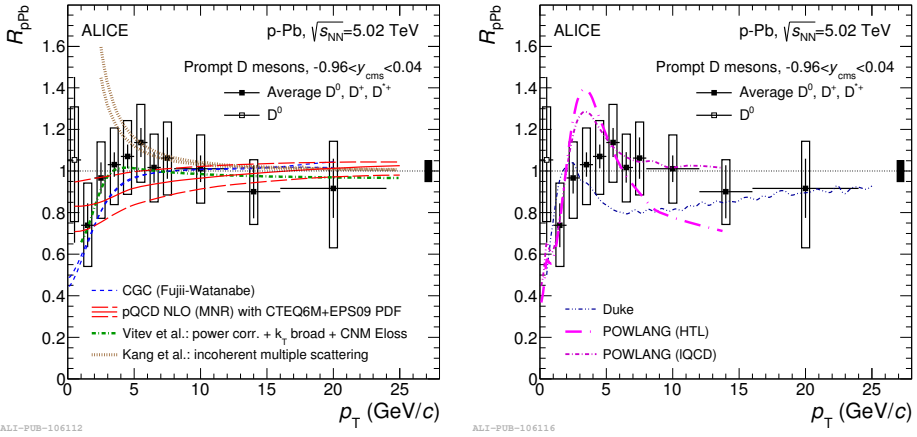


Figure 6.2: On the left models with only cold nuclear matter effects namely: CGC [82], NLO pQCD [83] with EPS09 nPDFs [51], a LO pQCD calculation with CNM effects (Vitev et al.) [84] and a calculation based on incoherent multiple scatterings (Kang et al.) [85]. On the right models with QGP formation included namely: Duke [44] and POWLANG [86], for more on these models see section 2.3 and 6.6, figures from [87]

Our first results were dominated by statistical uncertainties, so they did not allow any strong conclusion regarding the trend of the nuclear modification factor. There are differences between models including only initial state effects and those including a small Quark-Gluon Plasma medium in proton-lead collisions. The combination of a new proton-proton reference that was collected in 2017 and a six times larger data sample of p-Pb collisions could provide a more precise measurement, which might finally allow to discriminate between different model predictions. In the rest of the chapter the results of the 2016 analysis will be reported, including the dominant uncertainties on this measurement.

6.2 p–Pb data sample

After event selection the number of events was about $6 \cdot 10^8$ with a corresponding integrated luminosity, $L_{\text{int}} = 292 \pm 11 \mu\text{b}^{-1}$. The visible cross-section was measured via a van der Meer scan as $\sigma_{\text{MB}} = 2.09 \text{ b}$, where the statistical uncertainty is negligible compared to the systematic uncertainty of 3.7% [75].

A beam energy of 4 TeV for protons and 1.58 TeV per nucleon for lead nuclei was used to reach the target centre-of-mass energy of $\sqrt{s_{\text{NN}}} = 5.02 \text{ GeV}/c$. This implies that the nucleon-nucleon centre-of-mass system moves in rapidity by $\Delta y_{\text{cms}} = 0.465$ in the direction of the proton beam. The D-meson analyses are performed in the laboratory-frame interval $|y_{\text{lab}}| < 0.5$, the rapidity coverage in the centre-of-mass frame is equal to $0.96 < y_{\text{cms}} < 0.04$.

As discussed in chapter 4, the V0, ITS and TPC are used to select an event for our analysis. However it is not necessary to have all parts of the ITS available for the data-taking. Only 2 hits in the ITS per track are required of which at least one in the SPD, thus it is not necessary for both the SDD and the SSD to be available to be able to select events for this analysis.

In the 2016 data taking period, the SDD was not always available for data taking, resulting in two samples: a central barrel sample in which the full ITS is available, and a FAST sample in which the SDD is not available. In order to be certain that both samples could be combined extensive test were conducted. For instance, the data in the central barrel sample was reconstructed with and without using the information of the SDD. These samples were used to compare the central barrel sample to the fast sample under the same conditions.

The differences that were found between the samples were sufficiently small to allow the merging of the samples as can be seen in 6.3. The advantage in merging the samples is that the improvement in the statistics significantly reduces statistical fluctuations, which in particular makes the fits of the raw yield in the invariant mass spectra more robust.

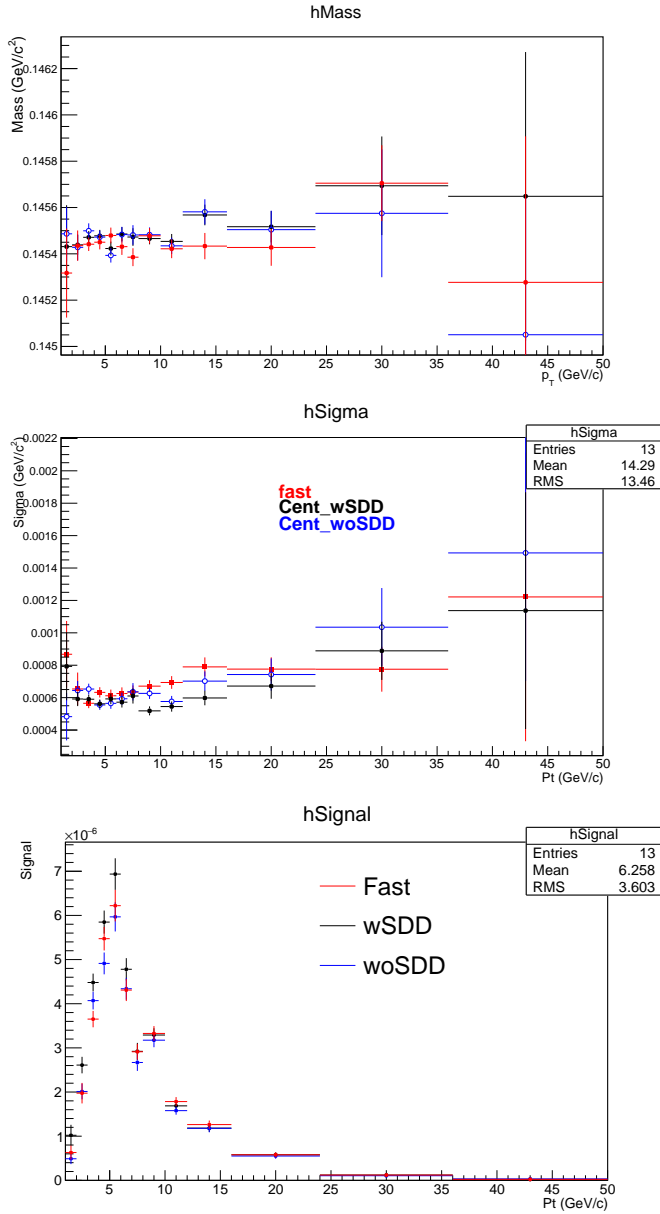


Figure 6.3: Top: The mean position of the mass-peak compared between the Fast sample and the sample with SDD reconstructed with and without SDD.

Middle: The width of the gaussian mass-peak, Bottom: Signal per Event. In all the results the red data points represent the FAST sample results, the black the reconstructed sample with SDD included and the blue the same sample as the black, but reconstructed without SDD information. The 36-50 GeV/c p_T -interval is shown here, but will not be used in the final results as this bin had insufficient statistics.

6.3 Topological Selection Criteria

In table B.2 in appendix C the central selection criteria for the D^{*+} are reported in the transverse momentum bins in which they were optimised.

In addition to these selection criteria a particle identification via dE/dx in the TPC within 2σ for the D^0 decay products for transverse momenta below $2 \text{ GeV}/c$ and within 3σ above $2 \text{ GeV}/c$ was required, for the identification via the TOF a requirement of a signal timing within 3σ was used if TOF results were available. There was not enough statistics available to get a stable result for transverse momenta above $36 \text{ GeV}/c$ even without a request for particle identification information.

After a general optimisation was done as highlighted in chapter 4, the selection criteria were specifically optimised further for this data set. More stringent selection variables with respect to the proton-proton case will slightly reduce the signal in proton-lead collisions, however they are needed to sufficiently reduce the background processes. The main difference between these criteria in p–Pb and the ones for pp are in the stricter cut on the normalised decay length of the D^0 up to $8 \text{ GeV}/c$.

6.4 Raw Yield Extraction

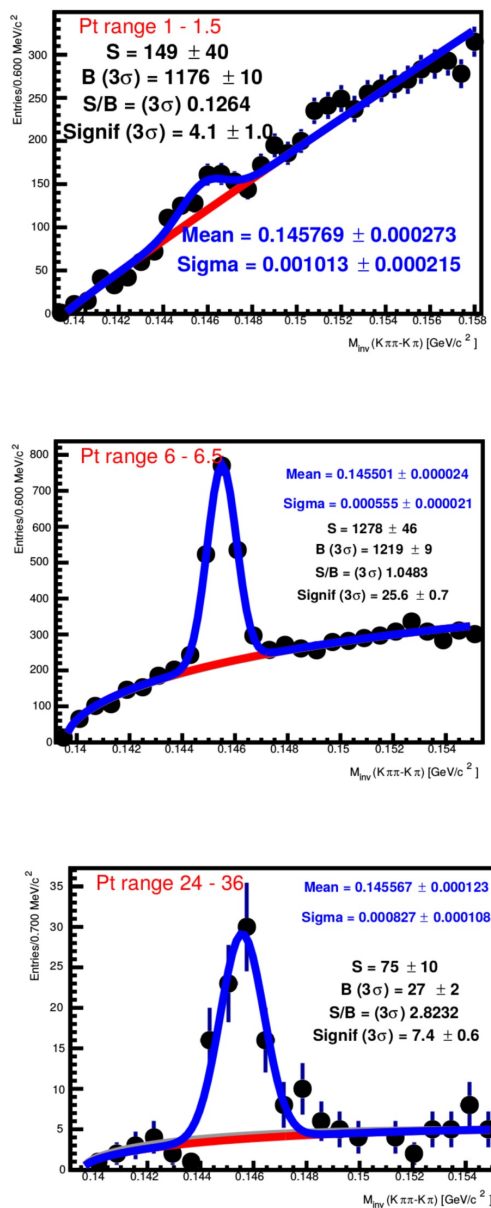


Figure 6.4: Invariant-mass-difference distributions of D^{*+} candidates and charge conjugates in the three p_T intervals for a sample of p–Pb collisions at $\sqrt{s} = 5.02$ TeV. The blue curve shows the fit function of a combined signal and background function, while the red line represents the background fit function.

Figure 6.4 shows examples of the invariant mass distributions extracted with the selection criteria from section 6.3, in 7.3 one can find the full sample. Included in the figures are the mean and width of the gaussian that was fitted for the mass peak, the signal and background levels estimated within 3σ around the peak, the signal/background level and the significance of each peak. As you can see there is a peak fitted for the 1-1.5 GeV/c p_T interval. This p_T interval is not used in the final results, as the signal/background level is quite poor and the width of the peak is very unstable. Reassuringly the sum of the 1-1.5 GeV/c p_T bin and the one from 1.5-2 GeV/c is equal to the bin from 1-2 GeV/c. The final cross-section and the corresponding R_{pPb} are reported for p_T from 1.5 GeV/c to 36 GeV/c.

In figure 6.5 the mean, width and raw yield are shown in the final binning compared to that in coarser binning in which the selection criteria are optimised. The trend of the results are in agreement with each other for both the width and mean. The results achieved with both a 2 and 3 σ TPC requirement are shown. The final reported cross-section utilizes a 2 σ selection criterium in the TPC up to 2 GeV and a 3 σ above it. The raw yield reported in the coarser transverse momentum binning is in agreement with the sum of its parts in the fine binning within uncertainties. The 3 σ setting is less stringent allowing for a larger raw-yield, but after corrections the cross-sections for 2 and 3 σ are very similar. The final values used in the calculation of the cross-section are those in the fine binning. The associated systematical uncertainties will be discussed in section 6.6.

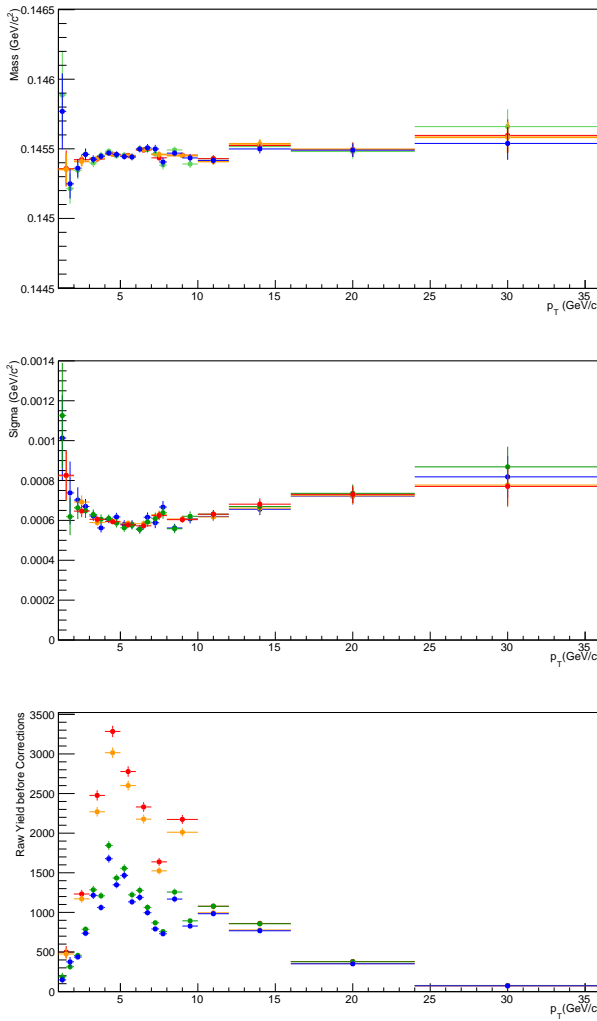


Figure 6.5: Top: the mean position of the mass peak compared to that from coarser binning, Middle: the width of the gaussian mass peak, Bottom: Raw yield. In all panels the results with 2σ TPC selection criteria in fine binning are shown in blue, with the 3σ criteria in green and those of the coarser binning are shown in orange for 2σ and in red for 3σ .

6.5 Efficiency Corrections

The acceptance and efficiency corrections are based upon Monte Carlo simulations as described in chapter 4.

To mimic p–Pb collisions one does not have a single simulation as was available for proton-proton. Instead the number of participants in a collision is extracted for each Pythia event via a Glauber MC simulation. If the extracted number of binary collisions is larger than 1, a HIJING p–Pb event is added as the underlying event. For these simulated collisions each event was required to contain either a $c\bar{c}$ or $b\bar{b}$ pair. Furthermore the D-mesons are forced to decay via a hadronic decay channel of interest for the analysis. The PYTHIA events were generated using PYTHIA v6 with Perugia-2011 tuning. The detector response and detailed geometry were included in the GEANT3 particle transport package. The configuration mimics the runs used in data and reproduces the conditions of all ALICE subsystems as well as the luminosity. Due to the two sub-samples with different conditions, a specific simulation sample was created for each subsample and for the final results the combination of efficiencies was weighted with the number of events used per sample in data. From

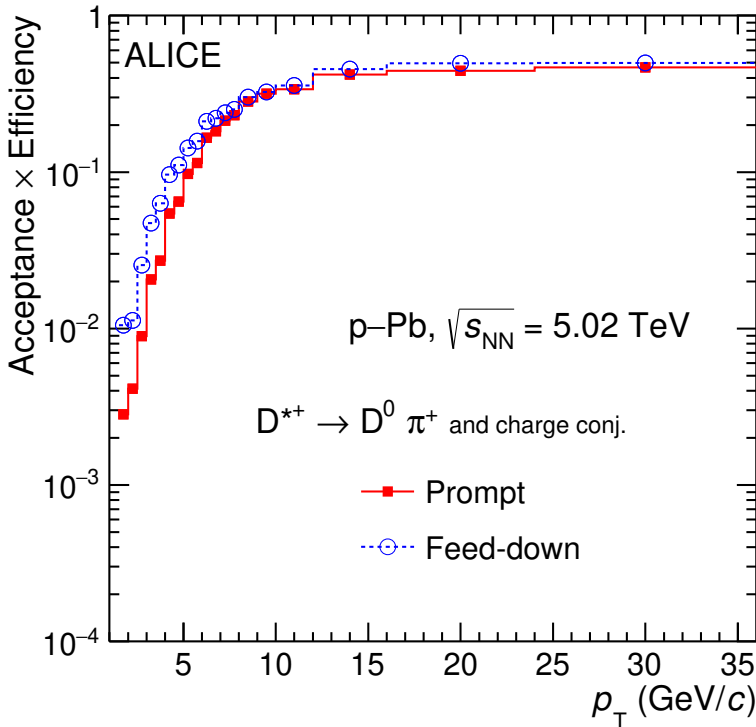


Figure 6.6: Acceptance times efficiency of prompt and feeddown D^{*+} mesons as a function of transverse momentum. .

this the acceptance times efficiency distribution of figure 6.6 were extracted. The

acceptance and efficiency are combined with the FONLL predictions for the prompt fraction to correct the results for the influence of feed-down D^{*+} -mesons. The corresponding p_T -differential cross-section is calculated and shown in figure 6.14.

6.6 Systematic uncertainties

Tables 6.1 and 6.2 include the systematics uncertainties derived from the different analysis steps. The following sections will give a justification for the uncertainties mentioned in the table. The uncertainty on the feed down was calculated separately for each transverse momentum bin and is included in the total uncertainty.

Table 6.1: Systematic uncertainties extracted for the final results in p–Pb collisions at 5.02 TeV in run 2 at low p_T

p_T (GeV/c)	1.5-2	2-2.5	2.5-3	3-3.5	3.5-4	4-4.5	4.5-5	5-5.5	5.5-6
Raw Yield(%)	7	7	5	3	3	3	3	2	2
Selection criteria (%)	4	2	2	2	2	2	2	2	2
PID (%)	1	0	0	0	0	0	0	0	0
Tracking (%)	3.2%	3.2	3.2	3.2	3.2	3.2	3.2	3.2	3.2

Table 6.2: Systematic uncertainties extracted for the final results in p–Pb collisions at 5.02 TeV in run 2 at mid to high p_T

p_T (GeV/c)	6-6.5	6.5-7	7-7.5	7.5-8	8-9	9-10	10-12	12-16	16-24	24-36
Raw Yield new (%)	2	2	2	2	2	2	2	2	2	4.5
Selection criteria (%)	2	2	2	2	2	2	2	2	2	2
PID (%)	0	0	0	0	0	0	0	0	0	0
Tracking (%) sp	3.2	3.2	3.2	3.2	3.5	3.5	3.5	4	4	4.5

The p_T -shape of heavy flavour particles in the simulations is not mentioned in the table. The estimation of this uncertainty is done based on the differences between the FONLL-predicted shape of the transverse momentum distribution and the shape as is produced by the Monte-Carlo simulation which were found to be negligible.

6.6.1 Raw yield uncertainty

The raw yield uncertainties have been extracted varying the binning, fit range, background function and using bincounting instead of the fit value for the peak.

A special choice has been made for the transverse momenta interval of 1.5-2.0 GeV/c. In this bin the background is better described by a powerlaw, and would not fit with the normal background function unless fixed to the width as given by Monte Carlo, so this sample is taken into account with fixed width for the fit function.

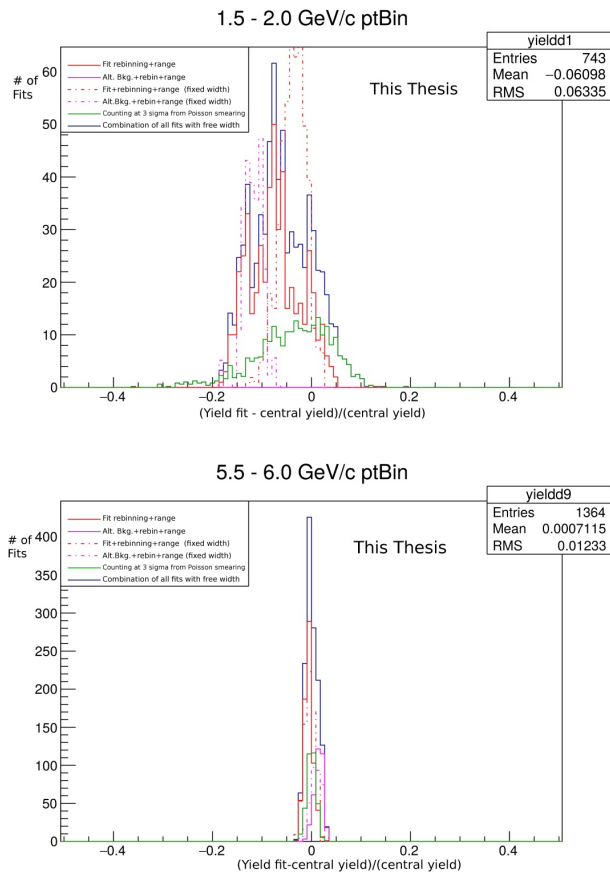


Figure 6.7: Yield different fits and bin counting with a Poisson smeared distribution. Upper: p_T -interval 1-2 GeV/c, in which the alternative background hypothesis is the same as the central hypothesis background that is used in the other bins. Bottom : p_T -interval 5-6 GeV/c, one of the lower central p_T intervals.

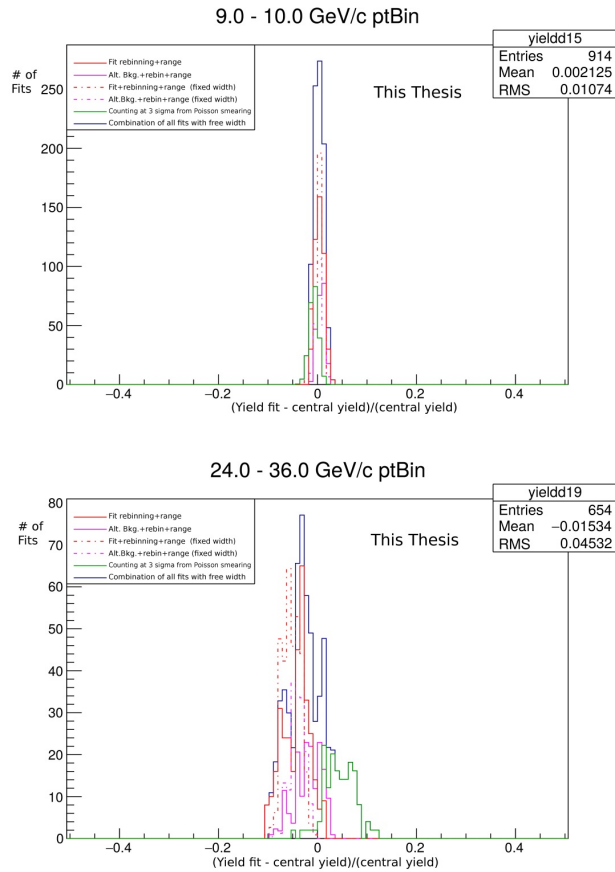


Figure 6.8: Yield difference for various fits and bin counting with a Poisson smeared distribution. Upper: p_T -interval 9-10 GeV/c higher central bin. Bottom: highest p_T -interval 24-36 GeV/c

In figure 6.7 two examples are shown at lowest and mid low and in 6.8 at mid high and highest p_T -bins. The distributions for the different fitting options are shown allowing us to see if the fit selected as a central value is within 1σ of the mean of the distribution. This is done as the mean is not always an actual fit value, and the fit should at least be high enough quality at that value. Furthermore the differences with respect to the bincounting and alternative background distribution shapes can be seen. For the p_T interval from 1-2GeV/c one might note that the uncertainty is set at 7 percent, while the width is 6.3 as obtained from figure 6.7. This includes the part of the distribution for which the fits were stable, and includes the mean of the distribution. These variations are done both with free and fixed width of the distribution. The final values are based on the fixed width, i.e. the values where the width was fixed to the value found for the Monte Carlo simulations. This was necessary to exclude outliers that are not rejected by our earlier criteria due to a

large uncertainty on the width.

The total uncertainty was estimated as the RMS of the combined weighted distributions. The weighing factor was chosen such that rebinning has the same weight in terms of uncertainty to the fit range and the same weight as to the bin counting option and the alternative fit weight. The final values are mentioned in tables 6.1 and 6.2.

6.6.2 Variation of the topological selections

The selection criteria variation was applied in the coarse transverse momenta bins, for which the criteria were optimized. The same variations were applied to the finer binning and shown to be compatible with these results.

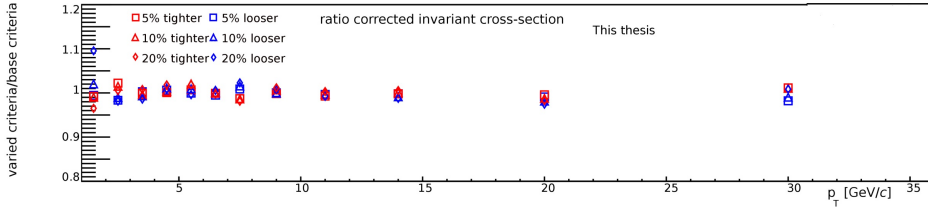


Figure 6.9: Variations in selection criteria to stricter and looser variables as mentioned in chapter 4. In blue looser variations, ranging from (block-shape) 5 to 20 (diamond) in central p_T bins, in red stricter variations

The most sensitive topological variables, i.e. the cosine of the pointing angle, the DCA, the product of impact parameters and the minimal normalised decay length were varied simultaneously with 5, 10 and 20% of their value¹ except for the highest transverse momenta. The selection criteria for this interval were changed by more than 20% in order to have any visible influence on our high p_T data, as the usual percentages showed no visible effect on the mass-figures. The variations that allowed the extraction with an invariant-mass fit that had a significant fitted peak are shown for the highest transverse momentum interval.

6.6.3 Particle Identification - and Feed-down uncertainty

The uncertainty on the particle identification has been extracted via a new method. The particle identification precision is checked at decayed particle species level per transverse momentum bin, separately for the non-soft kaon and pions. Based on the Monte-Carlo distributions for the decay products the results are propagated to the specific D-mesons species via simulation. This check was done for both the D^0D^+ and D^{*+} and it was concluded that if identification of the decay daughters is required within 3σ in the TPC there is no significant bias, as the average difference was found to be at per mille level. Therefore a negligible uncertainty is assigned for a momentum above $2\text{ GeV}/c$.

For the first transverse momentum bin a particle identification in the TPC within 2σ was required, for this an uncertainty of 1% was assigned. The found uncertainty coming from the combination of daughter particles contributing to this p_T -bin was between 0,5% and 1% level.

¹or their difference to the absolute maximum in the case of the cosine of the pointing angle

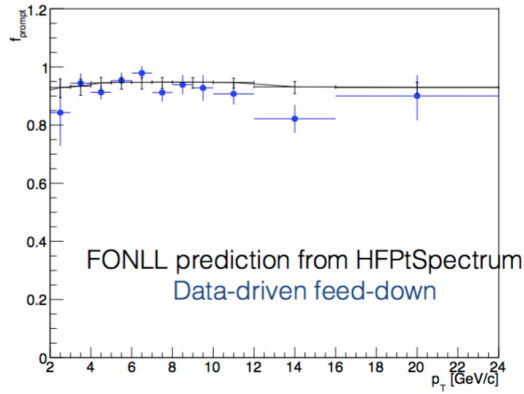


Figure 6.10: The measured charm fraction in blue as a function of transverse momentum as compared to the theoretical values from FONLL predictions used in this analyses.

The fraction of the charm particles based on predictions from FONLL are shown in figure 6.10 and are compared to the results from the data-driven method. The uncertainty on the predictions are extracted via the variations highlighted in section 4.4.

6.6.4 Tracking uncertainty

The uncertainties on the tracking are extracted as mentioned in section 4.6.2. For the uncertainty due to the tracking variations on the D^0 decay products the TPC criteria variations were applied both in the analysis of all prompt D^0 and in the D^0 selected by D^{*+} topological selection. For D^{*+} topological cuts the effect of the TPC tracking variations were smaller or equal to those for all prompt D^0 . Thus the uncertainty on the tracks due to the TPC selection was set to 0.5% per track, as found from D^0 variations. In addition a 1% ITS-TPC matching uncertainty per track was extracted for daughter particles between 1 and 8 GeV/c and a 2% uncertainty was extracted for higher and lower transverse momentum daughters.

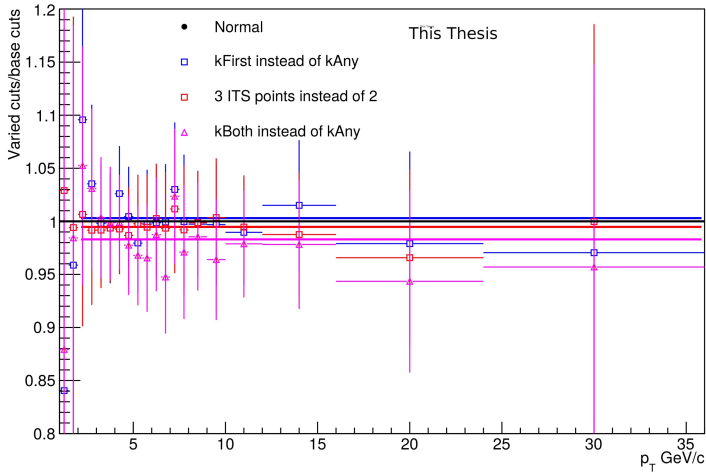


Figure 6.11: The ratio between the resulting yield with varied soft-pion trackings criteria compared to the base criteria. The solid lines show average over the full transverse momentum range for ratio of the yield of the variations.

For the soft pion the variations were done on the ITS criteria, and a 1.5% uncertainty was set based on the results of figure 6.11.

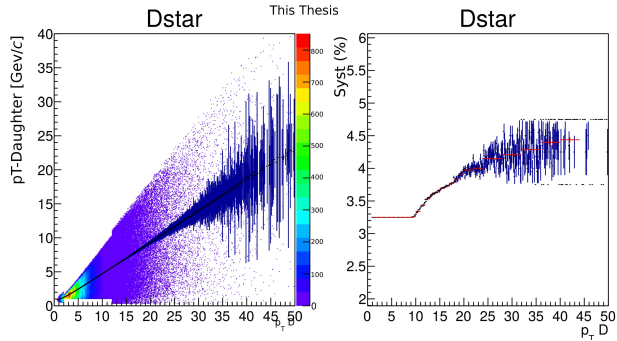


Figure 6.12: Left: The transverse momentum distribution of the pion and kaon coming from the D^0 on the y -axis as a function of the corresponding D^{*+} transverse momentum distribution on the x -axis, showing the width of possible combinations. Right: The distribution of propagated tracking uncertainty of the D^{*+} with respect to the D^{*+} transverse momentum, i.e. the combination of the uncertainty extracted from the left figure and that of the soft pion, the red line denotes the average value that is used for the final uncertainty per p_T -bin.

The D^0 ITS-TPC matching uncertainty was propagated from daughter transverse momenta to the associated D^{*+} , and quadratically summed with the TPC and ITS tracking uncertainties. Finally the combined values were extracted via the average of the distribution per bin as shown in figure 6.12.

6.6.5 Total uncertainty on the Nuclear modification factor

For the nuclear modification factor only the uncertainty on the feed-down correction has to be recalculated for the ratio of cross sections by consistently varying the FONLL calculation parameters in the numerator and in the denominator. The other uncertainties are considered independent between proton-proton and proton-lead collisions and thus added quadratically.

6.7 pp-reference

Proton-proton collisions in the large hadron collider are mainly done at the highest energy feasible at that time, to allow the best data for new particle searches. Thus to provide a proton-proton reference at energies where no data sample was available ALICE used their best proton-proton reference available and scaled it to the energy of the proton-lead or lead-lead collision for which a reference was needed.

In some cases there was a sample available at the correct energy, but the integrated luminosity of these samples did not allow precise enough measurements to reduce the uncertainties with respect to the uncertainties on an energy scaled sample. For the new samples at $\sqrt{s_{NN}} = 5.02$ TeV this energy scaling is no longer needed as a sample of proton-proton collisions at that energy was collected in 2017. This sample with an integrated luminosity of $L_{\text{int}} = (19.3 \pm 0.4)nb^{-1}$ allows a precise enough measurement for most transverse momenta bins.

This measurement has a range in D^{*+} momenta from 1.5-36 GeV/c and is measured in the same binning as our new p-Pb results. The nuclear modification factor calculated with the combination of these two samples allows for a good precision. Furthermore as the detector settings and quality between 2016 and 2017 were very similar, some remaining detector effects will not only be covered by the uncertainties, but could still cancel out in the ratio. The results shown in figure 6.13 have been compared to the older energy scaling and the results at different energy collisions in [81] and were concluded to be in good agreement with each other.

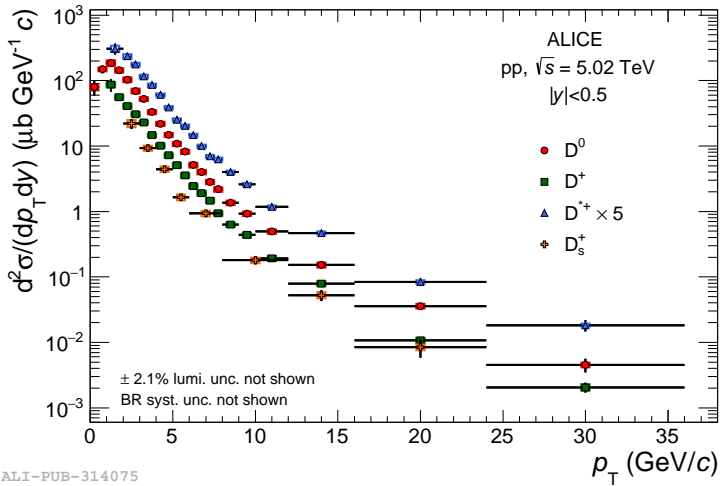


Figure 6.13: p_T -differential production cross sections for prompt D^0 , D^+ , D^{*+} and D_s^+ mesons in pp collisions at $\sqrt{s} = 5.02$ TeV are shown, for the D^0 the results in $0 \leq p_T \leq 1$ was obtained from analysis without decay vertex while the other bins are from the analysis with decay-vertex reconstruction. The D^{*+} results have been multiplied by 5 for a better visibility. Figure from [81].

6.8 Results

The nuclear modification factor in proton-lead collisions is calculated using the p_T -differential D^{*+} -meson cross-section in both proton proton and proton-lead collisions, as was mentioned in section 4.5. With that goal the p_T -differential cross-section in proton-lead collisions is extracted.

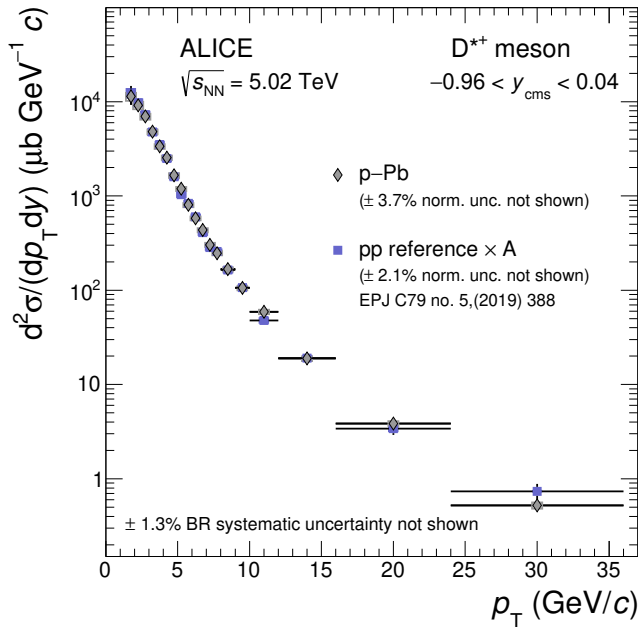


Figure 6.14: p_T -differential production cross sections for prompt D^{*+} mesons in proton-lead compared to proton-proton results .

The nuclear modification factor of prompt D^{*+} -mesons is studied to search for a possible effect of possible cold nuclear effects on the charm quark. With this goal in mind measurements of the D^0 and D^+ -mesons will finally be combined with the D^{*+} -meson in an average D-meson nuclear modification factor to reduce the uncertainties on the measurement. Here we will first take a look at the different D mesons species separately. The D^0 and D^+ measurements are reconstructed with $p_T > 1 \text{ GeV}/c$ in a hadronic decay channel via analyses based upon the secondary vertex displaced decay topology. For the D^0 a result down to a p_T of 0 GeV/c is obtained via a technique based on background estimation and subtraction². In figure 6.14 the cross-section is shown in the final binning (compared to that of the proton-proton collisions at 5 TeV). This results in a nuclear modification factor for the D^{*+} as shown in figure 6.15.

²For these very low momenta it is currently not possible to obtain a result using the topological decay analysis

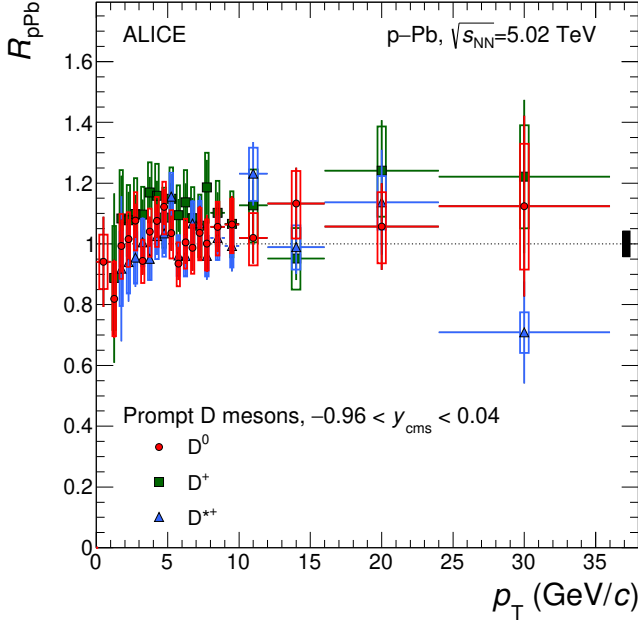


Figure 6.15: Nuclear Modification factor R_{pPb} as measured for the separate D-mesons before averaging between the mesons.

The average of the three D-mesons is calculated using the inverse uncertainties as weights and the systematic uncertainties are propagated through the weighted average. Only the uncertainties due to tracking efficiency and beauty feed-down correction are considered fully correlated between the three measurements, and summed correspondingly. The resulting R_{pPb} is compatible with unity over the p_T interval covered as well as in agreement within uncertainties with most models.

In the left panel of figure 6.16 four different models including cold nuclear matter effects are displayed: Colour Glass Condensate [82, 88] is a calculation based on the Color Glass Condensate formalism, the second model is a FONLL calculation [45] in which CTEQ6M PDFs [89] and a EPPS16 NLO nuclear modification [49] are included, the third is a calculation at Leading Order in which intrinsic k_T broadening, nuclear shadowing and energy loss of the charm quarks in cold nuclear matter (Vitev et al.) [84] are included, and the fourth and final is a higher-twist calculation based on incoherent multiple scatterings (Kang et al.) [85].

The first three calculation describe the data within the combination of uncertainties on the data and theory. The Colour Glass Condensate calculation is at the edge of the uncertainty overlap between the data and the theory for D-meson transverse momenta above 3 GeV/c. The model Kang et al. is disfavoured for transverse momenta below 4 GeV/c.

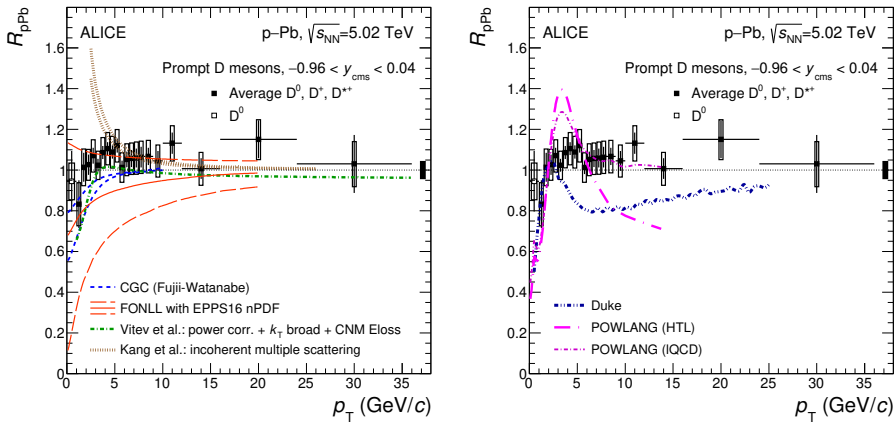


Figure 6.16: The average D-meson R_{pPb} at 5.02 GeV/c with the new sample compared to various models, on the left models including only cold nuclear matter effects, on the right models including also the formation of small Quark Gluon Plasma. Nomenclature and reference of the models: CGC [82, 88], FONLL with EPPS16 NLO [49], Vitev et al. [84], Kang et al [85], Duke [44] and POWLANG [86]

In the right panel of 6.16 the results of two transport model calculations, which include a Quark Gluon Plasma in proton-lead collisions, are compared to data. These models are Duke [44] and POWLANG [86], of which in the later only collisional processes are include, while Duke also includes radiative energy loss.

Both models consider the QGP as an expanding deconfined medium and calculate the transport of heavy quarks via a Langevin approach for the relativistic viscous hydrodynamics. For the POWLANG model two choices for the transport coefficients are included, one considering hard-thermal-loop (HTL) calculations and one considering lattice-QCD as mentioned in section 2.1.1.

A structure with a maximum at $p_T \approx 2.5 \text{ GeV}/c$ is seen in both models followed by a moderate suppression at higher transverse momenta. This suppression is disfavoured by the data which shows a flat trend for $p_T > 4 \text{ GeV}/c$. A small suppression is not excluded, but data disfavours a suppression larger then 10-15% in the 3-12 GeV/c interval. Two of the models including a Quark-Gluon Plasma for proton-lead, namely POWLANG HTL and Duke predict a suppression of 20-30%.

To see if the trend in data is related to the multiplicity of the collision, and thus related to the number of participants, a measurement in ‘centrality’ classes was done. For these measurement the Q_{pPb} was defined as:

$$Q_{pPb} = \frac{(d^2 N^{\text{prompt D}}/dp_T dy)_{pPb}^{\text{cent}}}{\langle T_{pPb} \rangle \times (d^2 \sigma_{pp}^{\text{prompt D}}/dp_T dy)}. \quad (6.1)$$

The choice for Q_{pPb} rather than naming it R_{pPb}^{cent} is made as the link between the centrality classes and the impact parameter is less clear in p–Pb collisions. The centrality classes are defined experimentally in the same way, with 0-10% the 10% collisions with the highest multiplicity available, but the difference in multiplicity is

partially due to fluctuations in the initial state. The average nuclear overlap function T_{pPb} in proton-lead collisions is estimated with a hybrid approach described in [90] which is based on the assumption that the charged-particle distribution measured at mid-rapidity scales with the number of participant nucleons.

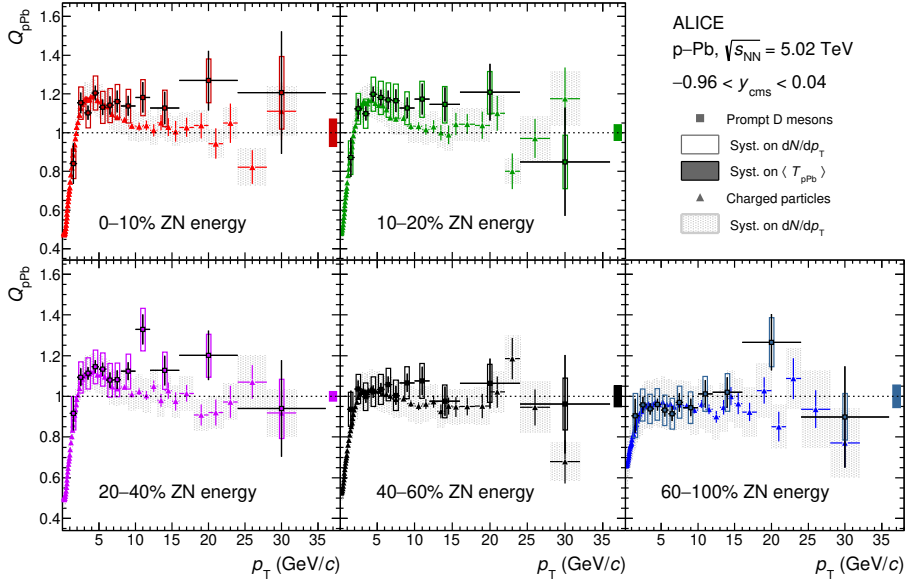


Figure 6.17: Nuclear modification factors of prompt D meson as a function of p_T in 0–10%, 10–20%, 20–40%, 40–60%, and 60–100% centrality classes compared to charged particles. The vertical error bars represent the statistical uncertainties while the empty boxes and the full boxes represent the systematic uncertainties for prompt D mesons and for charged particles, respectively. The colour-filled boxes at $Q_{pPb} = 1$ represent the normalisation uncertainties.

As one can see in figure 6.17 there is some hint of centrality dependence in the central values going from high multiplicity to low multiplicity, which is in agreement with the trend observed for charged particles. The uncertainty bars in figure 6.17 show that in most of the transverse momentum range the dominant uncertainty is the systematical uncertainty.

To further understand the difference between the centralities further a new observable was proposed, the Q_{CP} . This observable is defined as,

$$Q_{CP} = \frac{(d^2 N^{\text{prompt D}}/dp_T dy)_{pPb}^{\text{cent}}/\langle T_{pPb} \rangle^{\text{cent}}}{(d^2 N^{\text{prompt D}}/dp_T dy)_{pPb}^{60-100}/\langle T_{pPb} \rangle^{60-100}}. \quad (6.2)$$

Therefore the Q_{CP} is independent of the proton-proton results and does not include the uncertainties on the track reconstruction, selection criteria and PID uncertainties, which cancel in the ratio.

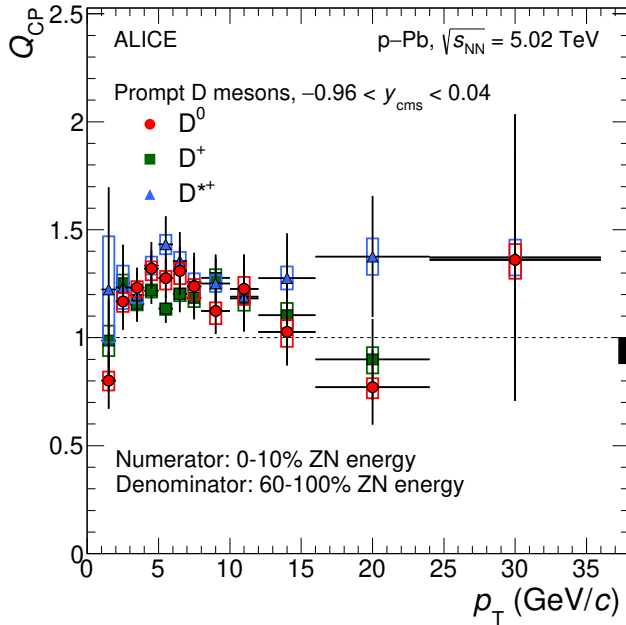


Figure 6.18: Separate D-meson Q_{CP} , obtained using 0–10% as numerator and 60–100% as denominator. The vertical error bar represent the statistical and the empty boxes represent the systematic uncertainties. The colour-filled box at $Q_{CP} = 1$ represent the normalisation uncertainties.

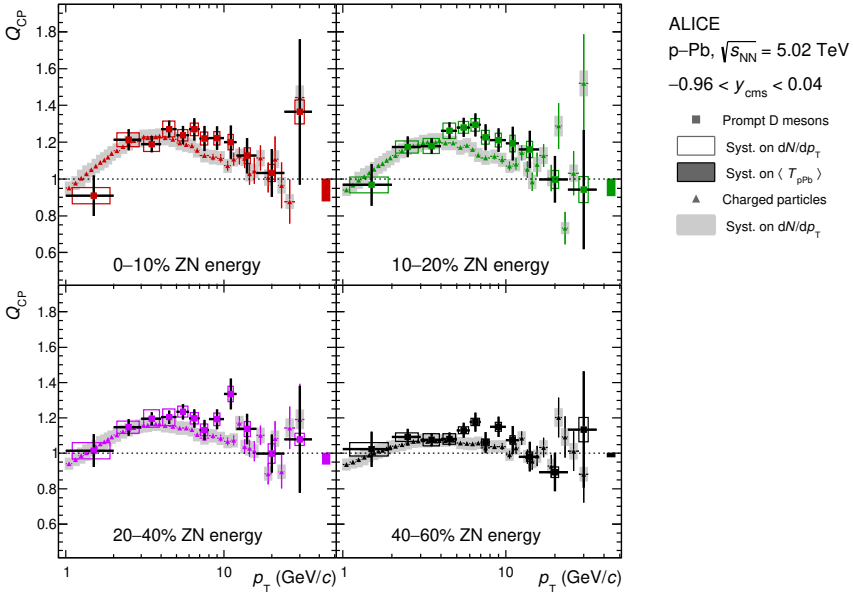


Figure 6.19: Average D-meson and charge particles Q_{CP} , obtained using 0–10%, 10–20%, 20–40% and 40–60% as numerators and 60–100% as denominator. The vertical error bars represent the statistical and the empty boxes represent the systematic uncertainties. The colour-filled boxes at $Q_{CP} = 1$ represent the normalisation uncertainties.

The Q_{CP} results are compared to those of charged particles in figure 6.19. Both particles show a similar trend, which are consistent with the Q_{pPb} results. When the results compared to all charged produced particles of to the same transverse momentum, there is an increase in the Q_{CP} in lowest p_T range available for the D-mesons, $1 < p_T < 5 \text{ GeV}/c$ up to about 1.3 for most central collisions.

Above $5 \text{ GeV}/c$ the values are decreasing to around 1 on average. Due to the smaller uncertainties the deviation seen at the 20-40% centrality classes divided by the 60-100% is the most significant of figure 6.19. Here it reaches a 3σ deviation from 1 between 3-7 GeV/c . This however does not imply that the effect is the strongest in this centrality class, the uncertainty due to the $\langle T_{pPb} \rangle$ factor decreases for more peripheral events.

Simply comparing the size of the deviation the ratios with the 0-10% and 10-20% as a numerator have a stronger effect at the same p_T -interval. However, due to the higher uncertainties these only amount to respectively 1.5σ and 2σ . While there were no theoretical predictions available for this observable at the time of completion of these measurements for the paper, it could be possible for radial flow that arises from a hydrodynamical evolution to modify the hadronisation dynamics of heavy quarks such that it would show an enhancement at intermediate p_T [78].

Discussion and Outlook

In the previous two sections the results obtained for 13 TeV pp and 5.02 TeV p–Pb collisions were reported with respect to earlier results and results of different energies. These results help to test the theoretical predictions for proton-proton and proton-lead collisions. These results showed agreement between theory and experiment at all available energies in proton-proton collisions and in contrast to the models there is only a very mild p_T dependence of R_{pPB} at $p_T > 3\text{GeV}/c$ in p–Pb collisions. In this chapter our results will be combined with some other results of ALICE to point out possible tension between possible theoretical models with the data. Finally an outlook towards future measurements is shown.

7.1 Outlook on the 13 TeV proton-proton results

As we have discussed in chapter 5 the proton-proton results have been extracted using only a small part of the measurement, containing 2 data-taking periods of 2016. The final complete sample of 13 TeV proton-proton collisions including 2016, 2017 and 2018 data taking periods is expected to have approximately 2 billion collisions, about a factor 10 more. Such a large sample reduces the effect of statistical fluctuations strongly, allowing us to measure D-mesons in run 2 of the LHC up to such precision that systematic effects form the dominant uncertainty. With double the statistics a more precise measurement than for 5 TeV proton-proton collisions is expected, which opens the possibility to do more differential measurements.

The measured values are consistently at the upper limit of the theoretical uncertainty, thus further measurements could be used to reduce uncertainties. Comparing the samples at 5 and 13 TeV, as was done in figure 5.16, shows some deviations from the central values. While no significant deviations are seen, the full sample would minimize the statistical uncertainties and allow to possibly further constrain gluonic parton density functions.

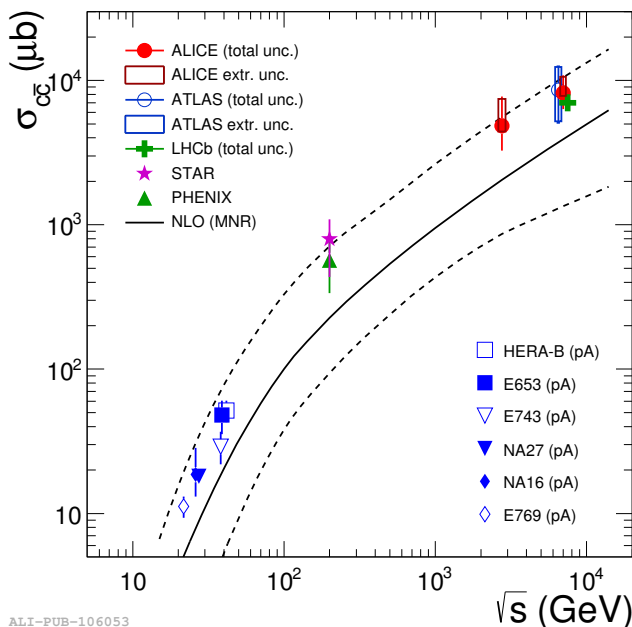


Figure 7.1: Total inclusive charm production cross section in proton-proton and proton-nucleon collisions as a function of the energy of the collision system [87, 91, 92, 93, 94, 95, 96] Data from proton-nucleon collisions were scaled with the nuclear number $1/A$. Results from NLO pQCD calculations (MNR [83]) are shown as solid lines and their uncertainties with dashed lines.

Combining D^{*+} , D^0 and D^+ measurements allows us to extract a charm cross-section value as is shown for other energies in figure 7.1. Inclusion of the 5.02 and 13 TeV results with the improved precision might help them reduce the uncertainties. This would make it even more interesting for theoreticians to try to calculate the next order correction and see if it moves the values towards the data.

7.2 Discussion on the p–Pb results at 5.02 TeV

If the comparison of the R_{pPb} with different models is studied as done in figure 6.16, chapter 6, there are hints of a preference for those models not including some quark gluon plasma like-effect in proton-lead.

At first look these models seem to disagree with the positive elliptic flow measurements from ALICE, ATLAS and CMS in high multiplicity proton-lead and PHENIX and STAR in high-multiplicity deuteron-gold collisions. Elliptic is often linked to a hydrodynamical evolution of some type of medium. However it is unclear whether the elliptic flow measured in p–Pb and even pp collisions are related to some type of hydrodynamical behaviour, and even less clear whether it implies the existence of a QGP. In these collisions the positive flow coefficients are most often linked to strong fluctuations in the initial state. These results are found in the highest multiplicity classes for these collisions. Alternative attempts for explanation of the elliptic flow use colour glass condensate models or final state colour exchange [97][98]. As was discussed in chapter 2.2 heavy flavour results could help to identify the source of the elliptic flow, or at least to constrain the models.

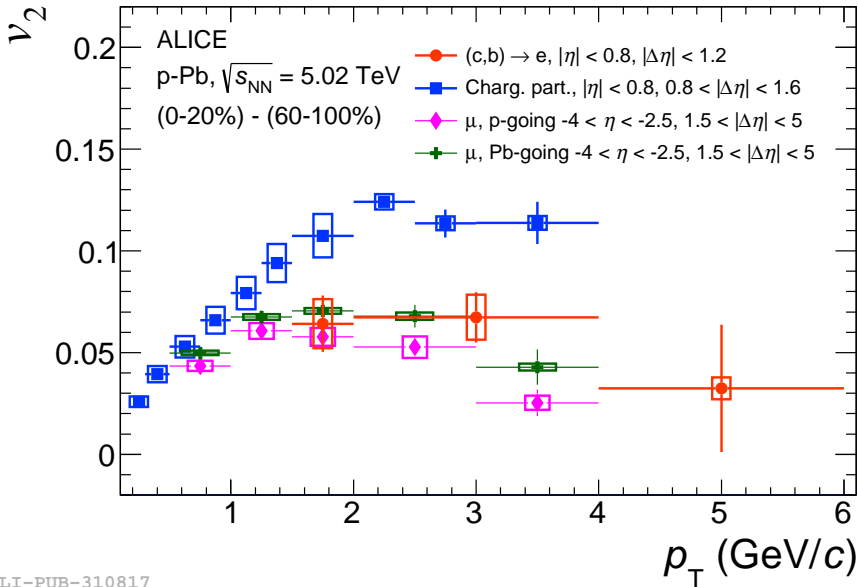


Figure 7.2: Elliptic flow of heavy flavour decay electrons compared to that of charged particles[99] and muons[100]. Statistical and systematic uncertainties are shown as bars and boxes, respectively. Figure from [101].

The heavy-flavour decay electron measurement shows a non-zero v_2 , in figure 7.2, between 1.5 – 4 GeV/c this has a significance higher than 5σ from [101]. The muon results shown in this figure are measured at forward rapidity and these results are dominated by heavy flavour muons for muon p_T above 2 GeV/c. Even above this threshold the comparison with these results is not straightforward as the heavy flavour production is influenced by different cold nuclear matter effects at different rapidities [100]. The elliptic flow of heavy flavour electrons is similar in strength to that of the charged hadrons, when taking into account the different transverse moment ranges of the two.

To summarise: the elliptic flow of heavy flavour confirms earlier observations in the light flavour sector of collective behaviour in p-Pb, while the relatively mild modification in the R_{pPb} seems to disfavour models including a QGP. The centrality dependence of the Q_{CP} does not help to clarify this.

7.3 Outlook on heavy flavour measurements

In the previous two sections the proton-lead and proton-proton results were discussed with respect to other measurements of heavy flavour probes in small systems. In this section we will instead try to look at the future of the field: which improvements are expected next?

The proton-proton results will improve by combining the available large statistics, as was discussed in section 7.1. This should reduce our uncertainties significantly, increase the transverse momentum range to higher momenta and could make a finer transverse momentum binning possible. However the experimental results for the full charm cross-section, such as shown in in figure 7.1 are very dependent on the low momentum results. As the distribution of heavy flavour particle decreases rapidly at higher transverse momentum the total cross-section is dominated by the lowest transverse momenta results. Thus more precise measurements at lower transverse momenta could improve the total charm cross-section uncertainty significantly.

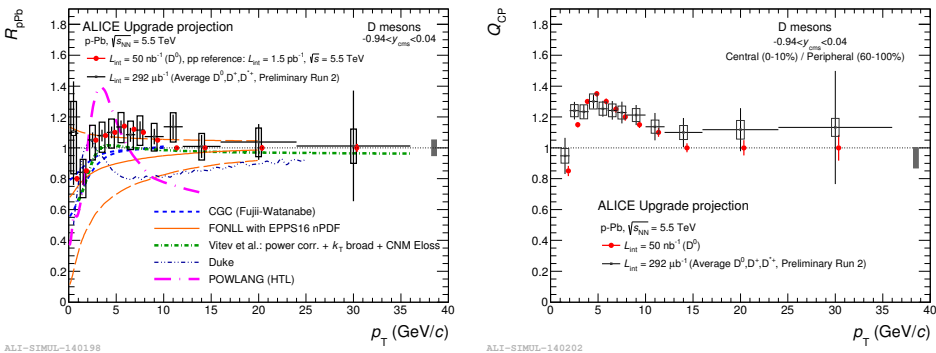


Figure 7.3: Modification factors R_{pPb} (left) and Q_{CP} (right) as a function of p_T for p-Pb collisions. In black the old preliminary results are shown while in red the projections for future results including measurements from run 3 and 4. (Figure as reported by ALICE at the HLLHC physics workshop 2017)

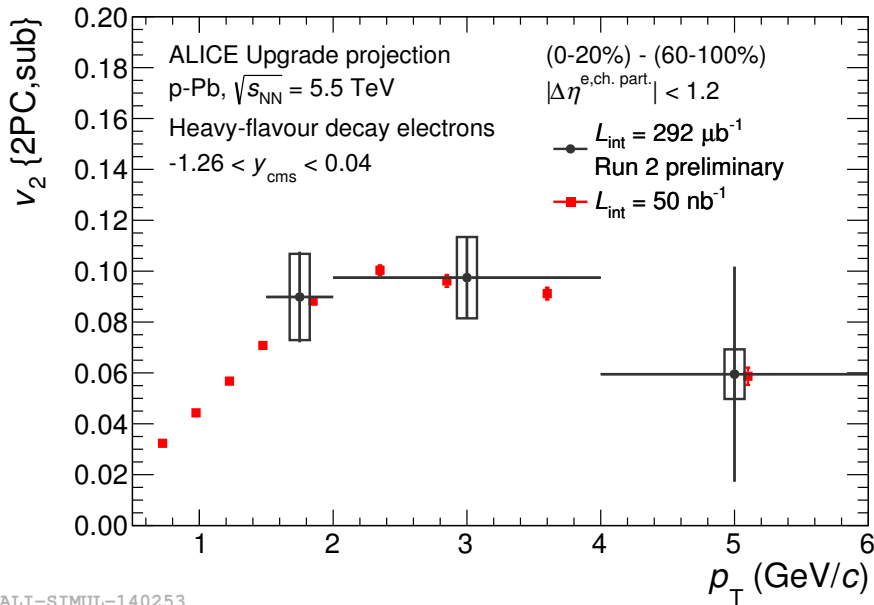


Figure 7.4: Elliptic flow of heavy flavour decay electrons expected in red compared to the recent results in black. Figure from [102]

An improvement in the measuring capabilities at lowest transverse momenta is not only very interesting for the charm measurement. The lowest transverse momentum range is also the range in which the cold nuclear matter models for p-Pb differ the most (see figure 7.3). In addition to those measurements the improvements necessary for the increased precision of the cross-section will enable us to measure the elliptic flow more precisely (see figure 7.4). Such precise measurements are expected to be possible in run 3 of the LHC, at 14 TeV in pp and at 5.5 TeV in proton-lead collisions. ALICE is using long shut down 2 to upgrade its inner tracking system. This updated system will be able to measure particles to significantly lower transverse momenta. On top of that the precision measurements will make it possible to reconstruct secondary vertices to such a precision that ALICE will be able to measure and identify beauty decays. This would us to abandon the current theoretically based feed-down corrections and instead identify the feed-down fraction with the data-driven method with the necessary precision.

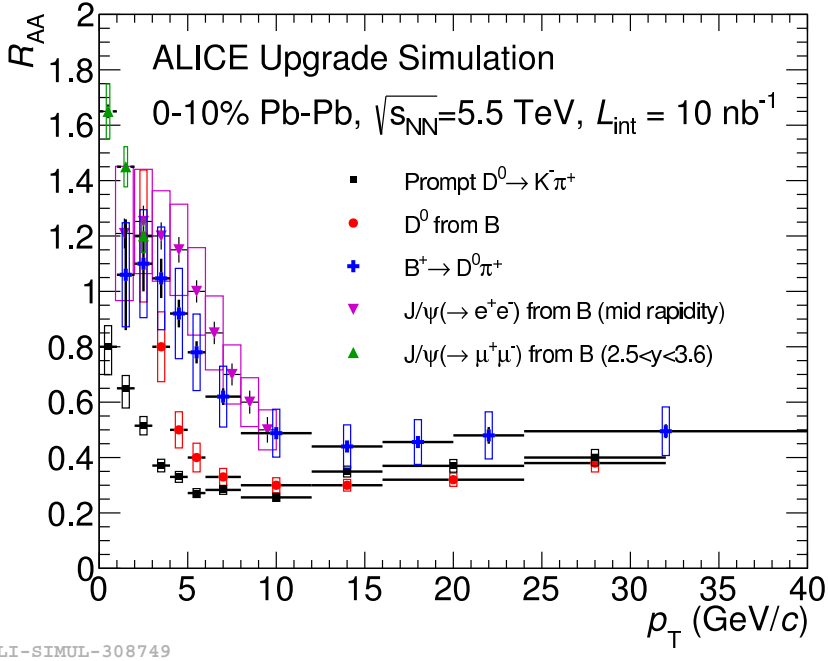


Figure 7.5: R_{AA} vs p_T of D^0 and B mesons using different decays: $B^+ \rightarrow D^0\pi^+$, prompt and non-prompt D^0 and non-prompt $J/\psi \rightarrow e^+e^-$ at mid rapidity and non-prompt $J/\psi \rightarrow \mu^+\mu^-$ at forward rapidity. Simulation of Pb-Pb collisions at 5.5 TeV for Run3+4 (10 nb^{-1}). Figure from [103]

In figure 7.5 simulations for the effect of the upgrade on the nuclear modification factor on D^0 measurements are shown in combination with examples of beauty measurement that would be possible with the upgrade.

Appendix A:
Invariant-mass-difference figures
in pp collisions

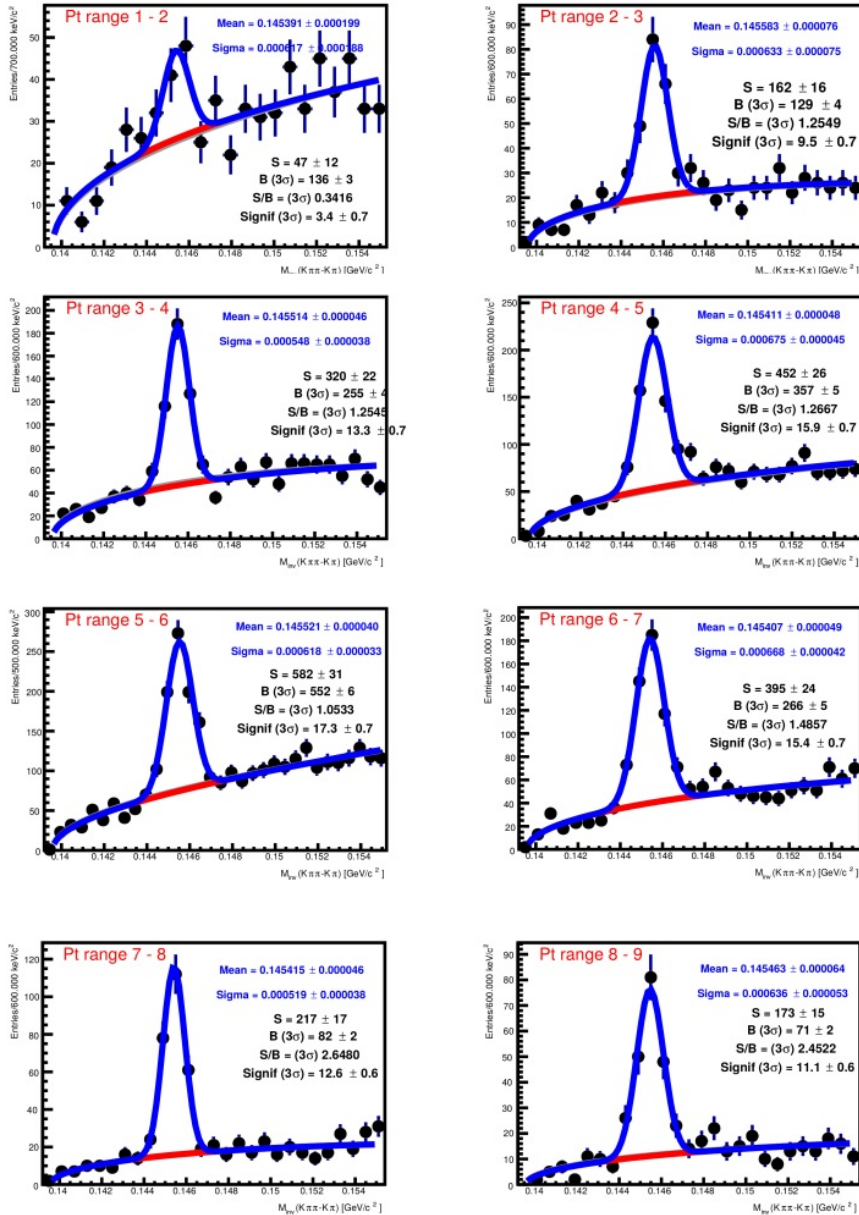


Figure 6: Invariant-mass-difference distributions of D^{*+} candidates and charge conjugates in the 1 to 9 $\text{GeV}/c p_T$ interval as an example for a sample of pp collisions at $\sqrt{s} = 13$ TeV. The blue curve shows the fit function of a combined signal and background function, while the red line represents the background fit function.

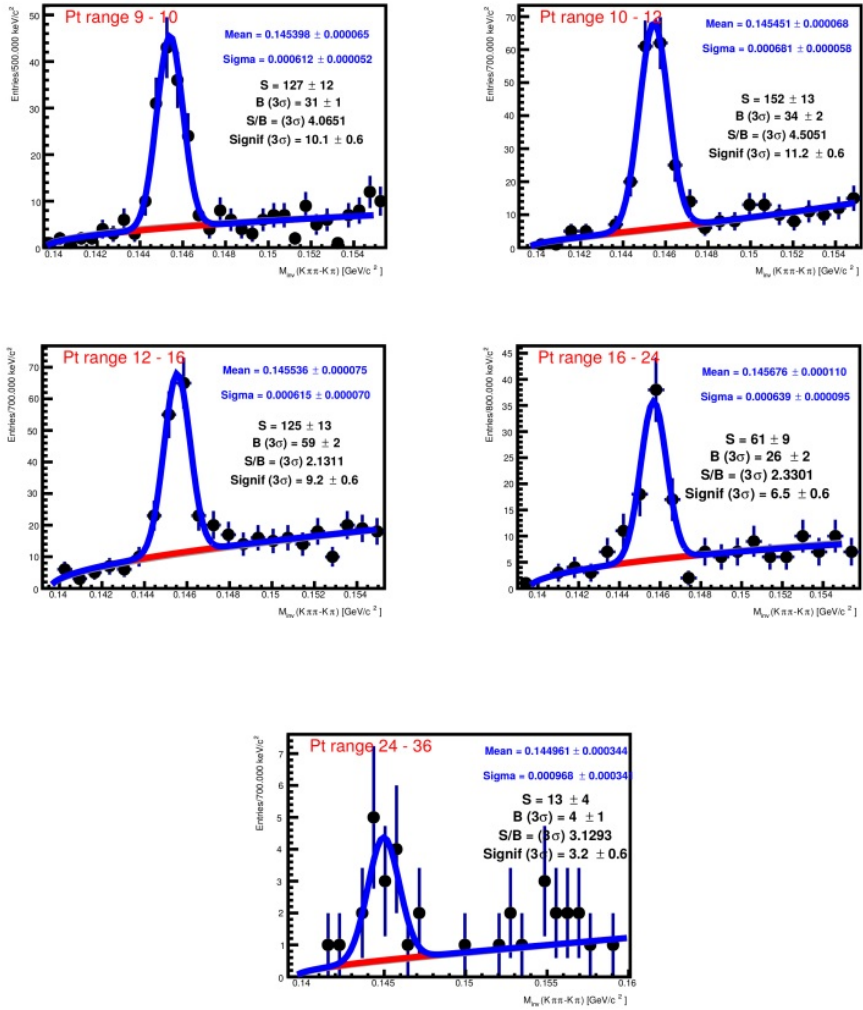


Figure 7: Invariant-mass-difference distributions of D^{*+} candidates and charge conjugates in the 9 to 36 GeV/c p_T interval as an example for a sample of pp collisions at $\sqrt{s} = 13$ TeV. The blue curve shows the fit function of a combined signal and background function, while the red line represents the background fit function.

Appendix B: Systematic uncertainties in pp collisions at 13 TeV

p_T GeV/c	1-2	2-3	3-4	4-5	5-6	6-7	7-8	8-9	9-10	10-12	12-16	16-24	24-36
FD up (%)	9	4	4	3	2	2	2	2	2	2	3	3	2
FD down (%)	9	4	4	3	2	3	3	3	3	3	3	3	2
Sel. crit. (%)	11	5	3	3	3	3	3	3	3	3	3	3	3
Raw Yield (%)	9	7	5	5	3	3	3	2	2	2	3	3	21
p_T -shape (%)	4	0	0	0	0	0	0	0	0	0	0	0	0
PID (%)	0	0	0	0	0	0	0	0	0	0	0	0	0
Tracking (%)	5.5	5.5	6	6	6.5	6.5	6.5	6.5	6.5	6.5	6.5	6.5	7
Total (%)	18%	11%	9%	9%	8%	8%	8%	8%	8%	8%	8%	8%	22%

Table A.1 : Systematic uncertainties extracted for the preliminary studies of the D^{*+} in 13 TeV

Appendix C: Topological selection criteria in p–Pb collisions

Table B.2: Topological selection criteria for D^{*+} used for analysis in p-Pb collisions, where hw stands for Half-width.

p_T GeV/c	1-2	2-3	3-4	4-5	5-6	6-7	7-8	8-12	12-16	16-24	24-36
Inv Mass D^0 (GeV/c ²)	0.03	0.032	0.032	0.032	0.036	0.036	0.036	0.05	0.094	.7	.7
DCA (cm)	0.030	0.03	0.024	0.031	0.04	0.08	0.12	0.105	0.1	.15	.15
$\cos \theta^*$	0.8	0.8	0.8	0.9	1.0	1.0	1.0	1.0	1.0	1.0	1.0
$p_T K$ (GeV/c)	0.5	1.0	1.0	1.	1.0	1.0	1.0	1.0	1.0	0.3	0.3
$p_T \pi$ (GeV/c)	0.5	1.0	1.0	1.	1.0	1.0	1.0	1.0	1.0	0.3	0.3
Imp. par. $d0_K$ (cm)	0.1	0.1	0.1	0.1	0.09	0.1	0.1	0.1	0.2	0.5	.5
Imp. par. $d0_\pi$ (cm)	0.1	0.1	0.1	0.1	0.09	0.1	0.1	0.1	0.2	0.5	.5
$d0_K \times d0_\pi$ (10 ⁻³ cm ²)	-0.36	-0.25	-0.13	-0.038	0.044	8	0.3	10	10	10	10
$\cos \theta_{point}$	0.865	0.9	0.87	0.86	0.83	0.76	0.76	0.68	0.6	0.1	0.6
Inv. M. hw D^{*+} (GeV/c ²)	0.15	0.3	0.15	0.15	0.15	0.15	0.15	0.15	0.2	0.3	0.3
Hw $M_{K\pi\pi} - M_{D^0}$ (GeV/c ²)	0.03	0.15	0.03	0.03	0.03	0.03	0.03	0.03	.1	0.1	0.1
p_T min soft π (GeV/c)	0.05	0.05	0.05	0.05	0.1	0.2	0.3	0.3	.05	0.05	0.05
p_T max soft π (GeV/c)	.5	0.5	0.5	10	10	100	100	100	100	100	10000
Norm Decay Length_XY	4.	4.	3.5	3	2.5	1.5	1	0	0	0	0

Appendix D:
Invariant-mass-difference figures
in p–Pb collisions

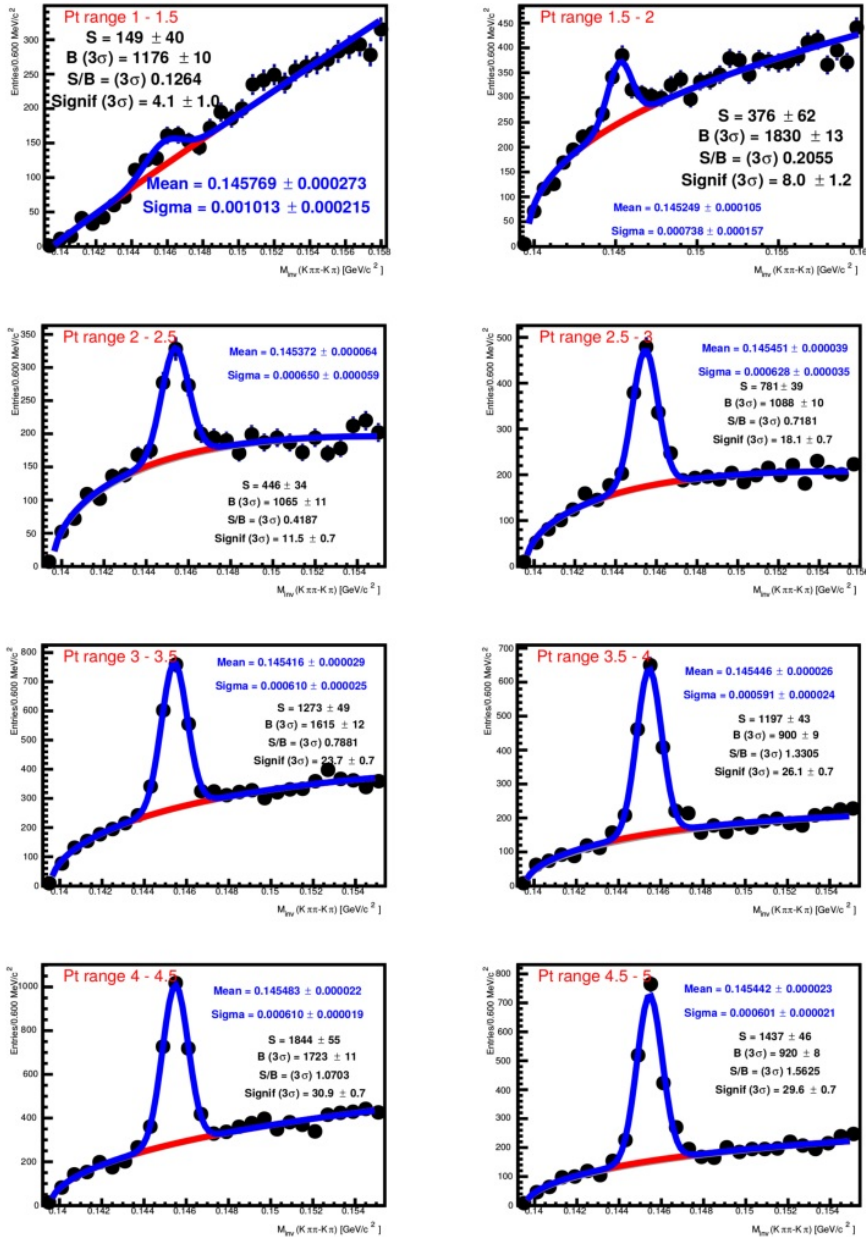


Figure C.8: Invariant-mass-difference distributions of D^{*+} candidates and charge conjugates in the 1 to 5 GeV/c p_T interval as an example for a sample of p–Pb collisions at $\sqrt{s} = 5.02$ TeV. The blue curve shows the fit function of a combined signal and background function, while the red line represents the background fit function.

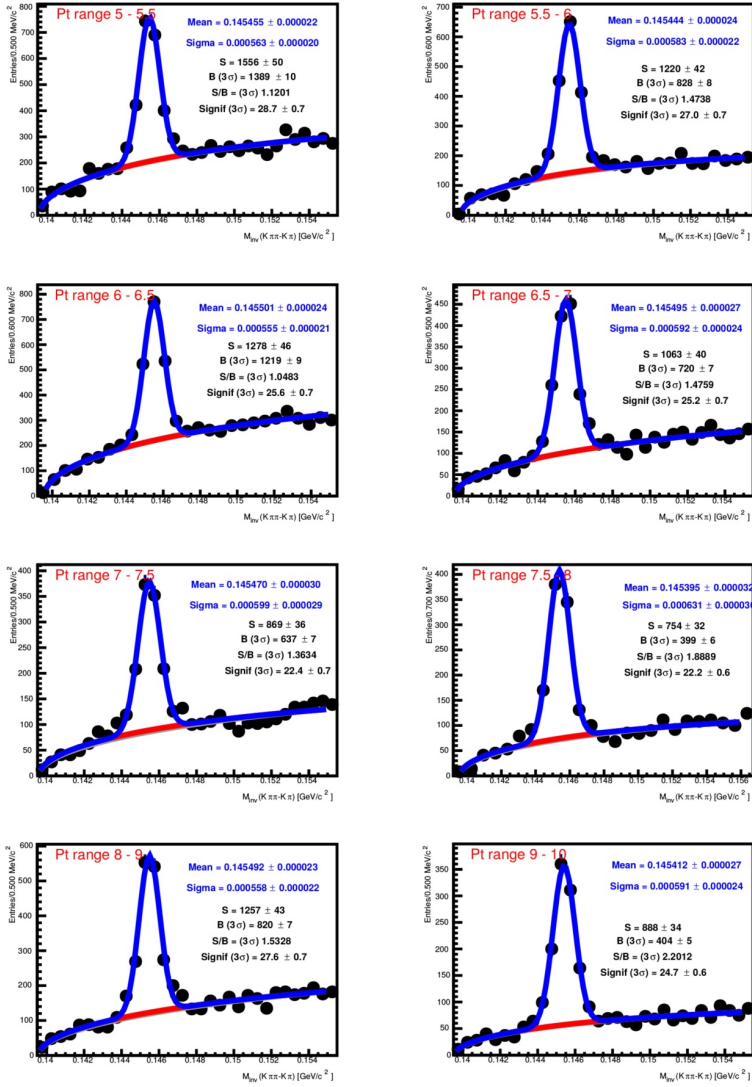


Figure C.9: Invariant-mass-difference distributions of D^{*+} candidates and charge conjugates in the 5 to 10 GeV/c p_T interval as an example for a sample of p–Pb collisions at $\sqrt{s} = 5.02$ TeV. The blue curve shows the fit function of a combined signal and background function, while the red line represents the background fit function.

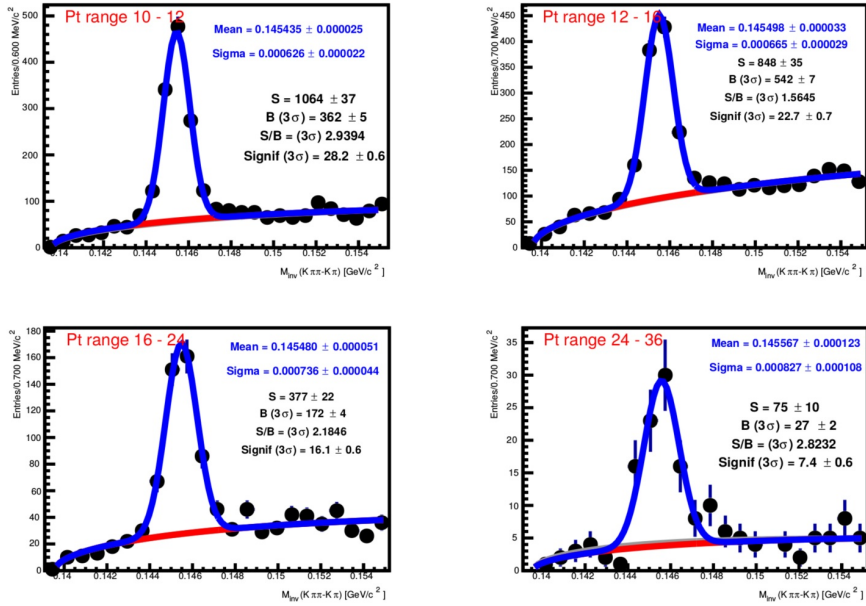


Figure C.10: Invariant-mass-difference distributions of D^{*+} candidates and charge conjugates in the 10 to 36 GeV/c p_T interval as an example for a sample of p–Pb collisions at $\sqrt{s} = 5.02$ TeV. The blue curve shows the fit function of a combined signal and background function, while the red line represents the background fit function.

Bibliography

- [1] Perkins, D. H., *Introduction to High Energy Physics*, 4th ed., Cambridge University Press, 2000, DOI: 10.1017/CB09780511809040.
- [2] Gell-Mann, M., “A Schematic Model of Baryons and Mesons”, *Phys. Lett.* Vol. 8, 1964, pp. 214–215, DOI: 10.1016/S0031-9163(64)92001-3.
- [3] Zweig, G., *An SU_3 model for strong interaction symmetry and its breaking; Version 1*, tech. rep. CERN-TH-401, Geneva: CERN, 1964, URL: <https://cds.cern.ch/record/352337>.
- [4] Bjørken, B. & Glashow, S., “Elementary particles and $SU(4)$ ”, *Physics Letters*, vol. 11, no. 3, 1964, pp. 255–257, DOI: 10.1016/0031-9163(64)90433-0, URL: <http://www.sciencedirect.com/science/article/pii/0031916364904330>.
- [5] Griffiths, D. J., *Introduction to elementary particles; 2nd rev. version*, Physics textbook, New York, NY: Wiley, 2008, URL: <https://cds.cern.ch/record/111880>.
- [6] Aaij, R. et al., “Observation of $J/\psi p$ Resonances Consistent with Pentaquark States in $\Lambda_b^0 \rightarrow J/\psi K^- p$ Decays”, *Phys. Rev. Lett.* Vol. 115, 2015, p. 072001, DOI: 10.1103/PhysRevLett.115.072001, arXiv: 1507.03414 [hep-ex].
- [7] Gross, D. J. & Wilczek, F., “Asymptotically Free Gauge Theories. I”, *Phys. Rev. D*, vol. 8, 10 1973, pp. 3633–3652, DOI: 10.1103/PhysRevD.8.3633, URL: <https://link.aps.org/doi/10.1103/PhysRevD.8.3633>.
- [8] David Politzer, H., “Asymptotic freedom: An approach to strong interactions”, *Physics Reports*, vol. 14, Nov. 1974, pp. 129–180, DOI: 10.1016/0370-1573(74)90014-3.
- [9] Khachatryan, V. et al., “Measurement of the inclusive 3-jet production differential cross section in proton–proton collisions at 7 TeV and determination of the strong coupling constant in the TeV range”, *Eur. Phys. J.* Vol. C75, no. 5, 2015, p. 186, DOI: 10.1140/epjc/s10052-015-3376-y, arXiv: 1412.1633 [hep-ex].
- [10] Luscher, M., “Lattice QCD: From quark confinement to asymptotic freedom”, *Annales Henri Poincare*, vol. 4, 2003, S197–S210, DOI: 10.1007/s00023-003-0916-z, arXiv: hep-ph/0211220 [hep-ph].
- [11] Bhalerao, R. S., “Relativistic heavy-ion collisions”, no. TIFR-TH-14-11, 2014, Comments: Updated version of the lectures given at the First Asia-Europe-Pacific School of High-Energy Physics, Fukuoka, Japan, 14-27 October 2012.

- Published as a CERN Yellow Report (CERN-2014-001) and KEK report (KEK-Proceedings-2013-8), K. Kawagoe and M. Mulders (eds.), 2014, p. 219. Total 21 pages, 219–239. 21 p, URL: <http://cds.cern.ch/record/1695331>.
- [12] al., A. A. et, “The effective QCD phase diagram and the critical end point”, *Nuclear Physics B*, vol. 897, 2015, pp. 77–86, DOI: 10.1016/j.nuclphysb.2015.05.014, URL: <http://www.sciencedirect.com/science/article/pii/S0550321315001741>.
- [13] Baldo, M., Buballa, M., Burgio, G., Neumann, F., Oertel, M. & Schulze, H.-J., “Neutron stars and the transition to color superconducting quark matter”, *Physics Letters B*, vol. 562, no. 3, 2003, pp. 153–160, DOI: 10.1016/S0370-2693(03)00556-2, URL: <http://www.sciencedirect.com/science/article/pii/S0370269303005562>.
- [14] Shen, C. & Heinz, U., “The road to precision: Extraction of the specific shear viscosity of the quark-gluon plasma”, *Nucl. Phys. News*, vol. 25, no. 2, 2015, pp. 6–11, DOI: 10.1080/10619127.2015.1006502, arXiv: 1507.01558 [nucl-th].
- [15] Busza, W., Rajagopal, K. & Schee, W. van der, “Heavy Ion Collisions: The Big Picture, and the Big Questions”, *Ann. Rev. Nucl. Part. Sci.* Vol. 68, 2018, pp. 339–376, DOI: 10.1146/annurev-nucl-101917-020852, arXiv: 1802.04801 [hep-ph].
- [16] Iancu, E., “QCD in heavy ion collisions”, in: *Proceedings, 2011 European School of High-Energy Physics (ESHEP 2011): Cheile Gradistei, Romania, September 7-20, 2011*, 2014, pp. 197–266, DOI: 10.5170/CERN-2014-003.197, arXiv: 1205.0579 [hep-ph].
- [17] Pasechnik, R. & Šumbera, M., “Phenomenological Review on Quark–Gluon Plasma: Concepts vs. Observations”, *Universe*, vol. 3, no. 1, 2017, p. 7, DOI: 10.3390/universe3010007, arXiv: 1611.01533 [hep-ph].
- [18] Adam, J. et al., “Anisotropic flow of charged particles in Pb-Pb collisions at $\sqrt{s_{NN}} = 5.02$ TeV”, *Phys. Rev. Lett.* Vol. 116, no. 13, 2016, p. 132302, DOI: 10.1103/PhysRevLett.116.132302, arXiv: 1602.01119 [nucl-ex].
- [19] Aamodt, K. et al., “Particle-Yield Modification in Jetlike Azimuthal Dihadron Correlations in Pb-Pb Collisions at $\sqrt{s_{NN}} = 2.76$ TeV”, *Phys. Rev. Lett.* Vol. 108, 9 2012, p. 092301, DOI: 10.1103/PhysRevLett.108.092301, URL: <https://link.aps.org/doi/10.1103/PhysRevLett.108.092301>.
- [20] Andronic, A. et al., “Heavy-flavour and quarkonium production in the LHC era: from proton-proton to heavy-ion collisions”, *Eur. Phys. J.* Vol. C76, no. 3, 2016, p. 107, DOI: 10.1140/epjc/s10052-015-3819-5, arXiv: 1506.03981 [nucl-ex].
- [21] Liu, F.-M. & Liu, S.-X., “Quark-gluon plasma formation time and direct photons from heavy ion collisions”, *Phys. Rev.* Vol. C89, no. 3, 2014, p. 034906, DOI: 10.1103/PhysRevC.89.034906, arXiv: 1212.6587 [nucl-th].
- [22] Levai, P. & Vogt, R., “Thermal charm production by massive gluons and quarks”, *Phys. Rev.* Vol. C56, 1997, pp. 2707–2717.
- [23] Rapp, R. & Hees, H. van, “Heavy Quarks in the Quark-Gluon Plasma”, in: *Quark-gluon plasma 4*, 2010, pp. 111–206.

- [24] Averbek, R., “Heavy-flavor production in heavy-ion collisions and implications for the properties of hot QCD matter”, *Progress in Particle and Nuclear Physics*, vol. 70, May 2013, pp. 159–209.
- [25] Uphoff, J., Fochler, O., Xu, Z. & Greiner, C., “Elliptic Flow and Energy Loss of Heavy Quarks in Ultra-Relativistic heavy Ion Collisions”, *Phys.Rev.* Vol. C84, 2011, p. 024908, DOI: 10.1103/PhysRevC.84.024908, arXiv: 1104.2295 [hep-ph].
- [26] Svetitsky, B., “Diffusion of charmed quarks in the quark-gluon plasma”, *Phys. Rev. D*, vol. 37, 9 1988, pp. 2484–2491, DOI: 10.1103/PhysRevD.37.2484, URL: <https://link.aps.org/doi/10.1103/PhysRevD.37.2484>.
- [27] Das, S. K., Scardina, F., Plumari, S. & Greco, V., “Heavy-flavor in-medium momentum evolution: Langevin versus Boltzmann approach”, *Phys. Rev.* Vol. C90, 2014, p. 044901, DOI: 10.1103/PhysRevC.90.044901, arXiv: 1312.6857 [nucl-th].
- [28] He, M., Fries, R. J. & Rapp, R., “Heavy-Quark Diffusion and Hadronization in Quark-Gluon Plasma”, *Phys. Rev.* Vol. C86, 2012, p. 014903, DOI: 10.1103/PhysRevC.86.014903, arXiv: 1106.6006 [nucl-th].
- [29] Gossiaux, P. B., Vogel, S., Hees, H. van, Aichelin, J., Rapp, R., He, M. & Bluhm, M., “The Influence of bulk evolution models on heavy-quark phenomenology”, *Submitted to: Phys.rev. C*, 2011, arXiv: 1102.1114 [hep-ph].
- [30] Su, N., “A brief overview of hard-thermal-loop perturbation theory”, *Commun. Theor. Phys.* Vol. 57, 2012, p. 409, DOI: 10.1088/0253-6102/57/3/12, arXiv: 1204.0260 [hep-ph].
- [31] Dokshitzer, Y. L. & Kharzeev, D., “Heavy quark colorimetry of QCD matter”, *Phys.Lett.* Vol. B519, 2001, pp. 199–206, DOI: 10.1016/S0370-2693(01)01130-3, arXiv: hep-ph/0106202 [hep-ph].
- [32] Djordjevic, M. & Gyulassy, M., “Heavy quark radiative energy loss in QCD matter”, *Nucl.Phys.* Vol. A733, 2004, pp. 265–298, DOI: 10.1016/j.nuclphysa.2003.12.020, arXiv: nucl-th/0310076 [nucl-th].
- [33] Armesto, N., Salgado, C. A. & Wiedemann, U. A., “Medium induced gluon radiation off massive quarks fills the dead cone”, *Phys.Rev.* Vol. D69, 2004, p. 114003, DOI: 10.1103/PhysRevD.69.114003, arXiv: hep-ph/0312106 [hep-ph].
- [34] Beraudo, A., De Pace, A., Monteno, M., Nardi, M. & Prino, F., “Heavy flavors in heavy-ion collisions: quenching, flow and correlations”, *Eur. Phys. J.* Vol. C75, no. 3, 2015, p. 121, DOI: 10.1140/epjc/s10052-015-3336-6, arXiv: 1410.6082 [hep-ph].
- [35] Song, T., Berrehrah, H., Cabrera, D., Cassing, W. & Bratkovskaya, E., “Charm production in Pb + Pb collisions at energies available at the CERN Large Hadron Collider”, *Phys. Rev.* Vol. C93, no. 3, 2016, p. 034906, DOI: 10.1103/PhysRevC.93.034906, arXiv: 1512.00891 [nucl-th].
- [36] Cao, S., Luo, T., Qin, G.-Y. & Wang, X.-N., “Heavy and light flavor jet quenching at RHIC and LHC energies”, 2017, arXiv: 1703.00822 [nucl-th].
- [37] He, M., Fries, R. J. & Rapp, R., “Heavy Flavor at the Large Hadron Collider in a Strong Coupling Approach”, *Phys.Lett.* Vol. B735, 2014, pp. 445–450, DOI: 10.1016/j.physletb.2014.05.050, arXiv: 1401.3817 [nucl-th].

- [38] Nahrgang, M., Aichelin, J., Gossiaux, P. B. & Werner, K., “Influence of hadronic bound states above T_c on heavy-quark observables in Pb + Pb collisions at the CERN Large Hadron Collider”, *Phys.Rev.* Vol. C89, no. 1, 2014, p. 014905, DOI: 10.1103/PhysRevC.89.014905, arXiv: 1305.6544 [hep-ph].
- [39] Acharya, S. et al., “Measurement of D^0 , D^+ , D^{*+} and D_s^+ production in Pb-Pb collisions at $\sqrt{s_{NN}} = 5.02$ TeV”, *JHEP*, vol. 10, 2018, p. 174, DOI: 10.1007/JHEP10(2018)174, arXiv: 1804.09083 [nucl-ex].
- [40] Djordjevic, M. & Djordjevic, M., “Predictions of heavy-flavor suppression at 5.1 TeV Pb+Pb collisions at the CERN Large Hadron Collider”, *Phys. Rev.* Vol. C92, no. 2, 2015, p. 024918, DOI: 10.1103/PhysRevC.92.024918, arXiv: 1505.04316 [nucl-th].
- [41] Adam, J. et al., “Centrality dependence of the nuclear modification factor of charged pions, kaons, and protons in Pb-Pb collisions at $\sqrt{s_{NN}} = 2.76$ TeV”, 2015, arXiv: 1506.07287 [nucl-ex].
- [42] Djordjevic, M., “Heavy flavor puzzle at LHC: a serendipitous interplay of jet suppression and fragmentation”, *Phys.Rev.Lett.* Vol. 112, no. 4, 2014, p. 042302, DOI: 10.1103/PhysRevLett.112.042302, arXiv: 1307.4702 [nucl-th].
- [43] Greco, V., Ko, C. M. & Levai, P., “Parton coalescence at RHIC”, *Phys. Rev.* Vol. C68, 2003, p. 034904, DOI: 10.1103/PhysRevC.68.034904, arXiv: nucl-th/0305024 [nucl-th].
- [44] Xu, Y., Cao, S., Qin, G.-Y., Ke, W., Nahrgang, M., Auvinen, J. & Bass, S. A., “Heavy-flavor dynamics in relativistic p-Pb collisions at $\sqrt{s_{NN}} = 5.02$ TeV”, *Nucl. Part. Phys. Proc.* Vol. 276-278, 2016, pp. 225–228, DOI: 10.1016/j.nuclphysbps.2016.05.050, arXiv: 1510.07520 [nucl-th].
- [45] Cacciari, M., Frixione, S., Houdeau, N., Mangano, M. L., Nason, P., et al., “Theoretical predictions for charm and bottom production at the LHC”, *JHEP*, vol. 1210, 2012, p. 137, DOI: 10.1007/JHEP10(2012)137, arXiv: 1205.6344 [hep-ph].
- [46] Cacciari, M., Mangano, M. L. & Nason, P., “Gluon PDF constraints from the ratio of forward heavy-quark production at the LHC at $\sqrt{S} = 7$ and 13 TeV”, *Eur. Phys. J.* Vol. C75, no. 12, 2015, p. 610, DOI: 10.1140/epjc/s10052-015-3814-x, arXiv: 1507.06197 [hep-ph].
- [47] Greco, V., Ko, C. M. & Rapp, R., “Quark coalescence for charmed mesons in ultrarelativistic heavy ion collisions”, *Phys. Lett.* Vol. B595, 2004, pp. 202–208, DOI: 10.1016/j.physletb.2004.06.064, arXiv: nucl-th/0312100 [nucl-th].
- [48] Beraudo, A. et al., “Extraction of Heavy-Flavor Transport Coefficients in QCD Matter”, *Nucl. Phys.* Vol. A979, ed. by Rapp, R., Gossiaux, P. B., Andronic, A., Auerbeck, R. & Masciocchi, S., 2018, pp. 21–86, DOI: 10.1016/j.nuclphysa.2018.09.002, arXiv: 1803.03824 [nucl-th].
- [49] Eskola, K. J., Paakkinen, P., Paukkunen, H. & Salgado, C. A., “EPPS16: Nuclear parton distributions with LHC data”, *Eur. Phys. J.* Vol. C77, no. 3, 2017, p. 163, DOI: 10.1140/epjc/s10052-017-4725-9, arXiv: 1612.05741 [hep-ph].

- [50] Vitev, I., “Non-Abelian energy loss in cold nuclear matter”, *Phys. Rev.* Vol. C75, 2007, p. 064906, DOI: 10.1103/PhysRevC.75.064906, arXiv: hep-ph/0703002 [hep-ph].
- [51] Eskola, K., Paukkunen, H. & Salgado, C., “EPS09: A New Generation of NLO and LO Nuclear Parton Distribution Functions”, *JHEP*, vol. 0904, 2009, p. 065, DOI: 10.1088/1126-6708/2009/04/065, arXiv: 0902.4154 [hep-ph].
- [52] Kovarik, k. et al., “nCTEQ15: Global analysis of nuclear parton distributions with uncertainties in the CTEQ framework”, *Phys.Rev.D*, vol. 93, no. 8, Apr. 2016, p. 085037.
- [53] Lansberg, J.-P. & Shao, H.-S., “Towards an automated tool to evaluate the impact of the nuclear modification of the gluon density on quarkonium, D and B meson production in proton–nucleus collisions”, *The European Physical Journal C*, vol. 77, no. 1, 2016, p. 1, DOI: 10.1140/epjc/s10052-016-4575-x, URL: <https://doi.org/10.1140/epjc/s10052-016-4575-x>.
- [54] Albacete, J. L. et al., “Predictions for Cold Nuclear Matter Effects in p +Pb Collisions at $\sqrt{s_{NN}} = 8.16$ TeV”, *Nucl. Phys.* Vol. A972, 2018, pp. 18–85, DOI: 10.1016/j.nuclphysa.2017.11.015, arXiv: 1707.09973 [hep-ph].
- [55] Frixione, S., Nason, P. & Ridolfi, G., “A Positive-weight next-to-leading-order Monte Carlo for heavy flavour hadroproduction”, *JHEP*, vol. 09, 2007, p. 126, DOI: 10.1088/1126-6708/2007/09/126, arXiv: 0707.3088 [hep-ph].
- [56] Corcella, G., Knowles, I. G., Marchesini, G., Moretti, S., Odagiri, K., Richardson, P., Seymour, M. H. & Webber, B. R., “HERWIG 6.5 release note”, 2002, arXiv: hep-ph/0210213 [hep-ph].
- [57] Sjostrand, T., Mrenna, S. & Skands, P. Z., “PYTHIA 6.4 Physics and Manual”, *JHEP*, vol. 0605, 2006, p. 026, DOI: 10.1088/1126-6708/2006/05/026, arXiv: hep-ph/0603175 [hep-ph].
- [58] Jacquemod, M. M. & Mobs, E., “CERN Quick Facts 2018 (English version). CERN Instantané 2018 (version anglaise)”, 2018, URL: <https://cds.cern.ch/record/2631844>.
- [59] Missian, D., Bestmann, P., Fuchs, J.-F., Gayde, J.-C. & Herty, A., *Managing the Survey Activities during LS1*, tech. rep. CERN-ACC-2015-0087, Geneva: CERN, Oct. 2014.
- [60] Aamodt, K. et al., “The ALICE experiment at the CERN LHC”, *JINST*, vol. 3, 2008, S08002, DOI: 10.1088/1748-0221/3/08/S08002.
- [61] Bellwied, R. et al., *ALICE EMCAL Physics Performance Report*, tech. rep., ALICE Collaboration, 2010.
- [62] Dellacasa, G. et al., “ALICE technical design report of the photon spectrometer (PHOS)”, 1999.
- [63] Baldit, A., Barret, V., Bastid, N., Blanchard, G., Castor, J., Chambon, T., Crochet, P., Daudon, F., Devaux, A., Dupieux, P., Espagnon, B., Force, P., Forestier, B., Genoux-Lubain, A., Insa, C., Jouve, F., Lamoine, L., Lecoq, J., Manso, F., Tissot, S., et al., “ALICE TRD Technical design report”, Jan. 2001.
- [64] Abbas, E. et al., “Performance of the ALICE VZERO system”, *JINST*, vol. 8, 2013, P10016, DOI: 10.1088/1748-0221/8/10/P10016, arXiv: 1306.3130 [nucl-ex].

- [65] Cortese, P et al., “ALICE technical design report on forward detectors: FMD, T0 and V0”, 2004.
- [66] Zoccarato, Y. et al., “Front-End electronics and first results of the ALICE VZERO detector”, *Nucl. Instrum. Meth. A*, vol. 626, Jan. 2011, pp. 90–96.
- [67] Miller, M. L., Reygers, K., Sanders, S. J. & Steinberg, P., “Glauber modeling in high energy nuclear collisions”, *Ann.Rev.Nucl.Part.Sci.* Vol. 57, 2007, pp. 205–243, DOI: 10.1146/annurev.nucl.57.090506.123020, arXiv: nucl-ex/0701025 [nucl-ex].
- [68] Abelev, B. et al., “Centrality determination of Pb-Pb collisions at $\sqrt{s_{NN}} = 2.76$ TeV with ALICE”, *Phys.Rev.* Vol. C88, no. 4, 2013, p. 044909, DOI: 10.1103/PhysRevC.88.044909, arXiv: 1301.4361 [nucl-ex].
- [69] Glauber, R. & Matthiae, G., “High-energy scattering of protons by nuclei”, *Nucl.Phys.* Vol. B21, 1970, pp. 135–157.
- [70] Aamodt, K et al., “Alignment of the ALICE Inner Tracking System with cosmic-ray tracks”, *JINST*, vol. 5, 2010, P03003, DOI: 10.1088/1748-0221/5/03/P03003, arXiv: 1001.0502 [physics.ins-det].
- [71] Abelev, B. et al., “Performance of the ALICE Experiment at the CERN LHC”, *Int.J.Mod.Phys.* Vol. A29, 2014, p. 1430044, DOI: 10.1142/S0217751X14300440, arXiv: 1402.4476 [nucl-ex].
- [72] Alme, J. et al., “The ALICE TPC, a large 3-dimensional tracking device with fast readout for ultra-high multiplicity events”, *Nucl. Instrum. Meth.* Vol. A622, 2010, pp. 316–367, DOI: 10.1016/j.nima.2010.04.042, arXiv: 1001.1950 [physics.ins-det].
- [73] Akindinoy, A. et al., “Performance of the ALICE Time-Of-Flight detector at the LHC”, *Eur. Phys. J. Plus*, vol. 128, 2013, p. 44, DOI: 10.1140/epjp/i2013-13044-x.
- [74] Fruhwirth, R., “Application of Kalman filtering to track and vertex fitting”, *Nucl.Instrum.Meth.* Vol. A262, 1987, pp. 444–450, DOI: 10.1016/0168-9002(87)90887-4.
- [75] Abelev, B. et al., “Measurement of visible cross sections in proton-lead collisions at $\sqrt{s_{NN}} = 5.02$ TeV in van der Meer scans with the ALICE detector”, *JINST*, vol. 9, no. 11, 2014, P11003, DOI: 10.1088/1748-0221/9/11/P11003, arXiv: 1405.1849 [nucl-ex].
- [76] Tanabashi, M. et al., “Review of Particle Physics”, *Phys.Rev.D*, vol. 98, no. 030001, 2018.
- [77] Skands, P. Z., “Tuning Monte Carlo Generators: The Perugia Tunes”, *Phys. Rev.* Vol. D82, 2010, p. 074018, DOI: 10.1103/PhysRevD.82.074018, arXiv: 1005.3457 [hep-ph].
- [78] “Measurement of prompt D^0 , D^+ , D^{*+} , and D_s^+ production in p–Pb collisions at $\sqrt{s_{NN}} = 5.02$ TeV”, arXiv: 1906.03425 [nucl-ex].
- [79] Nadolsky, P. M. et al., “Implications of CTEQ global analysis for collider observables”, *Phys.Rev.D*, vol. 78, 2008, p. 013004.
- [80] Acharya, S. et al., “Measurement of D-meson production at mid-rapidity in pp collisions at $\sqrt{s} = 7$ TeV”, 2017, arXiv: 1702.00766 [hep-ex].

- [81] Acharya, S. et al., “Measurement of D^0 , D^+ , D^{*+} and D_s^+ production in pp collisions at $\sqrt{s} = 5.02$ TeV with ALICE”, *JHEP*, vol. 92, Dec. 2019, arXiv: 1901.07979 [nucl-ex].
- [82] Fujii, H. & Watanabe, K., “Heavy quark pair production in high energy pA collisions: Open heavy flavors”, *Nucl. Phys.* Vol. A920, 2013, pp. 78–93, DOI: 10.1016/j.nuclphysa.2013.10.006, arXiv: 1308.1258 [hep-ph].
- [83] Mangano, M. L., Nason, P. & Ridolfi, G., “Heavy quark correlations in hadron collisions at next-to-leading order”, *Nucl. Phys.* Vol. B373, 1992, pp. 295–345, DOI: 10.1016/0550-3213(92)90435-E.
- [84] Sharma, R., Vitev, I. & Zhang, B.-W., “Light-cone wave function approach to open heavy flavor dynamics in QCD matter”, *Phys.Rev.* Vol. C80, 2009, p. 054902, DOI: 10.1103/PhysRevC.80.054902, arXiv: 0904.0032 [hep-ph].
- [85] Kang, Z.-B., Vitev, I., Wang, E., Xing, H. & Zhang, C., “Multiple scattering effects on heavy meson production in p+A collisions at backward rapidity”, *Phys. Lett.* Vol. B740, 2015, pp. 23–29, DOI: 10.1016/j.physletb.2014.11.024, arXiv: 1409.2494 [hep-ph].
- [86] Beraudo, A., De Pace, A., Monteno, M., Nardi, M. & Prino, F., “Heavy-flavour production in high-energy d-Au and p-Pb collisions”, *JHEP*, vol. 03, 2016, p. 123, DOI: 10.1007/JHEP03(2016)123, arXiv: 1512.05186 [hep-ph].
- [87] Adam, J. et al., “ D -meson production in p-Pb collisions at $\sqrt{s_{NN}} = 5.02$ TeV and in pp collisions at $\sqrt{s} = 7$ TeV”, *Phys. Rev.* Vol. C94, no. 5, 2016, p. 054908, DOI: 10.1103/PhysRevC.94.054908, arXiv: 1605.07569 [nucl-ex].
- [88] Fujii, H. & Watanabe, K., “Nuclear modification of forward D production in pPb collisions at the LHC”, 2017, arXiv: 1706.06728 [hep-ph].
- [89] Pumplin, J., Stump, D. R., Huston, J., Lai, H. L., Nadolsky, P. M. & Tung, W. K., “New generation of parton distributions with uncertainties from global QCD analysis”, *JHEP*, vol. 07, 2002, p. 012, DOI: 10.1088/1126-6708/2002/07/012, arXiv: hep-ph/0201195 [hep-ph].
- [90] Adam, J. et al., “Centrality dependence of particle production in p-Pb collisions at $\sqrt{s_{NN}} = 5.02$ TeV”, *Phys.Rev.* Vol. C91, 2015, p. 064905, DOI: 10.1103/PhysRevC.91.064905, arXiv: 1412.6828 [nucl-ex].
- [91] Lourenco, C. & Wohri, H. K., “Heavy flavour hadro-production from fixed-target to collider energies”, *Phys. Rept.* Vol. 433, 2006, pp. 127–180, DOI: 10.1016/j.physrep.2006.05.005, arXiv: hep-ph/0609101 [hep-ph].
- [92] Adare, A. et al., “Heavy Quark Production in $p + p$ and Energy Loss and Flow of Heavy Quarks in Au+Au Collisions at $\sqrt{s_{NN}} = 200$ GeV”, *Phys. Rev.* Vol. C84, 2011, p. 044905, DOI: 10.1103/PhysRevC.84.044905, arXiv: 1005.1627 [nucl-ex].
- [93] Adamczyk, L. et al., “Measurements of D^0 and D^* Production in $p + p$ Collisions at $\sqrt{s} = 200$ GeV”, *Phys. Rev.* Vol. D86, 2012, p. 072013, DOI: 10.1103/PhysRevD.86.072013, arXiv: 1204.4244 [nucl-ex].
- [94] Aaij, R et al., “Prompt charm production in pp collisions at $\sqrt{s} = 7$ TeV”, *Nucl. Phys.* Vol. B871, 2013, pp. 1–20, DOI: 10.1016/j.nuclphysb.2013.02.010, arXiv: 1302.2864 [hep-ex].

- [95] Abelev, B. et al., “Measurement of charm production at central rapidity in proton-proton collisions at $\sqrt{s} = 2.76$ TeV”, *JHEP*, vol. 1207, 2012, p. 191, DOI: 10.1007/JHEP07(2012)191, arXiv: 1205.4007 [hep-ex].
- [96] Aad, G. et al., “Measurement of $D^{*\pm}$, D^\pm and D_s^\pm meson production cross sections in pp collisions at $\sqrt{s} = 7$ TeV with the ATLAS detector”, *Nucl. Phys.* Vol. B907, 2016, pp. 717–763, DOI: 10.1016/j.nuclphysb.2016.04.032, arXiv: 1512.02913 [hep-ex].
- [97] Dusling, K. & Venugopalan, R., “Comparison of the color glass condensate to dihadron correlations in proton-proton and proton-nucleus collisions”, *Phys. Rev.* Vol. D87, no. 9, 2013, p. 094034, DOI: 10.1103/PhysRevD.87.094034, arXiv: 1302.7018 [hep-ph].
- [98] Dumitru, A., Lappi, T. & McLerran, L., “Are the angular correlations in pA collisions due to a Glasmion or Bose condensation?”, *Nucl. Phys.* Vol. A922, 2014, pp. 140–149, DOI: 10.1016/j.nuclphysa.2013.12.001, arXiv: 1310.7136 [hep-ph].
- [99] Abelev, B. et al., “Long-range angular correlations of π , K and p in p-Pb collisions at $\sqrt{s_{NN}} = 5.02$ TeV”, *Phys. Lett.* Vol. B726, 2013, pp. 164–177, DOI: 10.1016/j.physletb.2013.08.024, arXiv: 1307.3237 [nucl-ex].
- [100] Acharya, S. et al., “Production of muons from heavy-flavour hadron decays in p-Pb collisions at $\sqrt{s_{NN}} = 5.02$ TeV”, *Phys. Lett.* Vol. B770, 2017, pp. 459–472, DOI: 10.1016/j.physletb.2017.03.049, arXiv: 1702.01479 [nucl-ex].
- [101] Acharya, S. et al., “Azimuthal anisotropy of heavy-flavour decay electrons in p-Pb collisions at $\sqrt{s_{NN}} = 5.02$ TeV”, *Phys. Rev. Lett.* Vol. 122, no. 7, 2019, p. 072301, DOI: 10.1103/PhysRevLett.122.072301, arXiv: 1805.04367 [nucl-ex].
- [102] “ALICE upgrade physics performance studies for 2018 Report on HL/HE-LHC physics”, 2019, URL: <https://cds.cern.ch/record/2661798>.
- [103] Citron, Z. et al., “Future physics opportunities for high-density QCD at the LHC with heavy-ion and proton beams”, in: *HL/HE-LHC Workshop: Workshop on the Physics of HL-LHC, and Perspectives at HE-LHC Geneva, Switzerland, June 18-20, 2018*, 2018, arXiv: 1812.06772 [hep-ph].

Summary

In this dissertation D^{*+} meson results in proton-proton collisions at $\sqrt{s} = 13$ TeV and proton-lead collisions at $\sqrt{s_{NN}} = 5.02$ TeV at the Large Hadron Collider collected with the ALICE detector have been presented.

Heavy quarks, such as the charm quark that is a constituent of the D^{*+} meson, are effective probes for the study of the properties of the Quark-Gluon Plasma formed in high energy Pb–Pb collisions, as heavy quarks are mainly produced in hard scattering processes in the initial stages of the collision. In p–Pb collisions the production of heavy flavour quarks can be influenced by Cold Nuclear Matter (CNM) effects. The nuclear modification, R_{AA} (R_{pPb}) measures the plasma (cold nuclear matter) effects in Pb–Pb (p–Pb) collisions on the p_T -distribution of the final state particles compared to a particles distribution from minimum bias pp collisions. The comparison of heavy flavour production in proton-Pb and Pb–Pb collisions via the nuclear modification factor allows to distinguish between CNM effects and hot-nuclear matter effects present in Pb–Pb collisions. Measurements of the heavy flavour hadron cross-section in proton-proton collisions allows to test perturbative Quantum Chromo Dynamic calculations in addition to forming a reference measurement for the R_{AA} or R_{pPb} . Ratio's of the cross-section in pp collisions at different collision energies allow to strongly reduce the uncertainties with respect to separate cross-section results, especially in theoretical calculations. The reduction of the uncertainties makes it possible to probe the gluonic properties of the theory with measurements at low D-meson transverse momenta.

The proton-proton results presented in this thesis are within uncertainty consistent with FONLL predictions, though consistently above the central value. Future measurement with the full 13 TeV sample collected in 2015-2018 might be able to decrease the uncertainties sufficiently to further constrain the FONLL predictions. The preliminary results of the ratio of the cross-section at 13 TeV with respect to 5 TeV shown in this thesis are fully consistent with the predictions, and the uncertainty on the measurement and theory are similar. An increase in statistics could significantly improve these results and might make it possible to separate fluctuations from actual differences especially at low transverse momenta.

The presented proton-lead results are consistent with the results in proton-proton collisions. The nuclear modification factor for the average of D-mesons, D^{*+} combined with D^0 and D^+ , shows a flat trend for transverse momenta above 3 GeV/c. These results are in agreement with various models that include cold nuclear matter ef-

fects in the full transverse momentum range, disfavoured a calculation based on incoherent multiple scatterings at low transverse momenta. Models including also some form of Quark-Gluon Plasma show a different trend with respect to p_T , but cannot fully be excluded based on the precision of the current measurements. Measurements done in multiplicity sets in proton-lead collisions show hints of a non-flat shape. These results also show a non-unity centrality ratio at 3σ precision of which the shape is seen at all centralities, hinting towards some form of flow in p-Pb. Measurements of heavy flavour decay electrons find a non-zero v_2 , which is possible due to fluctuations in the initial state geometry, but can also be explained by a very small QGP in proton-lead collisions. The ALICE detectors is currently using long shut down 2 to upgrade the inner tracking system. The upgrades will allow the ALICE detector to do more precise measurements at lower transverse momenta. On top of that the extra precision will also allow us to correct for any B-decay D^{++} mesons via measurement instead of relying on theory to calculate the fraction of B-decay mesons.

Results from this thesis have been presented in various conferences and the proton-lead results can also be found in [78].

Samenvatting

In deze dissertatie zijn de resultaten beschreven van D^{*+} -mesonmetingen die verkregen zijn bij proton-proton botsingen met een massamiddelpunts-energie van 13 TeV en proton-lood botsingen met een massamiddelpunts-energie van 5.02 TeV met behulp van het ALICE experiment bij de Large Hadron Collider.

Zware quarks, zoals de charm quark die voorkomt in D^{*+} -mesonen, zijn van groot belang in het onderzoek naar eigenschappen van het quark-gluonplasma dat gevormd wordt in hoog energetische botsingen van twee lood-ionen (Pb–Pb). Dit komt doordat zulke zware quarks voornamelijk worden gecreëerd in harde verstrooiingsprocessen gedurende de eerste fases van zo'n botsing. In proton-loodbotsingen (p–Pb-botsingen) zou de productie van zware quarks beïnvloed kunnen worden door de aanwezigheid van koude nucleaire materie.

De nucleaire-modificatiefactor, R_{AA} (R_{pPb}) beschrijft het effect van het plasma (respectievelijk de koude nucleaire materie) op de distributie van de loodrechte impuls van de uiteindelijk gevormde deeltjes. Dit wordt gedaan door de resultaten in Pb–Pb- (respectievelijk p–Pb-botsingen) te vergelijken met aselechte metingen in proton-protonbotsingen (pp-botsingen). Door de nucleaire-modificatiefactor in p–Pb- en Pb–Pb-botsingen te vergelijken wordt het mogelijk om effecten van koude nucleaire materie te onderscheiden van die van warme nucleaire materie (quark-gluonplasma).

Daarnaast maken metingen van de botsingsdoorsnedes van hadronen met zware quarks in proton-protonbotsingen het mogelijk om perturbatieve quantumchromodynamische berekeningen te toetsen aan de werkelijkheid. Als we de verhoudingen tussen botsingsdoorsnedes in pp-botsingen bij verschillende massamiddelpunts-energieën bestuderen, vallen enkele theoretische onzekerheden tegen elkaar weg. Dit effect is vooral sterk bij de theoretische voorspellingen voor deze resultaten. De kleinere onzekerheidsmarge maakt het mogelijk om de gluonische eigenschappen van de theorie te bestuderen via metingen van D-mesonen met een lage loodrechte impuls.

De beschreven resultaten voor pp botsingen zijn consistent met de theoretische voorspellingen in FONLL-model (First Order Next to Leading Log). Ze liggen wel boven de verwachte voorspelde waarde voor deze FONLL-berekening, maar binnen de onzekerheidsmarge van deze theoretische voorspelling. In toekomstige metingen is het wellicht mogelijk een dusdanig lage onzekerheid te bereiken dat de resultaten de FONLL voorspellingen verder kunnen begrenzen. Dit zou wellicht al mogelijk zijn

bij het gebruik van alle meetresultaten in proton-proton botsingen bij 13 TeV die in 2015-2018 zijn geregistreerd. De voorlopige resultaten van de verhouding tussen de botsingsdoorsnedes bij 5,02 en 13 TeV komen overeen met de theoretisch voorspelde verhoudingen en de onzekerheidsmarge van data en theorie zijn in dezelfde orde van grootte. Daarom zou een statistisch significantere meting het mogelijk kunnen maken eventuele kleine verschillen te onderscheiden van statistische fluctuaties. Een kleinere onzekerheid zou mogelijk de theoretische voorspelling beter kunnen begrenzen vooral in het interval met de laagste loodrechte impuls die in deze dissertatie beschreven staat.

De gepresenteerde p-Pb-resultaten zijn consistent met de resultaten in pp-botsingen. De nucleaire-modificatiefactor die is berekend voor het gemiddelde van D^{*+} , D^0 - en D^+ -mesonen toont een vlakke trend t.o.v. de loodrechte impuls voor waarden boven de $3\text{GeV}/c$. Deze resultaten komen voor het gehele loodrechte impuls interval overeen met de meeste theoretische voorspellingen waarin de effecten koude nucleaire materie zijn meegenomen. Enkel een modelberekening die gebaseerd is op niet coherente meerdere verstrooiingen is niet volledig consistent met de getoonde resultaten voor zeer kleine loodrechte impuls. Theoretische verklaringen waarin wordt aangenomen dat er in p-Pb-botsingen ook een vorm van een quark-gluonplasma ontstaat, vertonen voor hun een niet vlakke trend ten opzichte van de loodrechte impuls van de D-mesonen. Maar ze staan binnen hun onzekerheidsmarges wel de vlakkere trend van deze meting toe. Als we de nucleaire-modificatiefactor bekijken in verschillende van de multipliciteitsklassen vertoont dit hints van een niet vlakke distributie t.o.v. de loodrechte impuls van de D-mesonen. Als men de verhoudingen tussen de resultaten in verschillende multipliciteitsklassen bestudeerd wordt een 3σ -verschil gezien tussen verschillende multipliciteitsklassen. De trend t.o.v. de loodrechte impuls zien we in elke multipliciteitsklasse. Dit zou wellicht kunnen worden verklaard door een vorm van stroming in proton-lood botsingen. Elliptische stromingsmetingen op electronen afkomstig van het verval van hadronen met zware quarks vinden een significante (5σ) elliptische stroming. Dit komt mogelijk door fluctuaties in de geometrische eigenschappen van de deeltjes voor de botsing, maar kan ook verklaard worden door het ontstaan van een zeer klein quark-gluonplasma in p-Pb-botsingen.

ALICE gebruikt de tweede lange sluiting van LHC voor het verbeteren van o.a. het Inner Tracking System. Deze verbeteringen zorgen niet alleen voor een hogere precisie van de resultaten voor lage loodrechte impulsen, maar maken het ook mogelijk om de correctie op de resultaten voor D^{*+} -mesonen voor het deel dat afkomstig is van B-verval via metingen plaats te laten vinden. Momenteel wordt dit gedaan via de theoretische verwachtingen voor dit verval. De resultaten getoond in deze dissertatie zijn gepresenteerd op meerdere conferenties en de proton-lood resultaten kunnen ook gevonden worden in [78].

Acknowledgments

Before anyone else, I need to thank for and acknowledge the work of André Mischke towards this thesis. André was the one whom I first met at the start of my master thesis, the person who made sure I had a summer students project that fitted with my master thesis, and the first person to ask me if I wanted to continue into my PhD. He motivated me to continue and kept on pushing me to present whenever I could, and even though I sometimes quietly complained that I wanted to be a physicist, not a postergirl, it has helped me tremendously in my presentation skills. I know you would have made me rewrite large parts of this thesis, and I wish you had the opportunity to do so.

An equally big thank you goes out to Alessandro. While you had more roles every year I was there, you never shied away from them. Thank you for being available and for pushing for me if I wanted to go to a conference. But thank you just as much for telling me that it was okay to refuse to search for one when I was getting overwhelmed in combining life and work. Without your help with physics during the start of my PhD, the way you stepped up during André's illness, and even more in the time without him, this thesis would not have been possible.

On a lighter note I must thank Thomas for reading my thesis, as a promotor you were there when needed, but also allowed me the freedom to work it out with Andre and Alessandro when possible. Thank you for helping me with the extensions, the writing and for being available when truly necessary.

Then there is the brilliant heavy flavour Utrecht team: Barbara, Auro, Lennaert, Jasper, Sjaefudin, Henrique and Sandro. You made me laugh, reminded me of details I forgot or missed, and every once in a while solved my problem by simply helping me think out loud.

I have not mentioned Cristina and Luuk with the team as a special thank you must go to both of you, to whom I went with most work-problems: Cristina took care of whatever I could not do, from planning to helping me out when I was away, without you we would not have finished the p-Pb paper. Luuk, you grew from master student who poked me to give him the necessary files for the 5 TeV to the one I poked if something changed in the code while I was at maternity leave. Thank you both for not making me feel like a complete idiot while my brain was still on baby-vacation. As for the rest of Utrechts Subatomic physics group at the time, Raimond, Jacopo, Rihan, Monique, Gert-Jan, Ton, Naomi, Panos, Zhanna, Marco, Mike and Davide Caffari and Davide Lodato, thank you for the atmosphere and the fun/ridiculous/

impossible/honest questions about my kids and life.

On a personal note I have a few extra people to thank, first of all my parents, for understanding the stress, while not always the subject matter, and helping me manage it.

A big thank you also goes to my in-laws who also took over the kids if I needed to finish something and never told me that I needed a better work-life balance at those moments.

I would also like to take the time to thank some friends: my old room-mates and friends Linda and Floris, who even with the distances we had now took care of me at my worst and deserve my very best. As well as my friends Patrick, Pytrik, Chris, Esger, Yassir, Kyra and Anouk who took my mind of work and the kids and made me relax every once in a while.

To honour the project is to honour the road towards it. Thus I have to thank one extra person, as without him I doubt I would have started studying Maths and Physics in the first place. A special thanks goes to Gerard Barendse, who motivated me and showed me there was always more to learn. Thank you. For I have had fun so much fun studying and a very enjoyable PhD-experience. But most of all, this choice of studies has given me my husband and with him our wonderful kids.

Darius, mijn lieve man, wat heb jij te lijden gehad onder dit boekje af en toe. We hebben bijna 7 waanzinnige geweldige en onmogelijk jaren achter de rug, gelukkige of minder gelukkige tijden, we vechten ons er samen doorheen. Dankjewel: dat je me niet laat opgeven, dat je me door mijn zwangerschappen heen hebt geholpen aan het werk te gaan en blijven, ik ben er alleen maar beter van geworden.

I cannot thank my kids for my PhD, as honestly the three of you were my biggest challenge to finish it. The eldest two of you were born during my PhD work and all of you are a lot easier to focus on than writing or coding, but I would not have had it any other way.

You make me smile even when I am at an all-time-low and I hope that one day I can show you this and tell you that working hard for a PhD is truly worth it, but keeping your life-work balance at the same time makes it perfect.

As for all of those I have not mentioned, my apologies. I was never one of few words, and I have simply ran out of reasonable space ;).

Curriculum Vitae

Annelies Veen

14-07-1990

Born in Amsterdam, the Netherlands

Education

2012-2014

MSc. Experimental Physics
Utrecht University, Utrecht, The Netherlands

2008-2012

BSc. Physics and Mathematics (simultaneously)
Utrecht University, Utrecht, The Netherlands

2002-2008

Gymnasium beta
Damstede, Amsterdam, The Netherlands

Work Experience

2019-present

Researcher
ABF Research, Delft, The Netherlands

2014-2019

PhD Candidate
Subatomic Physics
Utrecht University, Utrecht, The Netherlands

